Czech Technical University in Prague

Faculty of Electrical Engineering
Department of Electromagnetic Field

Spatial Vector Microwave Measurement

Doctoral Thesis

Viktor Adler

Prague, July 2018

Ph.D. Programme: Electrical Engineering and Information Technology

Branch of study: Radioelectronics

Supervisor: Prof. Ing. Karel Hoffmann, CSc.

Prohlášení

Tímto prohlašuji, že jsem svou disertační práci na téma "Spatial Vector Microwave Measurement" vypracoval samostatně s použitím odborné literatury a dalších informačních zdrojů, které jsou všechny průběžně citovány a uvedeny v seznamu literatury na konci této práce.

Jako autor uvedené dizertační práce dále prohlašuji, že jsem v souvislosti s vytvořením této práce neporušil autorská práva třetích osob, zejména jsem nezasáhl nedovoleným způsobem do cizích autorských práv osobnostních.

V Praze dne 9. července 2018

.....
Viktor Adler

Poděkování

Chtěl bych poděkovat všem lidem, kteří se jakkoli podíleli na kompletaci této disertační práce. Především děkuji za dlouhodobou podporu své životní partnerce Kláře, která vždy stála při mě a tolerovala všechny nesnáze, které v souvislosti s touto prací vyvstávaly. Dále děkuji svému školiteli prof. Karlu Hoffmannovi, CSc. za odbornou pomoc a za toleranci mého nesystematického a svérázného přístupu k práci. V neposlední řadě děkuji všem kolegům, kteří mě po celou dobu studia na katedře podporovali, byli mi vždy oporou a vždy si našli čas na odborné rady.

Abstrakt

V této práci je představena nová interferometrická měřicí metoda pro měření koeficientu přenosu mezi dvěma anténami. Jestliže je přenos mezi anténami realizován odrazem od nějakého předmětu, lze metodu využít např. pro mikrovlnné zobrazování. Navržený systém obsahuje referenční větev obsahující anténu, která přímo ozařuje přijímací anténu a testovací větev, kde anténa ozařuje testovaný objekt. Elektromagnetická vlna z testovacího kanálu je od testovacího objektu odražena do přijímací antény, kde interferuje s vlnou z referenční větve. Pro jednoznačné získání fázového posunu mezi referenční a testovací vlnou jsou provedena postupně minimálně dvě interferometrická měření, kdy je v referenčním kanálu nastaven vhodný fázový posun a amplituda přenosu. Při měření můžeme provést více nezávislých interferometrických měření a vzniklá redundance může být využita ke zmenšení nejistot měření. Dále byl popsán způsob geometrické representace měření, který umožňuje názorně odhadnout nejisty měření. Nejistoty měření byly určeny i na základě numerické Monte Carlo metody. Navržená konfigurace byla ověřena jak přesným měřením za použití vektorového analyzátoru pro ověření nejistot měření, tak původní konfigurací pro ověření funkčnosti celého konceptu. Navrženou metodou bylo provedeno mikrovlnné zobrazování metodou inverzní syntetické apertury a byla tak ověřena použitelnost navrženého systému.

Klíčová slova: mikrovlnná měření; měření fáze; six-port; nejistoty měření; mikrovlnné zobrazování.

Abstract

This work presents a new interferometric measuring method for measuring the transmission coefficient between two antennas. If the transmission between the antennas is realized by a reflection from an object, the method can be used, e.g., for microwave imaging. The proposed system contains a reference branch containing an antenna that directly irradiates the receiving antenna and a test branch where the antenna irradiates the object under test. The electromagnetic wave from the test channel is reflected from the test object into the receiving antenna where it interferes with the wave from the reference channel. To achieve a unambiguous phase shift between the reference and test waves, at least two interferometric measurements are performed sequentially, with a suitable phase shift and the amplitude of the transmission being set in the reference channel. We can perform more independent interferometric measurements while redundancy can be used to reduce measurement uncertainty. Furthermore, a method of geometric representation of the measurement has been described which makes it possible to clearly estimate the measurement uncertainty. Measurement uncertainties were determined by the numerical Monte Carlo method. The proposed configuration has been verified by accurate measurements using a vector analyzer to verify measurement uncertainties, and the original configuration to verify the functionality of the entire concept. Microwave imaging using the inverse synthetic aperture method was performed to verify the usability of the proposed system.

Keywords: microwave measurements; phase measurement; six-port; measurement uncertainty; microwave imaging.

Contents

List of Abbreviations

ADC	Analog-to-Digital Converter
CPWG	Grounded Coplanar Waveguide
CT	Computer Tomography
DUT	Device Under Test
FMCW	Frequency-Modulated Continuous Wave
FSL	Free Space Loss
HW	Hardware
IDFT	Inverse Discrete Fourier Transform
IFFT	Inverse Fast Fourier Transform
ISAR	Inverse Synthetic Aperture
LO	Local Oscillator
MCM	Monte Carlo Method
MLS	Maximum-Length Sequence
MMIC	Monolithic Microwave Integrated Circuits
PC	Personal Computer
PCB	Printed Circuit Board
PDF	Probability Density Function
PN	Pseudo-Noise
PQFN	Power Quad Flat No-lead
RCS	Radar Cross Section
RTTU	Reflection-Transmission Test Unit
SAR	Synthetic Aperture Radar
SFCW	Stepped-Frequency Continuous Wave

SMA	SubMiniature version A
SMD	Surface-Mount Device
SNR	Signal-to-Noise Ratio
SPDT	Single Pole, Double Throw
SPR	Six-Port Reflectometer
SPST	Single Pole, Single Throw
TRL	Thru-Reflect-Line calibration
TTL	Transitor-Transistor Logic
UOSM	Unknown-Open-Short-Match calibration
VNA	Vector Network Analyzer

Chapter 1

Introduction

This chapter presents the basic motivation and comments content of this thesis. After clarification of the purpose of this work, the thesis objectives are summarized.

1.1 Motivation

In recent years active microwave imaging systems have become widely used due to a rise in terrorist threats and at the Department of Electromagnetic Field of the Czech Technical University in Prague and the Faculty of Electrical Engineering an effort is being made to further the research in this area. The department has to deal with one serious disadvantage: affordable manufacturing of monolithic microwave integrated circuits (MMIC). Unfortunately, this challenge is impossible to meet. The only available option of construction of imaging system is to use discrete components meaning the entire measurement system becomes very extensive as it contains an exceedingly large number of measurement channels. For this reason we have started to develop a new vector measurement method applicable for microwave imaging with a simpler hardware solution.

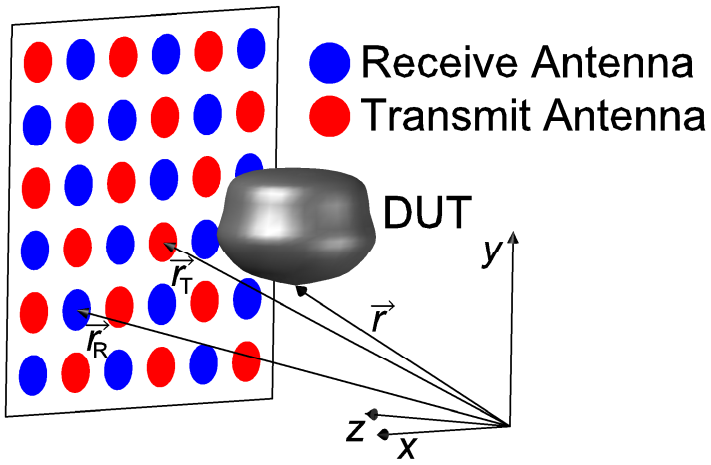

Figure 1.1: Multistatic measurement scenario.

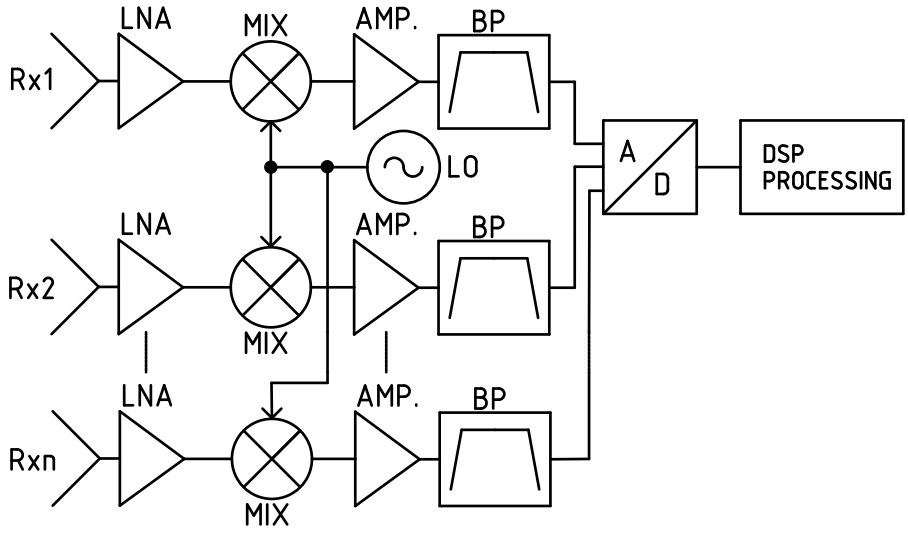

Figure 1.2: Block scheme of the receiving channels in imaging system.

Most real time active imaging systems utilize the multistatic geometrical concept [1] shown in Figure 1.1. Such a system does not require any moving parts because the spatial distribution of the reflectivity of the object under imaging is determined by the positions of individual antennas in the antenna array. The measurement is performed by means of coherent measuring of the complex transmission coefficients between one transmitting antenna and one receiving antenna when the test object is illuminated. During the measurement all possible combinations of transmitting coefficients are consequently measured by switching on all transmitting antennas and utilizing all receiving antennas. The set of measured, complex S-parameters is then $S(\vec{r}_{\mathrm{T}}, \vec{r}_{\mathrm{R}}, f)$, where $\vec{r}_{\mathrm{T}}$ is the position of the transmitting antenna, $\vec{r}_{\mathrm{R}}$ is the position of the receiving antenna and f is the measurement frequency. In total $N_{\mathrm{R}}N_{\mathrm{T}}$ S-parameters are measured at every frequency point where N_{R} and N_{T} are the number of receiving and transmitting antennas. The measured data are then processed by the synthetic aperture radar (SAR) imaging technique [2].

The majority of active microwave imaging systems, e.g., [3, 4, 5, 6, 7], utilize the super-heterodyne principle in all receiving channels as shown in Figure 1.2. For these systems to function properly necessarily requires a relatively large microwave power to be delivered to all mixers MIX of a receiving antennas Rx in antenna array by means of an extensive splitting structure of microwave lines. Even a sparse array concept [8] for relevant imaging may require up to hundreds of antennas and corresponding mixers to be used. Microwave power required from the local oscillator (LO) is then in the order of watts, so the energy efficiency of such a system is very low. More efficient solutions use mixers with individual amplifiers added for the LO signal to reach an appropriate level, however, an extensive splitting structure is still necessary to split the LO signal to individual mixer amplifiers [3].

1.2 Content of the Thesis

Implementation problems mainly resulting from inadequate complexness of microwave imaging systems described above using heterodyne principle for every receiving channel has forced us to develop a new microwave vector measurement method. The new measurement method described in this thesis is generally based on the interferometric measurement techniques similar to the six-port [9] or multistate reflectometer [10] extended to spatial applications. We decided to utilize the multistatic arrangement of a scalar measurement procedure because a measurement of the complex transmission coefficient between antenna pairs was required. We also wanted to effectively exploit the possible redundancy of the measurement arising from the multistate principle to increase measurement precision and obtain high-quality data with simple hardware (HW), unlike the standard vector network analyzer (VNA) measurement.

The thesis is mostly composed of a description of the original results and a description of generally known principles or procedures are stated very briefly mainly via relevant references. This thesis is organized as follows. Section 2 briefly states a principle of the operation of a six-port reflectometer (SPR), then background information of the uncertainty analysis of mutually uncorrelated quantities and the principle of the inverse synthetic aperture (ISAR) imaging method. In Section 3, the measurement procedure and computations of geometrical representation of the measurements are described in detail. In Section 4, the principle of the estimation of the measurement uncertainty on the basis of geometrical representation, and its comparison with measurement uncertainty using the numerical Monte Carlo method (MCM), are explained. In Section 5, an experimental verification of measurement uncertainty utilizing VNA is described. Section 6 describes the implementation and design of several microwave components forming the entire multistate scalar measurement system.

1.3 Thesis Objectives

1. Development of a method to measure vector transmission between a pair of antennas utilizing scalar measurements.

2. Reduce the complexity of the receiving part of the imaging system in comparison to the heterodyne solution and omit the need of a splitting structure for the local oscillator (LO) (reference) signal.

3. Utilizing potential redundancy in the measurement to decrease measurement uncertainty.

4. Laboratory verification of the measurement technique.

Chapter 2

State Of The Art

2.1 Six-Port Measurement

In the network analysis dealing with the vector measurement of scattering parameters, we distinguish two basic principles of measurements. The first principle is called the separation method, which, nowadays, is utilized in a majority of commercially produced VNAs. This method offers us a vector measurement close to the scattering parameters definition, where we directly compare the amplitudes and phases of incident and reflected/transmitted waves separated by a directional coupler. This measurement also requires utilization of a frequency conversion and complicated analog or digital processing of intermediate frequency signals, which makes such a system rather costly. The second principle for network analysis is the interference principle which performs a set of scalar power measurements of several combinations of interfering waves from the device under test (DUT) port. The incident and reflected waves are not directly separated in this method, but their mutual interference via known multi-port microwave circuit leads to unambiguous complex reflection coefficient determination. This principle is utilized in six-port measurement.

The first comprehensive papers concerning the six-port measurement technique were published in December 1977 in IEEE Transactions on Microwave Theory and Techniques [9, 11, 12] by Glenn Engen and Cletus Hoer from the National Institute of Standards and Technology. These three essential papers cover the core ideas, design criteria (minimal uncertainty of measurement, limited dynamics of bolometer detectors), propose a circuit approximately satisfying the criteria and introduce the structure of VNA using two SPRs.

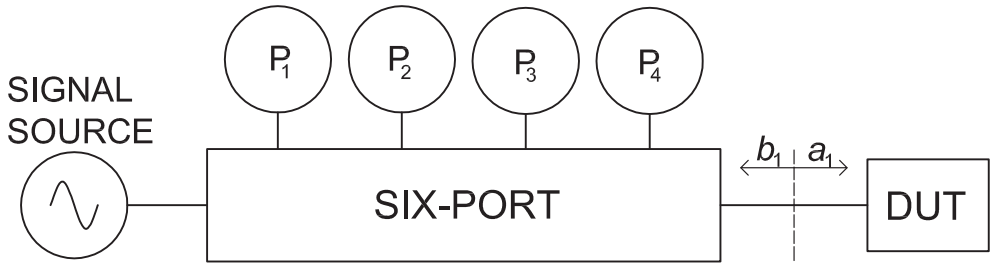

Figure 2.1: Block scheme of six-port reflection coefficient measurement.

The block scheme of the measurement setup is depicted in Figure 2.1. The main idea of SPR is that the microwave power applied to one port of a properly designed microwave linear six-port circuit is divided onto remaining five ports weighted by complex coefficients. These weighting coefficients are mainly determined by the S-parameters of the circuit and by desired reflection coefficient Γ of the DUT. Six-port measurements allow us, on the basis of the four measured powers, P_1 to P_4, to compute the complex reflection coefficient $\Gamma = b_1/a_1$ of the DUT. The waves a_1 and b_1 are complex wave amplitudes at the test port of SPR. Historically, the measurement procedure of reflection coefficient Γ is often graphically represented as shown in Figure 2.2, but in fact, it represents the solution of the system of the three equations. Reflection coefficient Γ is interpreted as an intersection of three circles in a complex plane with centres q_1, q_2 and q_3. The position of the circle centres is a critical design goal of the six-port system and is predetermining the range and uncertainty of the reflection coefficient measurement. The radii of circles r_1, r_2 and r_3 are proportional to square root of measured powers P_1, P_2 and P_3. The fourth measured power, P_4, is used mainly for measuring the incident power to the DUT. The actuals features and measurement uncertainties of the six-port microwave circuit depends on the design goals of the measurement system and several variants can be found in [13]. To perform a relevant measurement with SPR it is necessary to calibrate the measurement system. Several calibration techniques, utilizing a different number of fully known or partially known standards as [14, 15, 16], have been developed. To measure the transmission coefficient of the DUT we must utilize two six-port units [12] and, e.g., thru, reflect, line (TRL) calibration method [17], originally designed for six-port VNAs.

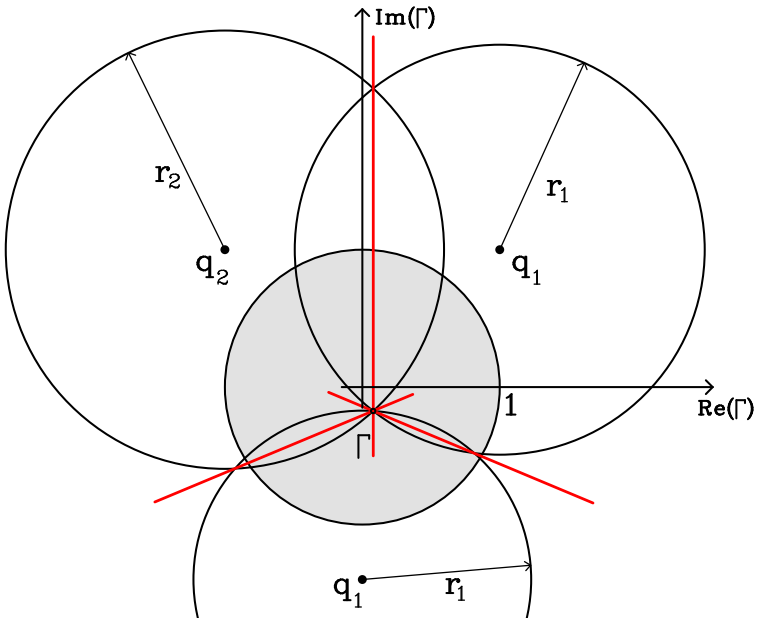

Figure 2.2: Graphical representation of the six-port measurement. The shaded unity circle represents the reflection coefficients of the passive circuits.

2.2 Measurement Uncertainties

In this section we present the basics of an uncertainty analysis, based on recommendations stated in Guide to the Expression of Uncertainty in Measurement (GUM) [18], which should serve as a global standard for the unification of measurement uncertainty computation and representation.

Measurements of any physical quantity in the real world are always degraded with known and, frequently, unknown external influences. The most common influences can be uncalibrated measurement equipment (voltmeter, ampermeter, weighting machine, power detector, ...), limited precision of representation of measured value (digital display, needle panel meter, ...), systematic error caused by method realization (contact resistance, untightened connector, ...), temperature drift and electronic noise. All of these factors cause the real value of measured quantity to never be precisely known and we can just estimate it. To describe the influence of all external adverse effects is usually more complicated than describing the measurement itself. Nevertheless, this procedure is necessary for an indisputable comparison, e.g., of two different methods for measuring the same quantity when we want to designate the better one.

In measurement uncertainty terminology there are several terms which are usually incorrectly interpreted. These terms are error, uncertainty, accuracy and precision. Error is, in the context of measurement, the difference between the measured value and the true value. This indicates that error could have a positive or negative sign with neither sign being favoured. The essential problem is that the true value of quantity is never known, hence we compute error at least from an estimation of the real value. On the other hand, uncertainty defines interval, in which the true value of quantity lies with some, usually high, probability. This interval is usually symmetric and, to some extent, predicts how significant errors during individual measurement reading could be expected in most cases. In situations where we believe that the measured value is close to true value, we say that the measured value is accurate. Since we cannot know whether a value is close to the true value, it is impossible to quantify its accuracy because it is more like a qualitative rating based on individual understanding. But we can definitely judge that one method is more accurate than another based on the computed method's measurement uncertainties. When values obtained by repeat measurements of a particular quantity exhibit little variability, we declare those values as precise. But this is also just a qualitative term, such as accuracy, and we can use this term correctly just for comparing two measurement methods, when one method give us more precise, i.e., fewer time variable values, than another method. It is also necessary to emphasize that values which are meant to be precise can be actually far away from the true value of quantity if a significant systematic error caused, for example, by neglecting some external influence, exists.

Random errors arise from uncontrollable small changes in the measured value, instrumentation or environment. These changes are present as variations in the obtained measured values when repeat measurements are carried out. Uncertainty of measurement represents the variability of measured quantity. When measurement of quantity x is repeated n times, we obtain a set of measurements $x_1, x_2, \ldots, x_n$, which can be understood as realizations of a random process. The mean value of

the set is widely used as the best estimation of the true value of quantity and can be computed as

$$\bar{x} = \frac{1}{n}\sum_{i=1}^{n} x_i, \tag{2.1}$$

and the variability of measured quantity can be described as a standard deviation

$$s = \sqrt{\frac{\sum_{i=1}^{n}\left(x_i - \bar{x}\right)^2}{n-1}}. \tag{2.2}$$

Since the standard deviation describes the spread of quantity x, the name given in metrology to the standard deviation is standard uncertainty and is usually denoted as $u\left(x\right)$. It is necessary to note, that (2.1) and (2.2) are just estimations of mean value and standard deviation, because we usually have a finite number of measurements n, hence the randomness of quantity x can not be precisely determined.

When we measure some physical quantity y indirectly through measurements of another physical quantities $x_1, x_2, \ldots, x_n$, i.e., y is a function of these quantities as $y = f\left(x_1, x_2, \ldots, x_n\right)$ and all partial measurements were obtained with uncertainties $u\left(x_1\right),\ u\left(x_2\right), \ldots,\ u\left(x_n\right)$, then we can determine the standard uncertainty of y as

$$\begin{aligned} u^2\left(y\right) &= \left(\frac{\partial y}{\partial x_1}\right)^2 u^2\left(x_1\right) + \left(\frac{\partial y}{\partial x_2}\right)^2 u^2\left(x_2\right) + \ldots + \left(\frac{\partial y}{\partial x_n}\right)^2 u^2\left(x_n\right) \\ &= \sum_{i=1}^{n}\left(\frac{\partial y}{\partial x_i}\right)^2 u^2\left(x_i\right), \end{aligned} \tag{2.3}$$

which sufficiently holds only when the uncertainties of quantities are $u\left(x_i\right) \ll x_i$ and the degree of sensitivity of function $y = f\left(x_1, x_2, \ldots, x_n\right)$ on an individual x_i can be sufficiently approximated by the first partial derivation (first-order Taylor series approximation). It is also necessary to assume that individual quantities $x_1, x_2, \ldots, x_n$ are uncorrelated, i.e., they were measured by different equipment, or with the same equipment in appreciable time spacing without noticeable systematic error. By application of (2.3) on mean computation shown in (2.1) and assuming that uncertainties of all measured quantities are the same ($u\left(x_i\right) = u\left(x\right)$ for all i), we get the standard uncertainty of mean value as

$$u\left(\bar{x}\right) = \sqrt{\sum_{i=1}^{n}\left(\frac{\partial \bar{x}}{\partial x_i}\right)^2 u^2\left(x_i\right)} = \sqrt{\frac{1}{n^2}\sum_{i=1}^{n} u^2\left(x_i\right)} = \sqrt{\frac{1}{n^2} n u^2\left(x\right)} = \frac{u\left(x\right)}{\sqrt{n}} = \frac{s}{\sqrt{n}}, \tag{2.4}$$

which shows that uncertainty of mean value decreases by a factor of $\sqrt{n}$.

Generally, there exist different ways how to obtain a specific uncertainty $u(x)$ of quantity x; we simply distinguish three type of uncertainties. The so-called Type A uncertainty is based on a sequence of repeated measurements and the computation of mean value and the deviation of the value, i.e., making the simplest statistical analysis necessary. On the other hand, Type B uncertainty is determined by looking

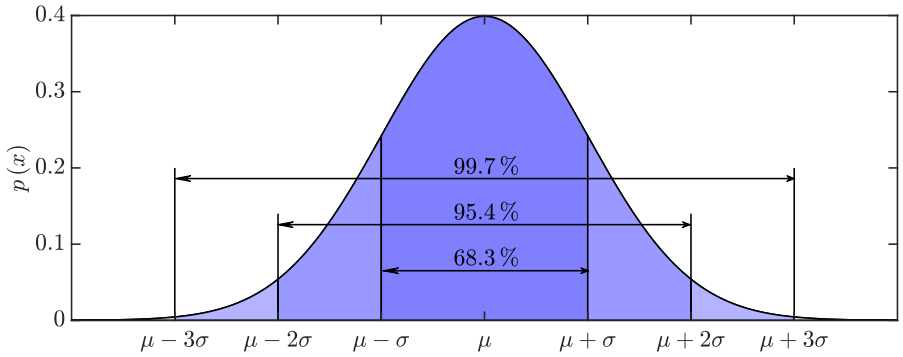

Figure 2.3: Probability density function of normal distribution with mean value μ and standard deviation σ. Stated coverage probabilities for coverage factors $k = 1$, 2 and 3 are also included.

up specific information about the measurement equipment in a calibration report or datasheet. It is obvious that uncertainty stated in the datasheet was also provided using the associated Type A uncertainty statistical procedure, but from the point of view of the reader of the datasheet it represents Type B uncertainty. The third type of uncertainty is so-called combined uncertainty, sometimes called Type C uncertainty, and it consists of the influences of several Type A and Type B uncertainties on some more complex measurement procedure. A combination of individual uncertainties is provided via (2.3), where all uncertainties $u(x_i)$ may be either Type A or Type B. This combined uncertainty is usually stated in the datasheet of measurement equipment and from the reader's point of view it becomes Type B uncertainty for subsequent usage.

Usually the value of measured quantity x has Gaussian (normal) distribution, which is the consequence of the central limit theorem. We assume that the actual measured value of quantity x using some measurement instrument is affected by many of individual external influences, which do not necessarily have to have a normal distribution, but in total they act together and behave in a normal distribution way. Theoretically, the normal distribution has no limits and obtaining infinite values of measured value is (theoretically) possible. In practice the measured values are truncated by certain physical limits of the measurement equipment and, therefore, it would be correct to use truncated normal distribution for the statistical analysis of measured values. Fortunately, in most practical cases these measurement limits are far away from the actual measured value in comparison to measurement uncertainty (variability of measured value), hence the difference between truncated and un-truncated normal distribution is possible to omit.

Practically, we want to know the interval of values, where the true value of measured quantity lies with a probability of usually 95%, sometimes 99%. To express this interval we introduce so-called expanded uncertainty $U(x)$, which is just a multiplication of standard uncertainty $u(x)$

$$U(x) = ku(x), \tag{2.5}$$

where coefficient k is called the coverage factor. The graphical representation of a

normal distribution and coverage intervals for coverage factors $k = 1$, 2 and 3 is depicted in Figure 2.3. For simplicity, coverage factors as integer numbers 2, 3, 4, ... are used in practice, which actually represents the coverage probability 95.4%, 99.7%, 99.994%, ... These coverage factors and specific coverage probabilities actually hold only when we know exactly the whole population of random quantity x, i.e., when we exactly know the statistical properties of quantity x. Otherwise, the determination of mean value $\bar{x}$ and its standard uncertainty $u(\bar{x})$ is not precise and it is necessary to correct the coverage factors for required coverage probability. Finally, in practice we describe the estimation of the real value of quantity x degraded with measurement uncertainty as

$$x = \bar{x} \pm U\left(\bar{x}\right), \tag{2.6}$$

when the coverage interval is not stated directly, it is meant to be 95 %. Hence, the measured value lies with probability 95% in interval $2U\left(\bar{x}\right)$ wide.

2.3 Inverse Synthetic Aperture Radar Measurement

The SAR technique [19], utilizing the same microwave equipment as a standard real aperture radar, offers dramatically better image resolution. Usually the SAR technique is used for Earth ground-mapping and imaging which requires the radar equipment to be attached to a plane or satellite. In a laboratory environment the SAR technique can be carried out using the X-Y positioning system with an antenna attached to it [20], or reversely, with a DUT attached to the positioning system with stationary antennas [21]. To perform precise range measurement with antennas attached to a positioning system is usually difficult because of the need for connection cables, which are stressed during antenna movement. The bending of cables usually causes significant phase errors in frequency domain measurement [22, 23], which, after transformation to a time domain in the sense of an inverse fast Fourier transform (IFFT), causes time or range errors, respectively. To avoid the phase errors of moving the cables of a measurement setup completely, it is possible to move the whole measurement setup together with an antenna, but it requires a rather compact measurement system.

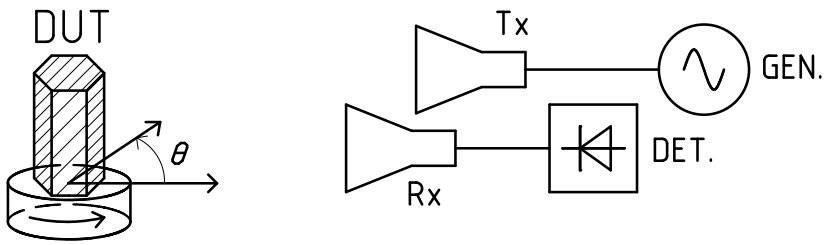

Figure 2.4: Arrangement for na ISAR measurement incorporating two antennas.

To investigate the shape and reflection properties of a certain object we need to examine the backscatter electromagnetic field from that object and performed suitable post processing of measured data. To obtain the shape of an object it is necessary to illuminate the object from various directions and one possibility is to perform a measurement all the way around the object. But there exists also an inverse possibility to rotate the object and investigate the scattered field with the stationary antenna, which is usually suitable for small objects under imaging. A schematic of the measurement is shown in Figure 2.4. The overall power budget of the measurement is highly affected by the radar cross section (RCS) of the DUT and, moreover, by the presence of flat surfaces and corners making RCS highly dependent on the angle of irradiation. Generally, it is necessary to obtain the range profile of the path between two antennas through the reflection from the DUT. The range profile can be obtained by standard radar techniques, e.g., by pulse radar, frequency-modulated continuous wave (FMCW) radar and stepped-frequency continuous wave (SFCW) radar. Measurement via one antenna in a purely monostatic arrangement is also possible. The frequency band of range measurement has to be properly chosen according to the required resolution of the final image. According to inverse Fourier transform properties and its influence on time-domain measurements in microwave vector measurements [24] the range resolution is

$$\Delta R = \frac{c_0}{2\mathrm{BW}}, \tag{2.7}$$

where BW is the bandwidth used. The range profiles are obtained for a set of rotation angles θ_i and form a so-called sinogram which is then used as input data to inverse Radon transform for image reconstruction [25] widely used in computer tomography (CT) imaging [26].

The Radon transform is an invertible integral transform that can produce a 2-D function $R(r, \theta)$ by integrating a function defined on plane $f(x, y)$ along parallel lines at different orientations. The application of the Radon transform of a 2-D function representing the cross section of two cuboids is shown in Figure 2.5. The individual columns of the sinogram represent hypothetically measured range profiles for all rotation angles θ.

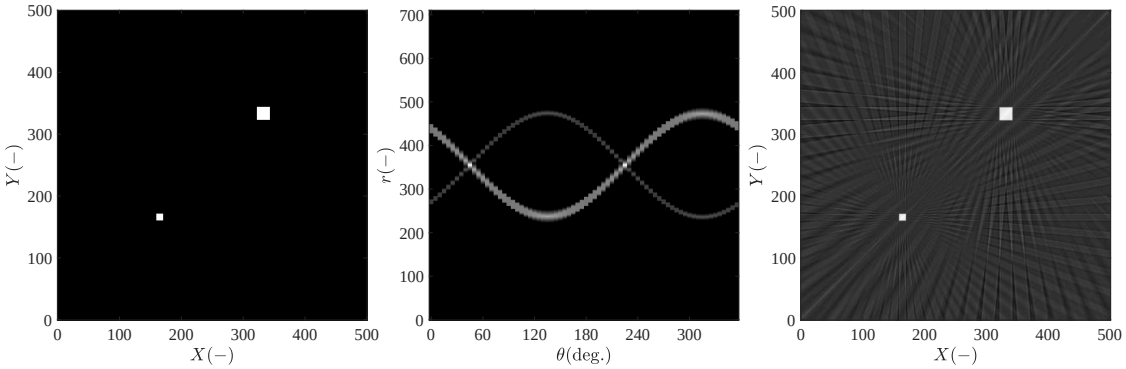

Figure 2.5: Application of a Radon transform to a 2-D function representing a cross section of two cuboids to create a sinogram. Application of an inverse Radon transform to the sinogram reconstructs the original function with noticeable clutter caused by a finite number of θ projection angles. The actual rotation angle step here is $\Delta\theta = 5\,\mathrm{deg}$.

Chapter 3

Principle of Measurement Method

The main goal of the thesis is to develop a measurement method with simple hardware requirements which only make scalar measurements and omit the need of a splitting structure for reference signal distribution. The principle of the measurement method will be shown and described using the simplest possible arrangement to verify the correctness of the basic principles. Most of the following findings have already been published in [27] and [28].

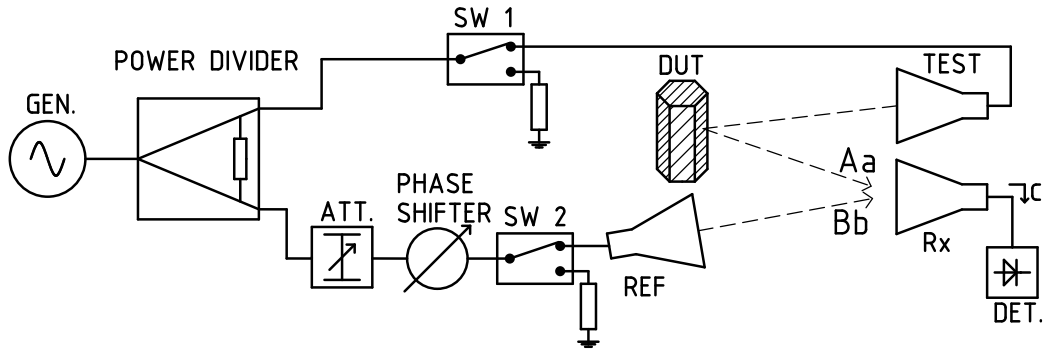

Figure 3.1: Basic measurement configuration.

3.1 Method Basics

A block diagram of the proposed system is shown in Figure 3.1. The output signal from the signal source is divided into two, theoretically independent paths by a power divider. In the upper (test) path the signal is led through switch SW 1 to the TEST transmitting antenna. The radiated electromagnetic wave illuminates a DUT and the reflected wave carrying vector information related to the DUT reflectivity enters into receiving antenna Rx resulting in the output voltage wave Aa. The coherent signal in the lower (reference) path is led from the power divider through an attenuator, a phase shifter with phase shift α and switch SW 2 to an REF transmitting antenna. The REF antenna directly illuminates receiving antenna Rx resulting in a output voltage wave Bb. Constants A and B are used to describe the states of SW 1 and

SW 2 and have a value of 0 or 1. The Rx antenna is directly connected to a detector measuring the incident microwave power. A specific value of the received power depends mostly on the mutual positions and properties of the antennas, the DUT properties and a phase difference between wave a and b.

It is obvious that the proposed system allows the user to make multiple scalar power measurements under different states or conditions. These different conditions allow a set of power measurements containing a sufficient amount of information to compute information about the DUT to be created and enable microwave imaging of the DUT to be performed. Let the vector information about the DUT to be held by variable Γ_{DUT}, which represents the ratio of waves a and b as follows

$$\Gamma_{\mathrm{DUT}} = \frac{b}{a} = \frac{|b|\,\mathrm{e}^{\mathrm{j}\angle(\mathrm{b})}}{|a|\,\mathrm{e}^{\mathrm{j}\angle(\mathrm{a})}} = \frac{|b|}{|a|}\mathrm{e}^{\mathrm{j}(\angle(\mathrm{b})-\angle(\mathrm{a}))} \tag{3.1}$$

The variable Γ_{DUT} actually represents a transmission coefficient between the TEST and Rx antennas, but it is solely influenced by the reflection properties of the DUT. The inverse definition of Γ_{DUT} would be more appropriate to follow the settled nomenclature in VNA terminology, but to follow previously published work, we will preserve this definition. In the next paragraphs we will investigate the procedure and uncertainty analysis of Γ_{DUT} quantity.

Assuming ideal microwave components and no multi-path propagation it is possible to write the power received by the Rx antenna as

$$P = \left|c^2\right| = |Aa + Bb|^2. \tag{3.2}$$

Let us denote the phase difference between waves a and b, when the phase shifter is set to $\alpha = 0\,\mathrm{deg.}$, as

$$\varphi = \angle(b) - \angle(a). \tag{3.3}$$

The amplitude of the wave a and the phase difference φ carrying information about the DUT can be determined as follows.

Various combinations of the SW 1 and SW 2 switches allow us to feed antennas REF and TEST with zero or non-zero microwave power. These cases can be described as:

1. $A = 1;\ B = 0$

   Only the TEST antenna is transmitting. The received power P_{T} is given by

   $$P_{\mathrm{T}} = |c|^2 = |Aa|^2 = |a|^2. \tag{3.4}$$

2. $A = 0;\ B = 1$

   Only the REF antenna is transmitting. The received power P_{R} does not depend on the α phase shift of the ideal phase shifter and is given by

   $$P_{\mathrm{R}} = |c|^2 = |Bb|^2 = |b|^2. \tag{3.5}$$

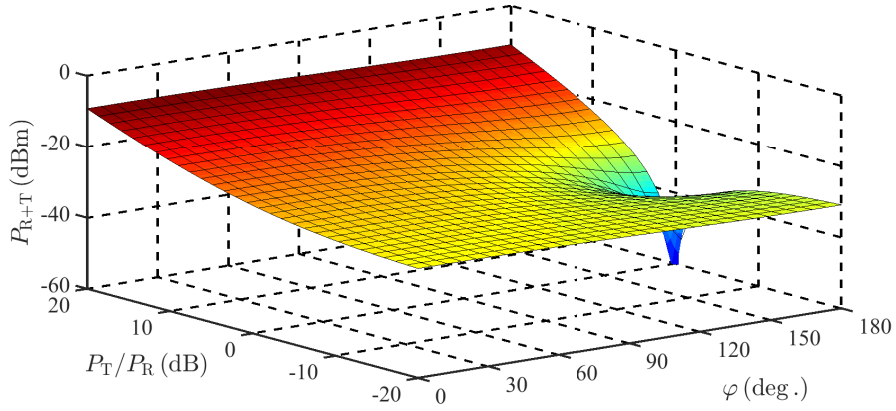

Figure 3.2: Dependence of P_{R+T} for $P_R = 30\,\text{dBm}$ and $\alpha = 0\,\text{deg}$.

3. $A = 1$; $B = 1$

The received power at the Rx antenna is given by the superposition of waves a and b. Electrical lengths of electrical paths in the reference and test channels from the power splitter to the output of receiving antenna Rx are not usually the same, even when the phase shifter is set to $\alpha = 0$. Let us suppose $n \geq 2$ measurements with different phase shifts α_i $(i = 1, 2, ..., n)$ of the phase shifter. For various α_i phase shifts, the Rx antenna receives powers given by

$$\begin{aligned} P_{R+T}^{(i)} &= |c_i|^2 = |Aa + Bb_i|^2 = \left||a| + |b|\,e^{j(\varphi+\alpha_i)}\right|^2 \\ &= \left|\sqrt{P_T} + \sqrt{P_R}e^{j(\varphi+\alpha_i)}\right|^2. \end{aligned} \tag{3.6}$$

Dependence of P_{R+T} from (3.6) for various P_T/P_R, $P_R = 30\,\text{dBm}$ and $\alpha = 0\,\text{deg}$. is depicted in Figure 3.2. It can be clearly seen that for $P_T/P_R = 0\,\text{dB}$ and $\varphi = 180\,\text{deg}$. the ideal destructive interference occurs and received power P_{R+T} attains zero value.

The phase difference φ between waves a and b can be determined only from scalar measurements of received powers P_T, P_R, and $P_{R+T}^{(i)}$. To do so it is best to express this power ratio

$$\frac{P_{R+T}^{(i)}}{P_T} = \frac{\left||a| + |b|\,e^{j(\varphi+\alpha_i)}\right|^2}{|a|^2} = \left|1 + \sqrt{\frac{P_R}{P_T}}e^{j(\varphi+\alpha_i)}\right|^2 \tag{3.7}$$

Equation (3.7) can be interpreted as n circles in the complex plane with a shared center $C = -1 + j0$ with radii

$$R_i = \sqrt{\frac{P_{R+T}^{(i)}}{P_T}} \tag{3.8}$$

intersected by a circle with a radius

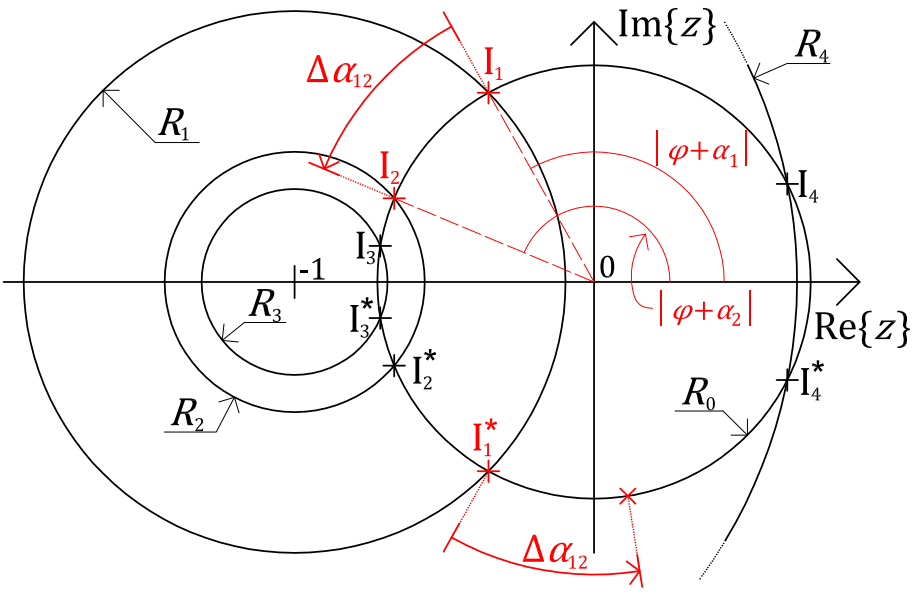

Figure 3.3: The geometrical interpretation of (3.7) for $n = 4$ and $\Delta\alpha_{12} > 0$.

$$R_0 = \sqrt{\frac{P_\mathrm{R}}{P_\mathrm{T}}} \tag{3.9}$$

with its center in the origin as is illustrated in Figure 3.3. The considered set of circles have n pairs of complex conjugated intersections I_i and I_i^*. For arguments of the intersection points it holds

$$\angle(\mathrm{I}_i) = -\angle(\mathrm{I}_i^*) = |\varphi + \alpha_i| \tag{3.10}$$

and the coordinates of the intersection points in the complex plane can be expressed as $\mathrm{I}_i = X_i + \mathrm{j}Y_i$. The real coordinates can be calculated as

$$X_i = \frac{1}{2}\left(R_i^2 - R_0^2 - 1\right) \tag{3.11}$$

and the imaginary coordinates as

$$Y_i = \sqrt{R_0^2 - X_i^2}. \tag{3.12}$$

The result of (3.12) always holds $Y_i \geq 0$ and therefore always holds $\mathrm{Im}(\mathrm{I}_i) \geq 0$ and $\mathrm{Im}(\mathrm{I}_i^*) \leq 0$.

Clearly, the argument of intersection points I_i and I_j ($j = 1, 2, ..., n$) depends on the settings of phase shifts α_i and α_j of the phase shifter. It is useful to express the phase difference between these two phase settings as

$$\Delta\alpha_{ij} = \alpha_j - \alpha_i, \tag{3.13}$$

presuming $\Delta\alpha_{ij} \in (-180, 180]$ deg. This value is always known including its sign, because we set this value during the measurement. When we consider an ideal and

noiseless microwave power measurement on the Rx antenna for the precise determination of φ, the actual set values of shifts α_i are not significant and can practically have an arbitrary value. The only important condition is for $\alpha_i \neq a_j$, i.e. $\Delta\alpha_{ij} \neq 0$.

According to a previously defined notation, the transmission coefficient between the TEST and Rx antennas can be written as

$$\Gamma_{\mathrm{DUT}} = R_0 \mathrm{e}^{\mathrm{j}\varphi}. \tag{3.14}$$

Now it is clear that to obtain the absolute value of the DUT reflection $|\Gamma_{\mathrm{DUT}}| = R_0$ it is enough to measure just the P_{R} and P_{T} powers without any other redundancy introduced by phase shifter settings, i.e., with settings $\alpha_i = 0$. But to emphasise that quantities R_0, R_i, α_i and Γ_{DUT} ale closely connected, we will show that it is also possible to express reflection Γ_{DUT} from R_i as follows. From (3.7), (3.8) and (3.9) it can be derived that

$$R_i^2 = R_0^2 + 2R_0 \cos(\varphi + \alpha_i) + 1. \tag{3.15}$$

After rearranging and substituting $R_0 = |\Gamma|$ we get the quadratic equation

$$|\Gamma|^2 + 2\cos(\varphi + \alpha_i)|\Gamma| + 1 - R_i^2 = 0 \tag{3.16}$$

with $|\Gamma|$ as an unknown variable. The solution of this equation is

$$|\Gamma|_{1,2} = \pm\sqrt{R_i^2 - \sin^2(\varphi + \alpha_i)} - \cos(\varphi + \alpha_i). \tag{3.17}$$

It is necessary to determine which root is the physical one and to prove that under realistic physical conditions the root cannot be imaginary. It can be derived that roots are imaginary only if

$$P_{\mathrm{R+T}} = P_{\mathrm{T}} - P_{\mathrm{R}}, \tag{3.18}$$

which can hold if

$$P_{\mathrm{R+T}} = P_{\mathrm{T}} + P_{\mathrm{R}} + 2\sqrt{P_{\mathrm{T}}P_{\mathrm{R}}}\cos(\varphi + \alpha_i) \tag{3.19}$$

which is possible only in case when (neglecting trivial solution)

$$P_{\mathrm{T}} = P_{\mathrm{R}} \quad \wedge \quad \varphi + \alpha_i = \pi, \tag{3.20}$$

which is impossible, because waves would be completely destructively interfered. And what is the physical root from two from (3.17)? It is the one with a plus sign ensuring positive absolute value of reflection Γ. Result cannot be negative because, otherwise, one of powers P_{T}, or P_{R} would have to be negative.

3.2 Dealing with Ambiguity in Phase

Equation (3.10) shows that the argument of intersection $\mathrm{I_i}$ only determines the absolute value of the phase shift $|\varphi + \alpha_i|$. The correct sign of φ is unknown, but it can be determined as follows. Figure 3.3 illustrates the situation for $n = 4$ (four

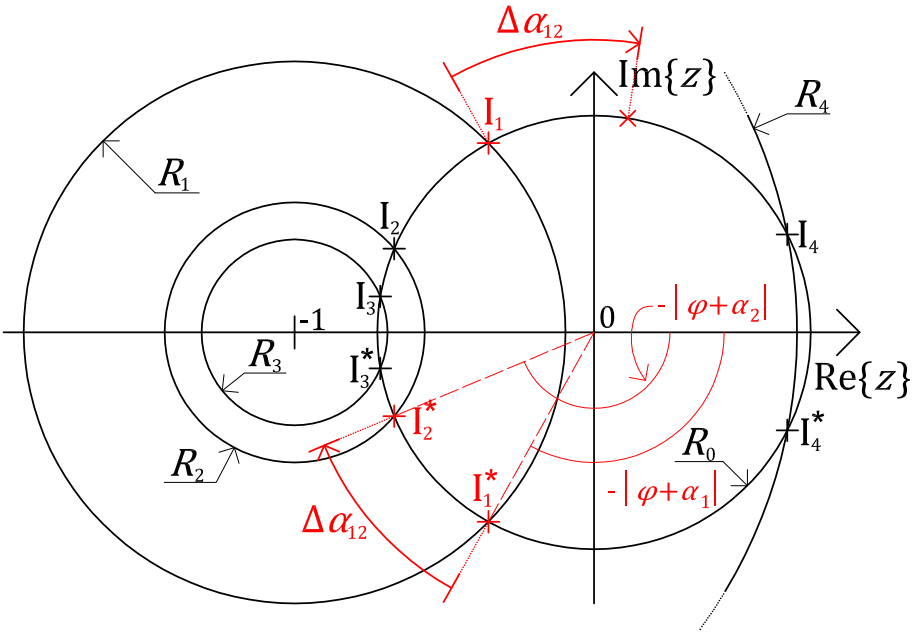

Figure 3.4: The geometrical interpretation of (3.7) for $n = 4$ and $\Delta\alpha_{12} < 0$.

couples of intersection points and four circles with radii R_i sharing center -1). As explained in the section 4, in the case of real measurements with uncertainties, the higher the number of measurements, the smaller the final uncertainty is. Hence, from a practical point of view it is beneficial to deal with measurements with more than two settings of the phase shifter.

Let us first consider an ideal measurement which requires exactly $n = 2$ arbitrary pairs of intersection points, e.g., I_1, I_1^* and, I_2, I_2^*, to determine the φ sign correctly. In the geometrical situation shown in Figure 3.3 $\Delta\alpha_{12} > 0$ (the arrow is counterclockwise) and $\angle(\mathrm{I}_1) + \Delta\alpha_{12} = \angle(\mathrm{I}_2)$ and $\angle(\mathrm{I}_1^*) + \Delta\alpha_{12} \neq \angle(\mathrm{I}_2^*)$. Therefore $(\varphi + \alpha_1) > 0$ holds and the phase difference φ is equal to $\varphi = \angle(\mathrm{I}_1) - \alpha_1$.

However, if the phase difference was set to $\Delta\alpha_{12} < 0$ (Figure 3.4) and received powers were the same as in Figure 3.3, then $\angle(\mathrm{I}_1^*) + \Delta\alpha_{12} = \angle(\mathrm{I}_2^*)$ and $\angle(\mathrm{I}_1) + \Delta\alpha_{12} \neq \angle(\mathrm{I}_2)$ would hold. It would result in relations $(\varphi + \alpha_1) < 0$ and $\varphi = -\angle(\mathrm{I}_1) - \alpha_1$. But, even if the received powers were the same in cases depicted in Figure 3.3 and Figure 3.4, the physical circumstances of the DUT were definitely different and, in practice, it is improbable to receive the same powers with different DUT. It is just an illustrative example.

So, assuming an ideal microwave power measurement, $n = 2$ measurements are enough to determine the phase difference φ between waves a and b precisely including its correct sign. When $n > 2$ measurements, one arbitrary intersection point, I_i, is chosen to determine the absolute value of φ and an arbitrary one, I_j, to determine the sign. There are $n - 1$ possibilities of choosing the intersection point I_j. When supposing ideal microwave hardware and no measurement uncertainties we can choose an arbitrary one. The following generalized procedure of the phase difference φ determination, including its correct sign, can be derived. If

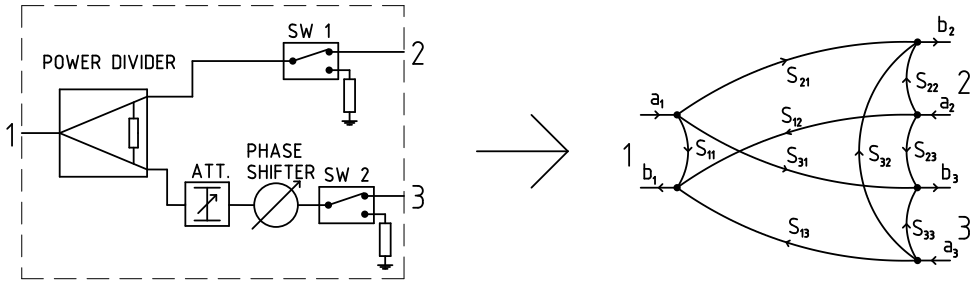

Figure 3.5: Representation of a multistate microwave system from measurement setup as a general three-port circuit.

$$|\angle(\mathrm{I}_i) + \Delta\alpha_{ij}| - \angle(\mathrm{I}_j) = 0 \tag{3.21}$$

then $(\varphi + \alpha_i) > 0$ and

$$\varphi = \angle(\mathrm{I}_i) - \alpha_i. \tag{3.22}$$

If

$$|\angle(\mathrm{I}_i) - \Delta\alpha_{ij}| - \angle(\mathrm{I}_j) = 0 \tag{3.23}$$

then $(\varphi + \alpha_i) < 0$ and

$$\varphi = -\angle(\mathrm{I}_i) - \alpha_i. \tag{3.24}$$

The algorithm only needs the arguments of intersection points and the phase shifts values. No complex conjugated points are necessary.

3.3 Influence of Hardware Imperfections

All previously stated procedures and computations assume ideal microwave HW which has zero reflections, insertion losses and infinite isolations. From a practical point of view this is a significant simplification, but to analyse the influence of all possible imperfections on the resulting transmission Γ_{DUT} measurement would be inadequately extensive for the purposes of this work. The whole problem of sensitivity of measurement on real hardware imperfections should be generalized to three-port circuit as shown in Figure 3.5 and influence of all parameters of circuit should be investigated.

According to the HW realization proposed later in Section 6 we will provide a simple analysis for a case, where the settings of the phase shifter influence not only the phase of S_{31}, but also the amplitude of this transmission. An ideal phase shifter has a scattering matrix

$$\mathbf{S}_{\mathrm{ideal}} = \mathrm{e}^{\mathrm{j}\alpha} \begin{bmatrix} 0 & 1 \\ 1 & 0 \end{bmatrix}, \tag{3.25}$$

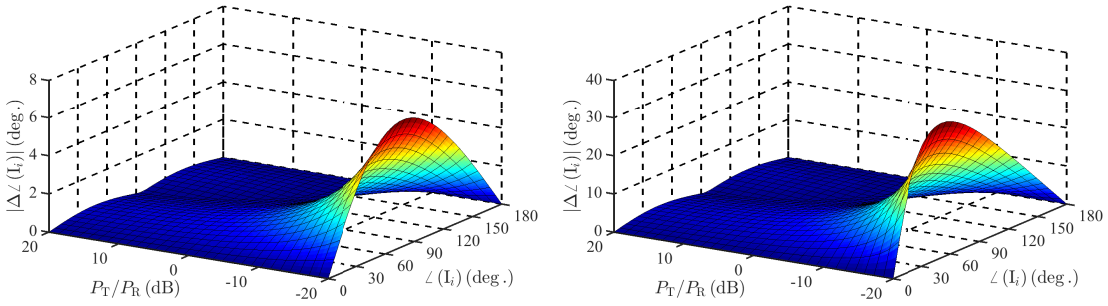

Figure 3.6: Error of argument of intersection point $\mathrm{I_i}$ caused by dependence of amplitude of the transmission of the phase shifter on a set phase shift. (a) $T(\alpha) = 0.1\,\mathrm{dB}$, (b) $T(\alpha) = 0.5\,\mathrm{dB}$.

where the amplitude of transmission is independent of a set phase shift α. In reality the amplitude of transmission is usually phase-setting dependent and the scattering matrix of such a phase shifter can be described as

$$\mathbf{S}_{\mathrm{real}} = T(\alpha)\,\mathbf{S}_{\mathrm{ideal}}, \tag{3.26}$$

where $T(\alpha)$ is the transmission amplitude dependence on a set phase shift α. This dependence brings inconsistency into the measurement of powers $P^{(i)}_{\mathrm{R+T}}$ for particular phase shift settings α_i, where different power from the REF antenna is actually transmitted to the Rx antenna compared to the measurement of power P_{R}, which was measured e.g., with phase settings $\alpha_i = 0\,\mathrm{deg}$. The received power $P^{(i)}_{\mathrm{R+T}}$ is then, according to (3.6), newly

$$P^{(i)}_{\mathrm{R+T}} = \left|\sqrt{P_{\mathrm{T}}} + |T(\alpha_i)|\,\sqrt{P_{\mathrm{R}}}\mathrm{e}^{\mathrm{j}(\varphi+\alpha_{\mathrm{i}})}\right|^2, \tag{3.27}$$

and according to (3.8) it will lead to incorrect radius R_i and, therefore, to an inaccurate phase difference φ determination. The error of φ determination, or error of argument of intersection point $\angle(\mathrm{I}_i)$, respectively, for $T(\alpha) = 0.1$ and $0.5\,\mathrm{dB}$ is depicted in Figure 3.6. It can be seen that errors of argument determination can be practically in order of units and tens of degrees, hence it is necessary to prevent this error.

The simplest way how to eliminate error in measurement caused by dependence $T(\alpha)$ is to create a set of measurements of reference powers $P^{(i)}_{\mathrm{R}}$ for the same settings of phase shifter α_i as for measurements of powers $P^{(i)}_{\mathrm{R+T}}$. Then compute a set of radii of circles $R^{(i)}_0$ according to (3.9), but with usage of the set of powers $P^{(i)}_{\mathrm{R}}$

$$R^{(i)}_0 = \sqrt{\frac{P^{(i)}_{\mathrm{R}}}{P_{\mathrm{T}}}} \tag{3.28}$$

and use these radii for intersection coordinates computations as

$$X_i = \frac{1}{2}\left(R_i^2 - R_0^{(i)2} - 1\right) \tag{3.29}$$

and

$$Y_i = \sqrt{R_0^{(i)2} - X_i^2}. \tag{3.30}$$

The absolute value of the DUT reflection $|\Gamma_{\mathrm{DUT}}|$ is not affected by dependence of transmission $T(\alpha)$ because it is computed directly from $R_0 = \sqrt{P_{\mathrm{R}}/P_{\mathrm{T}}}$ and we assume that the phase shifter was sett to $\alpha_i = 0$ deg., which we consider as a reference value.

Chapter 4

Uncertainty Analysis

In this section we describe the influence of uncertainty of a power detector on the uncertainty of phase difference φ between a reference and test wave.

4.1 Geometrical Approach

In the previous ideal case it did not matter which intersection point was used to determine the absolute value and correct sign of φ. However, in real measurements, influenced by uncertainties, the situation is more complex.

The simplest approach can be suggested in the following way. Intersection point, I_i, is chosen as the point created by the perpendicular intersection of circles. The position of such a point, as explained later, has minimum uncertainty. The correct sign of φ is most likely to be determined from intersection point I_j where the maximum difference between the results of (3.21) and (3.23) is reached. Results of these equations are never equal. The index j of the appropriate intersection point is

$$\arg \max_{j \in \{1,n\}/i} \left(\left| \angle \left(\mathrm{I}_i \right) + \Delta\alpha_{ij} \right| - \left| \angle \left(\mathrm{I}_i \right) - \Delta\alpha_{ij} \right| \right). \tag{4.1}$$

The operator argmax works as follows: $\arg \max_x f(x) = \{x | \forall y : f(y) \leq f(x)\}$. The outcome of this operator is a value or set of values of x for which $f(x)$ attains its largest value. With the optimum point I_j we can then use (3.21) - (3.24) to determine the correct sign of phase difference φ. The expression in the max operator can have a value from 0 deg. ($\angle(\mathrm{I}_i) = 0$ deg., $\Delta\alpha_{ij} = \pm 180$ deg.) to 180 deg. ($\angle(\mathrm{I}_i) = 90$ deg., $\Delta\alpha_{ij} = \pm 90$ deg.). When the mutual phase differences $\Delta\alpha_{ij}$ are chosen properly, the incorrect determination of the sign of phase difference φ is practically impossible.

The approach described above is simple but does not exploit all information contained in the measured data. Let us now consider a more advanced approach. The measured microwave power detected behind the Rx antenna is always affected by the uncertainty of the detector. The radii of circles R_0 and R_i, computed from measured powers, are affected as well. From a geometrical point of view, the ideal intersection points are thus transformed into intersection areas because we have to assume the intersection of rings instead of the intersection of circles. The phase difference φ is, thus, only possible to determine with some uncertainty. The situation of the intersection of the two rings is depicted in Figure 4.1.

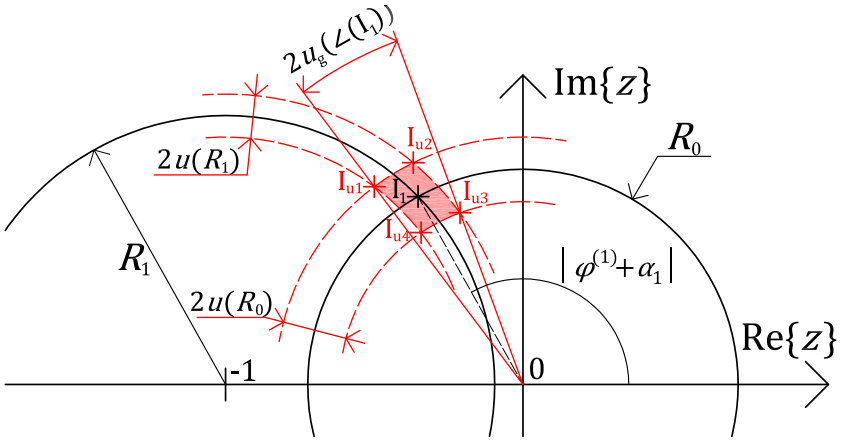

Figure 4.1: Illustration of the intersection of two rings.

The size and shape of the intersection area depends on the uncertainty of the power measurements and on the angle of intersection of these two rings. The angle of intersection depends on the electrical length of the reference and the test channel, and on test object properties. The smaller the intersection area, the better the determination of the phase difference φ. It is clear that a perpendicular intersection of circles results in minimum uncertainty. To maximize the likelihood that at least one circle with the radius R_i intersects the circle with the radius R_0 almost perpendicularly, regardless of the actual value φ, we must properly choose a set of phase shifts α_i. One possible solution is to use α_i which are uniformly distributed on the interval $[0,\ 180]$ deg. with the mutual phase shift $180/(n-1)$ deg.

The outcome of a microwave power measurement is always a number which lies with a certain probability in a coverage interval [29] which is defined not only by the detector itself, but also by features of the whole measurement circuit. When using the minimum number of measurements of $P_{\mathrm{R+T}}^{(i)}$ $(n=2)$ there are two realizations of φ. Let the first realization be labeled $\varphi^{(1)}$. Its absolute value is identified from the argument $\angle(\mathrm{I}_1)$ and its correct sign from $\angle(\mathrm{I}_2)$ and $\Delta\alpha_{12}$. The absolute value of the second realization labeled $\varphi^{(2)}$ is identified from the argument $\angle(\mathrm{I}_2)$ and its correct sign from $\angle(\mathrm{I}_1)$ and $\Delta\alpha_{21}$. The arguments of intersection points I_1 and I_2 are affected by the uncertainties of power measurements and that is why generally $\varphi^{(1)} \neq \varphi^{(2)}$. In general, when we have n power measurements of $P_{\mathrm{R+T}}^{(i)}$ corresponding to n settings of α_i, then we have n realizations of φ. The phase difference φ is then considered as a random circular variable with the average value [30]

$$\bar{\varphi} = \angle\left(\frac{1}{n}\sum_{i=1}^{n} \mathrm{e}^{\mathrm{j}\varphi^{(\mathrm{i})}}\right). \tag{4.2}$$

The average value of the measured quantity is commonly considered as the best estimation of the correct value of quantity, supposing an equal uncertainty of individual values [29]. But in our case every realization of phase difference $\varphi^{(i)}$ is obtained with a different standard uncertainty and to minimize the final standard uncertainty $u(\bar{\varphi})$, some realization of $\varphi^{(i)}$, with excessive standard uncertainty, should be eliminated from the computation. Hence, we can compute the sample mean

$$\bar{\varphi} = \angle\left(\frac{1}{|M|}\sum_{i\in M} \mathrm{e}^{\mathrm{j}\varphi^{(\mathrm{i})}}\right), \tag{4.3}$$

where M is the set of indices i for the realization of φ with sufficiently small uncertainty and $|M|$ is the total members of set M. An example of a proper set of realizations from a real measurement is stated in section 5.

The actual value of standard uncertainty $u\left(\varphi^{(i)}\right)$ depends on the size and shape of intersection area. The widths of rings can be evaluated using the law of uncertainty propagation [29]. Let us assume that microwave power is degraded only by Gaussian noise, the signal-to-noise ratio (SNR) on the power detector is high and that the measured powers P_{R}, P_{T} and $P_{\mathrm{R+T}}^{(i)}$ are uncorrelated. Then the standard uncertainties of radii R_0 and R_i are given by the equations

$$u\left(R_0\right) = \sqrt{\left(\frac{\partial R_0}{\partial P_{\mathrm{R}}} u\left(P_{\mathrm{R}}\right)\right)^2 + \left(\frac{\partial R_0}{\partial P_{\mathrm{T}}} u\left(P_{\mathrm{T}}\right)\right)^2} \tag{4.4}$$

and

$$u\left(R_i\right) = \sqrt{\left(\frac{\partial R_i}{\partial P_{\mathrm{T}}} u\left(P_{\mathrm{T}}\right)\right)^2 + \left(\frac{\partial R_i}{\partial P_{\mathrm{R+T}}^{(i)}} u\left(P_{\mathrm{R+T}}^{(i)}\right)\right)^2}, \tag{4.5}$$

where

$$\frac{\partial R_0}{\partial P_{\mathrm{R}}} = \frac{1}{2P_{\mathrm{T}}}\sqrt{\frac{P_{\mathrm{T}}}{P_{\mathrm{R}}}}\,, \frac{\partial R_0}{\partial P_{\mathrm{T}}} = \frac{-1}{2P_{\mathrm{T}}}\sqrt{\frac{P_{\mathrm{R}}}{P_{\mathrm{T}}}},$$

$$\frac{\partial R_i}{\partial P_{\mathrm{T}}} = \frac{-1}{2P_{\mathrm{T}}}\sqrt{\frac{P_{\mathrm{R+T}}^{(i)}}{P_{\mathrm{T}}}} \text{ and } \frac{\partial R_i}{\partial P_{\mathrm{R+T}}^{(i)}} = \frac{1}{2P_{\mathrm{T}}}\sqrt{\frac{P_{\mathrm{T}}}{P_{\mathrm{R+T}}^{(i)}}}\,.$$

The standard uncertainties $u(P)$ of the power detector can be obtained from its datasheet. Expanded uncertainties $U(P) = ku(P)$ for a specific coverage factor k, and specific coverage probability, respectively, are frequently used supposing a normal distribution of measured power [29].

In most cases the intersection area has four vertices, $\mathrm{I_{u1}}$ to $\mathrm{I_{u4}}$, (Figure 4.1) and the geometrically obtained uncertainty $u_{\mathrm{g}}\left(\angle\left(\mathrm{I}_1\right)\right)$ of the argument of the intersection point I_1 is given by two vertices of the intersection area with the lowest and the highest argument. In the case of Figure 4.1 the geometrical uncertainty is given by

$$u_{\mathrm{g}}\left(\angle\left(\mathrm{I}_1\right)\right) = u_{\mathrm{g}}\left(\left|\varphi^{(1)} + \alpha_1\right|\right) = \frac{\angle\left(\mathrm{I_{u1}}\right) - \angle\left(\mathrm{I_{u3}}\right)}{2}. \tag{4.6}$$

For further uncertainty analysis we will use imaginary power detector, which has expanded uncertainty ($k = 3$) as depicted in Figure 4.2. Uncertainty characteristics were inspired by the widely used HP85025 and HP85037 power detector family [31] and shows the basic properties of diode power detection uncertainties, where low powers are affected by noise and high powers by the linearity of voltage characteristics.

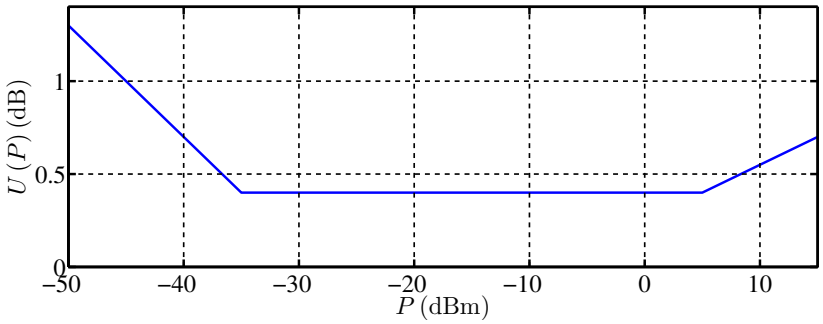

Figure 4.2: The expanded uncertainty of an fictional power detector.

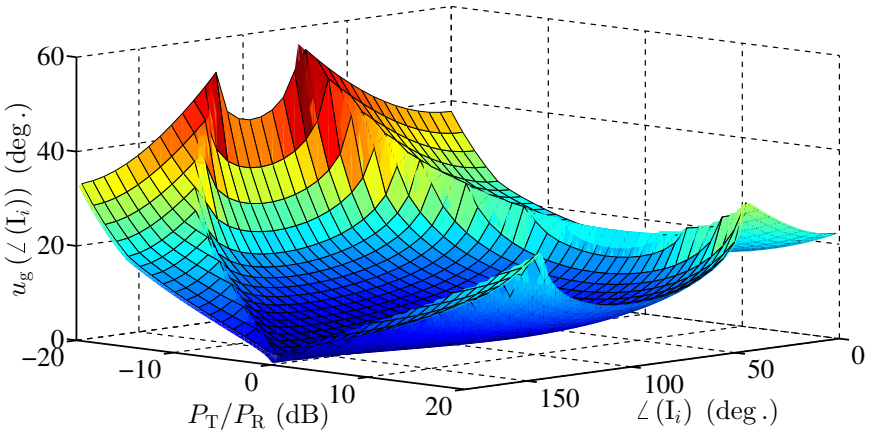

Figure 4.3: The geometrical uncertainty $u_\mathrm{g}\left(\angle\left(\mathrm{I}_i\right)\right)$ for all possible arguments of intersection points $\angle\left(\mathrm{I}_i\right)$ and for the various ratios of P_T and P_R when using imaginary power detector and $P_\mathrm{R} = -20\,\mathrm{dBm}$.

The dependence of u_g on all possible arguments of intersection points $\angle\left(\mathrm{I}_i\right)$, and for the various ratios $P_\mathrm{R}/P_\mathrm{T}$ and our fictional power detector is depicted in Figure 4.3. Its expanded uncertainty is $U(P) = 0.4\,\mathrm{dB}$ $(k = 3)$ for input powers from $-35\,\mathrm{dBm}$ to $5\,\mathrm{dBm}$ while outside of this power range it increases linearly with a slope of approximately $0.06\,\mathrm{dB/dBm}$ (see Figure 4.2). From Figure 4.3 it can be seen that the most accurate determination of the argument of the intersection point I_i generally occurs when the ratio of the received powers is $P_\mathrm{R}/P_\mathrm{T} = R_0^2 \approx 1$. This ratio can be reached with an adjustable microwave attenuator (Figure 3.1) or amplifier in the measurement circuit (reference channel). When the circles intersect almost tangentially, i.e. when $\angle\left(\mathrm{I}_i\right) = \left|\varphi^{(1)} + \alpha_i\right| \approx 0$ or $180\,\mathrm{deg.}$, the intersection area does not contain all four vertices, therefore these cases must be assessed individually. Some of these special cases are depicted in Figure 4.4. The main feature of these intersection areas is that one of the lines which geometrically defines the uncertainty $u_\mathrm{g}\left(\angle\left(\mathrm{I}_1\right)\right)$ is the real axis of the complex plane, because the shape of the intersection area is always symmetrical with regard to the real axis and because we a priori assume the correct determination of the sign of $\varphi^{(i)}$ using the argument of another suitable intersection point I_j.

In a real measurement, meaning one influenced by uncertainties, when $R_0 \gg R_i$

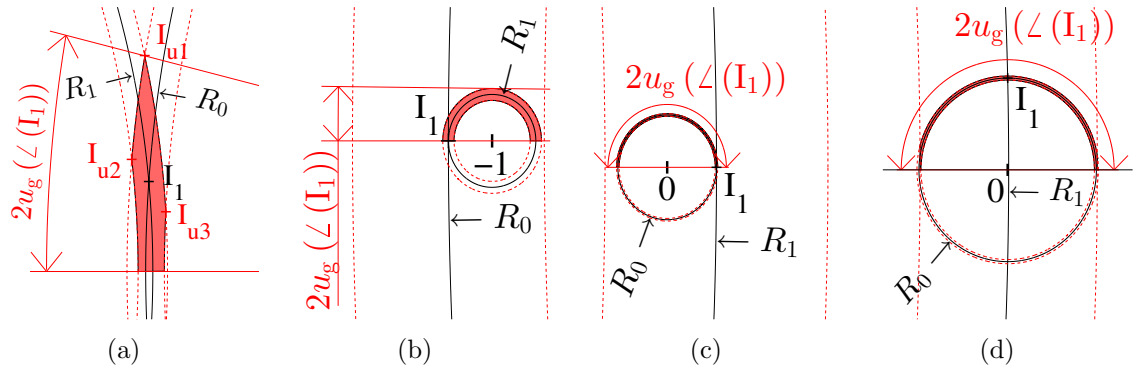

Figure 4.4: Special intersection cases for fictional power detector with uncertainty in Figure 4.2. For all graphs holds $P_{\mathrm{R}} = -30\,\mathrm{dBm}$. (a) $P_{\mathrm{T}} = -25\,\mathrm{dBm}$, $P_{(\mathrm{R+T})} = -32.081\,\mathrm{dBm}$. It leads to an almost tangential intersection: $\angle(\mathrm{I}_1) = 175\,\mathrm{deg}$. Only three vertices of the intersection area exist. (b) $P_{\mathrm{T}} = -30.09\,\mathrm{dBm}$, $P_{\mathrm{R+T}} = -69.74\,\mathrm{dBm}$. It leads to tangential intersection: $\angle(\mathrm{I}_1) = 180\,\mathrm{deg}$. (c) $P_{\mathrm{T}} = 8\,\mathrm{dBm}$, $P_{\mathrm{R+T}} = 8.109\,\mathrm{dBm}$. It leads to tangential intersection: $\angle(\mathrm{I}_1) = 0\,\mathrm{deg}$. Geometrical uncertainty of the argument of I_1 is in this case $u_{\mathrm{g}}(\angle(\mathrm{I}_1)) = 90\,\mathrm{deg}$. (d) $P_{\mathrm{T}} = 2.9\,\mathrm{dBm}$, $P_{\mathrm{R+T}} = 2.9022\,\mathrm{dBm}$. It leads to $\angle(\mathrm{I}_1) \approx 90\,\mathrm{deg}$. and $u_{\mathrm{g}}(\angle(\mathrm{I}_1)) = 90\,\mathrm{deg}$.

($\angle(\mathrm{I}_i) \approx 180\,\mathrm{deg}$.), or, $R_0 \ll R_i$ ($\angle(\mathrm{I}_i) \approx 0\,\mathrm{deg}$.), situations may occur where the intersection point, and even intersection area, does not exist at all. It may be caused by the uncertainty of measurement but also by unpredictable, random, external effects which influence the real measurement setup. In these cases we estimate the argument of the intersection point as 180 deg. and 0 deg., respectively. But for these measurements we are unable to determine the geometrical uncertainty $u_{\mathrm{g}}(\angle(\mathrm{I}_i))$. Eliminating such a measurement from set M in (4.3) is a reasonable solution. Moreover, a great difference between the radii of circles R_0 and R_i may be another source of large uncertainties (Figure 4.4(c), 4.4(d)) and that is one of the reasons why the dynamic range of measurement is practically limited.

The dynamic range of measurement can be understood as the maximum range of power P_{T} for which is possible to measure the phase difference φ with small uncertainty. The dynamic range is limited from bottom by the noise level and can be reached when the received powers P_{T} and P_{R} are very small, and/or almost the same and waves a and b have the mutual phase shift $(\varphi + \alpha_i) \approx 180\,\mathrm{deg}$. resulting in $P^{(i)}_{\mathrm{R+T}} \approx 0$ W. The upper limit of the dynamic range is limited by the maximal non-destructive measurable power by the power detector and can be reached by the excessively high powers P_{R} and/or P_{T} which, together, constructively interfere ($(\varphi + \alpha_i) = 0\,\mathrm{deg}$.). Another case reaching the upper limit of the dynamic range of measurement results from the measurement method itself and not from the maximum measurable power of the power detector. That case is depicted in Figure 4.4(d) when $\angle(\mathrm{I}_1) \approx 90\,\mathrm{deg}$. and $R_0 \leq u(R_1)$ the geometrical uncertainty is unacceptably high, $u_{\mathrm{g}}(\angle(\mathrm{I}_1)) = 90\,\mathrm{deg}$., and such a measurement is practically useless. It can be derived, that the situation depicted in Figure 4.4(d) occurs when the $|\varphi + \alpha_1| = \angle(\mathrm{I}_1) \approx 90\,\mathrm{deg}$. and simultaneously

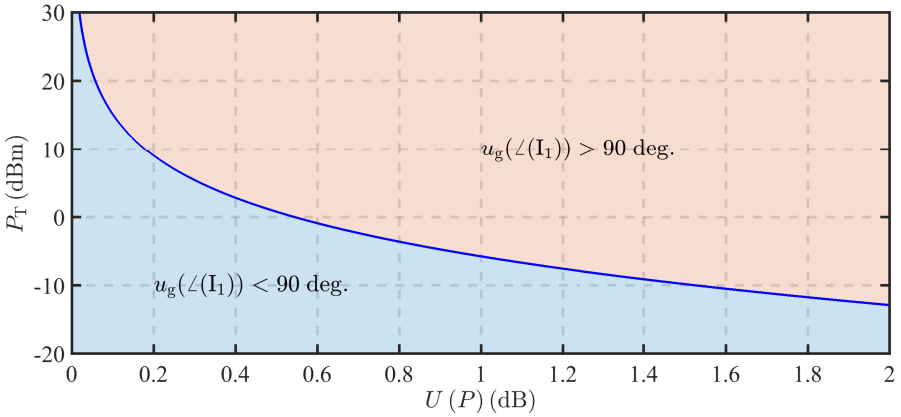

Figure 4.5: Maximal test power P_{T} for measurement with geometrical uncertainty $u_{\mathrm{g}}\left(\angle\left(\mathrm{I}_1\right)\right) < 90\,\mathrm{deg.}$ for $P_{\mathrm{R}} = -30\,\mathrm{dBm}$ and our fictional power detector with uncertainty characteristics in Figure 4.2. For P_{T} with value on dividing curve the case in Figure 4.4(d) occurs.

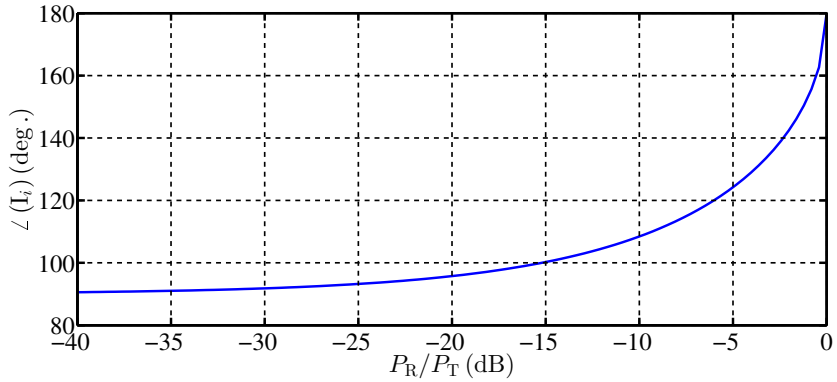

Figure 4.6: Necessary argument of intersection point $\angle\left(\mathrm{I}_i\right)$ enabling perpendicular intersection of circles for various ratios of powers P_{T} and P_{R}.

$$P_{\mathrm{T}} \geq P_{\mathrm{R}} + 10\log_{10}\left(\frac{2k^2}{\left(10^{\frac{U(P)_{\mathrm{dB}}}{10}} - 1\right)^2} - 1\right), \tag{4.7}$$

where k is the coverage factor for which the expanded uncertainty of the power detector is stated in decibels $U(P)_{\mathrm{dB}}$. E.g., when $P_{\mathrm{R}} = -30\,\mathrm{dBm}$ and $U(P)_{\mathrm{dB}} = 0.4\,\mathrm{dB}$ $(k = 3)$ then the reflected power from the test object should be $P_{\mathrm{T}} \leq -30 + 32.9 = 2.9\,\mathrm{dBm}$ when measuring the $\angle\left(\mathrm{I}_1\right)$ with geometrical uncertainty smaller than 90 deg. For a better detector with $U(P)_{\mathrm{dB}} = 0.1\,\mathrm{dB}$ $(k = 3)$ the upper limit of the dynamic range is improved and power P_{T} should be $P_{\mathrm{T}} \leq -30 + 45.2 = 15.2\,\mathrm{dBm}$. These worst case scenarios hold for the particular situation when $|\varphi + \alpha_1| \approx 90\,\mathrm{deg.}$ Dependence of (4.7) is depicted in Figure 4.5. For the other arguments of intersection points when $\angle\left(\mathrm{I}_1\right) \neq 90\,\mathrm{deg.}$ the uncertainty is generally smaller.

The geometrical uncertainty $u_{\mathrm{g}}\left(\angle\left(\mathrm{I}_1\right)\right)$ obtained from the geometrical representation of the measured powers is an estimation of standard uncertainty $u\left(\angle\left(\mathrm{I}_1\right)\right)$

which is directly equal to the standard deviation of $\angle(\mathrm{I}_1)$ a priori presuming a normal distribution of $\angle(\mathrm{I}_1)$. This presumption sufficiently holds when uncertainties of measured powers $u(P) \ll P$ while circles are intersecting almost perpendicularly. It results in bivariate normal distribution of the coordinates X_i and Y_i of the intersection point I_i and the shape of the coverage region is elliptical [32]. However, such a situation occurs rarely and only when

$$\cos(\angle(\mathrm{I}_i)) = -\sqrt{\frac{P_\mathrm{R}}{P_\mathrm{T}}} = -R_0 \tag{4.8}$$

is satisfied. The dependence of intersection points $\angle(\mathrm{I}_i)$ on power ratios $P_\mathrm{R}/P_\mathrm{T}$ is shown in Figure 4.6 and it can be seen that the perpendicular intersection can not happen when $P_\mathrm{R}/P_\mathrm{T} > 1$. As the perpendicular intersection occurs rarely it is not possible to presume the bivariate normal distribution generally. In general, when the angle $\angle(\mathrm{I}_i)$ lies anywhere in an interval of $[0,\, 180]$ deg. it is practically impossible to find an analytical solution for the standard deviation of $\angle(\mathrm{I}_i)$ for every combination of P_R, P_T, $P_{\mathrm{R+T}}$ and detector uncertainty $u(P)$. Therefore, in accordance with [18], when we are not able to ensure the distribution of the input quantities close to the normal distribution, and the linearized model of measurement used by the law of uncertainty propagation is not precise enough, it is more reliable to perform a numerical solution of uncertainty.

4.2 Numerical Approach

The MCM enables us to determine how much the geometrical estimation $u_\mathrm{g}(\angle(\mathrm{I}_i))$ differs from the numerically computed standard deviation $u_\mathrm{MCM}(\angle(\mathrm{I}_i))$. The numerical computation was performed by a huge amount of simulated measurements of powers P_R, P_T and $P_{\mathrm{R+T}}$ with specific uncertainties (standard deviations) $u(P)$. The number of trials was chosen with the intention of properly showing the coverage areas up to probability $p = 99.7\%$ and to compute the correction data for an approximate geometrical uncertainty determination. In accordance with [33], the number of trials should be greater than $1/(1-p)\,10^4 = 3.33 \cdot 10^6$ trials. We have utilized 10^7 trials, which allowed us to create a sufficiently precise illustration of the shape of coverage areas for $p = 99.7\%$ and a determination of variance of $\angle(\mathrm{I}_1)$ with uncertainty approximately $\sqrt{2/10^7} = 0.045\%$ [29].

An example of MCM output using our fictional power detector is depicted in Figure 4.7. Based on the MCM simulations the population of intersection points I_i and its standard deviation of argument $\angle(\mathrm{I}_i)$ were computed. As this statistical computation was performed from many measurements, we consider the outcome of MCM uncertainty $u_\mathrm{MCM}(\angle(\mathrm{I}_i))$ to be equal to the correct standard uncertainty $u(\angle(\mathrm{I}_i))$. At this point, we can compare the values of geometrically obtained uncertainty and values of numerically obtained uncertainty through the correction coefficient κ as

$$\kappa = \frac{u_\mathrm{MCM}(\angle(\mathrm{I}_i))}{u_\mathrm{g}(\angle(\mathrm{I}_i))} = \frac{u(\angle(\mathrm{I}_i))}{u_\mathrm{g}(\angle(\mathrm{I}_i))}, \tag{4.9}$$

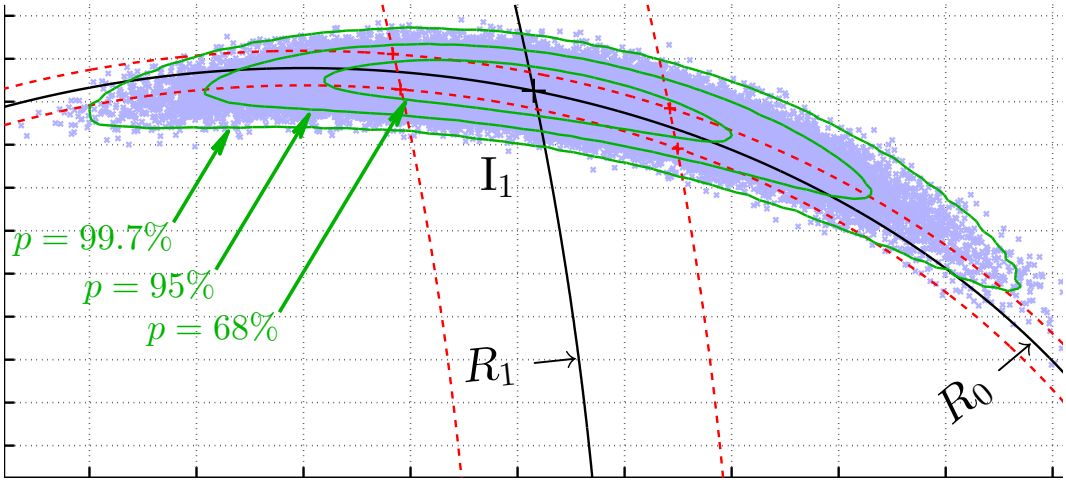

Figure 4.7: The output of MCM simulation with 10^7 trials. Received powers are $P_\mathrm{R} = -10\,\mathrm{dBm}$, $P_\mathrm{T} = 5\,\mathrm{dBm}$ and $P_\mathrm{R+T} = 5.483\,\mathrm{dBm}$. It results in the intersection point I_1 with the argument $\angle(\mathrm{I}_1) = 76\,\mathrm{deg}$. Powers were simulated with standard deviation given by features of our fictional power detector. Uncertainty regions are depicted for coverage probabilities $p = 68$, 95 and 99.7%. It is clear that the probability density function of positions of intersection points has not bivariate normal distribution.

hence, it is possible to express the standard uncertainty $u(\angle(\mathrm{I}_i))$ from geometrical uncertainty $u_\mathrm{g}(\angle(\mathrm{I}_i))$ as

$$u(\angle(\mathrm{I}_i)) = \kappa u_\mathrm{g}(\angle(\mathrm{I}_i))\,. \tag{4.10}$$

Coefficient κ is used as a correction coefficient for obtaining the correct standard uncertainty on the basis of geometrically obtained uncertainty. It is easier to make one robust numerical simulation for several combinations of received powers for a particular power detector and then use κ for a simple correction of geometrical uncertainty (4.10) because the geometrical uncertainty can be easily obtained in real time measurements based on measured powers.

The computation of κ for the particular case depicted in Figure 4.7 using the probability density function (PDF) is depicted in Figure 4.8. In Figure 4.7 the numerically computed uncertainty region for the coverage probability $p = 68\%$ seems to be wider than the intersection area, however, it is not true as seen in Figure 4.8. The geometrically obtained standard uncertainty, i.e. the width of the intersection area, is wider than the MCM standard uncertainty (deviation) $u_\mathrm{MCM}(\angle(\mathrm{I}_1))$ due to the shape of its coverage region for $p = 68\%$. There is a large number of points with arguments similar to $\angle(\mathrm{I}_1)$ making the standard deviation of $\angle(\mathrm{I}_1)$ smaller than expected from the bivariate coverage region. In this particular case $\kappa = 0.9$. However, it does not hold generally.

The actual values of κ depend on the measured powers and uncertainties of these powers. The MCM simulation assumed our fictional power detector (uncertainty in Figure 4.2) for all combinations of received powers in the ranges of $P_\mathrm{T} \in [-40,\, 0]\,\mathrm{dBm}$, $P_\mathrm{R} \in [-60,\, 20]\,\mathrm{dBm}$ and $P^{(i)}_\mathrm{R+T}$ resulting in each argument be-

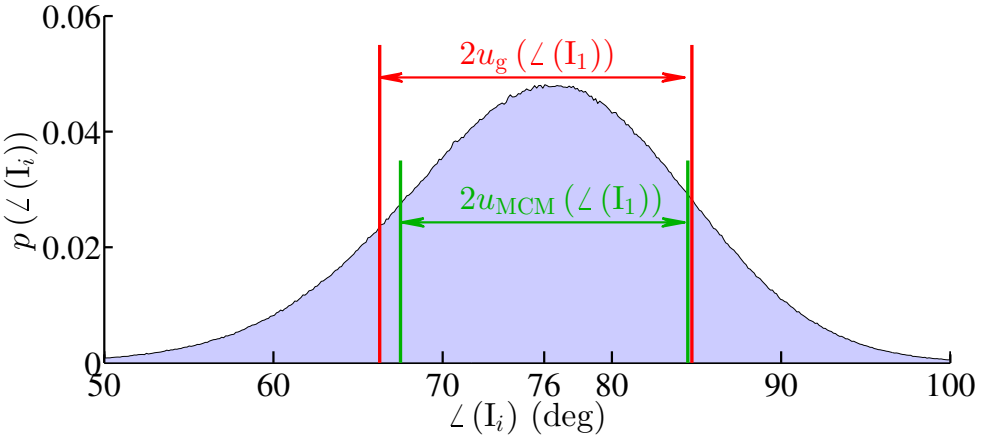

Figure 4.8: Probability density function of the argument of population of intersection points from MCM simulation depicted in Figure 4.7. The PDF is almost Gaussian. Median of arguments is 76 deg., standard deviation (uncertainty) of arguments $u_{\mathrm{MCM}}\,(\angle\,(\mathrm{I}_1)) = 8.3\,\mathrm{deg}$. and geometrically obtained uncertainty is $u_{\mathrm{g}}\,(\angle\,(\mathrm{I}_1)) = 9.2\,\mathrm{deg}$. Correction coefficient κ is then $\kappa = 8.3/9.2 = 0.90$.

ing $\angle\,(\mathrm{I}) \in [0,\,180]\,\mathrm{deg}$. The corresponding correction coefficient κ has an average value of $\bar{\kappa} = 0.67$ and has a 95% probability of lying in the interval [0.24, 0.99]. It means that uncertainty $u_{\mathrm{g}}\,(\angle\,(\mathrm{I}_1))$ is, in most cases $(1 - 0.67)/0.67 = 49\%$ higher than uncertainty $u_{\mathrm{MCM}}\,(\angle\,(\mathrm{I}_1))$. This deviation is unique for each power detector uncertainty value. The dependence of κ on uncertainties of power detector was analyzed and determined to not be significant. For example $\bar{\kappa} = 0.70$ for a detector with expanded uncertainty $U(P) = 0.2\,\mathrm{dB}$ $(k = 3)$ and $\bar{\kappa} = 0.72$ corresponds to a detector with a practically unreachable low value of expanded uncertainty of $U(P) = 0.01\,\mathrm{dB}$. We can conclude that for common power detectors with expanded uncertainties in the order of tenths of dB, the geometrically obtained uncertainty $u_{\mathrm{g}}\,(\angle\,(\mathrm{I}_1))$ is pessimistic estimation of standard uncertainty $u\,(\angle\,(\mathrm{I}_1))$ with an error in the order of tens of percentile points. The dependence of coefficient κ and resulting standard uncertainty $u\,(\angle\,(\mathrm{I}_i))$ on the various ratios $P_{\mathrm{R}}/P_{\mathrm{T}}$ and for all $\angle\,(\mathrm{I}_i)$ supposing our fictional power detector is depicted in Figure 4.9 and Figure 4.10. It can be clearly seen that it is advantageous for powers P_{T} and P_{R} to be the same $(P_{\mathrm{T}}/P_{\mathrm{R}} = 0\,\mathrm{dB})$ because in that case uncertainty $u\,(\angle\,(\mathrm{I}_i))$ attains its minimal value for whatever actual value of $\angle\,(\mathrm{I}_i)$.

The precision of the settings of the phase shifts α_i is also important in the uncertainty computation. The uncertainty of the phase difference $\varphi^{(i)}$ is given by

$$u\left(\varphi^{(i)}\right) = \sqrt{u(\angle\,(\mathrm{I}_i))^2 + u(\alpha_i)^2}. \tag{4.11}$$

This equation is based on the application of the law of uncertainty propagation on (3.22) or (3.24). The final standard uncertainty of the phase difference $\bar{\varphi}$, when using average (4.2) for computation, is, approximately, given by

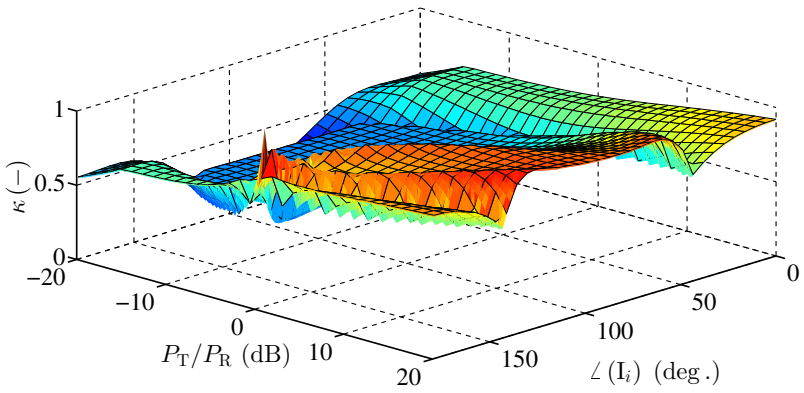

Figure 4.9: Numerically determined coefficient κ for our fictional power detector when $P_R = -30\,\mathrm{dBm}$.

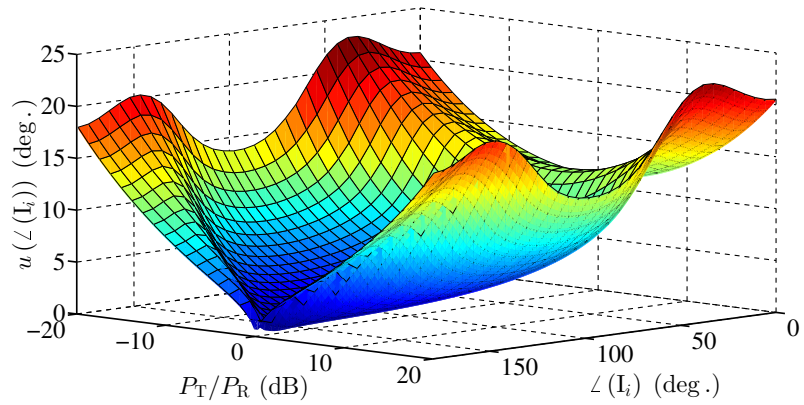

Figure 4.10: Resulting standard uncertainty $u\left(\angle\left(\mathrm{I}_i\right)\right)$ computed by (4.10) using the geometrical uncertainty from Figure 4.3 and κ from Figure 4.9.

$$u\left(\bar{\varphi}\right) = \frac{1}{n}\sqrt{\sum_{i=1}^{n} u(\varphi^{(i)})^2}. \tag{4.12}$$

This computation is based on the assumption that the determination of the uncertainty of average of the circular random variable is reasonably approximated by the uncertainty of the arithmetic mean when the standard uncertainty $u\left(\varphi^{(i)}\right)$ is small (maximally about 10 deg.). But even when a higher quality power detector ($U(P) \approx 0.1\,\mathrm{dB}$) is used, in some particular cases (Figure 4.4(c), 4.4(d) the uncertainty $u\left(\varphi^{(i)}\right)$ can be significantly higher than 10 deg. Then it is definitely better to use (4.3) for the computation of $\bar{\varphi}$ resulting in

$$u\left(\bar{\varphi}\right) = \frac{1}{|M|}\sqrt{\sum_{i\in M} u(\varphi^{(i)})^2}. \tag{4.13}$$

Chapter 5

Verification Measurement With VNA

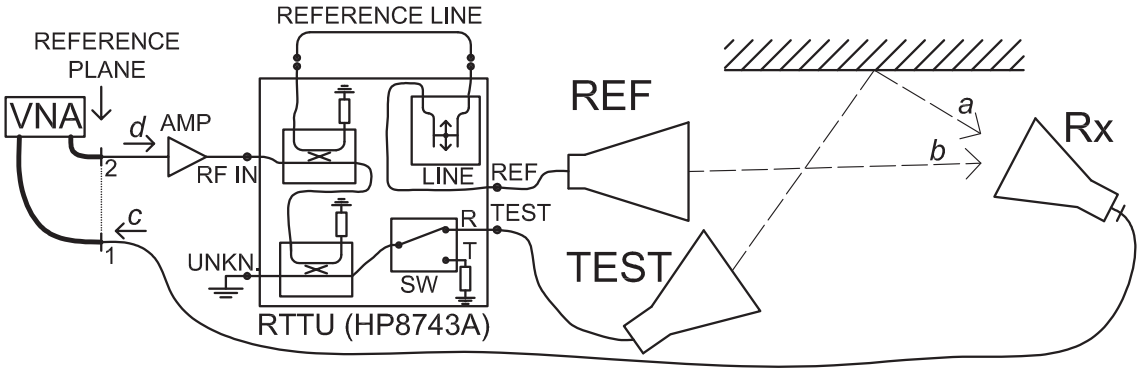

Figure 5.1: Block scheme of the measurement setup.

The new measurement method was experimentally verified using an Agilent E8364A vector network analyzer in the 6 to 12 GHz frequency band. The block scheme of the experimental setup is shown in Figure 5.1 and the measurement setup photo is seen in Figure 5.2. Components of the measurement setup were able to take measurements from 2 to 18 GHz. However a 6 to 12 GHz octave sub-band was used as a sufficiently wide band, compared to standard imaging systems, e.g., [3, 4, 5, 6], for experimental verification.

The microwave signal from port 2 of the VNA goes through a Mini-Circuits ZVA-213S+ microwave amplifier, to compensate for setup losses, into a reflection-transmission test unit (RTTU) HP8743A from Hewlett-Packard which is applied as a power divider and a precise phase shifter using an internal extending line (LINE). The transmitting antenna TEST is controlled by the internal switch SW. The APC-7 short is connected to the unknown port of the RTTU. Three double ridged waveguide horn antennas DRH20 [34] manufactured by the RFspin s.r.o. company with a gain of approximately 13.5 dB at 10 GHz were used for the measurement.

For further calculations let us denote $A_{\mathrm{T}} = a/d$ which is the transmission from VNA port 2 to the output of the Rx antenna via the antenna TEST. Further, let $A_{\mathrm{R}} = b/d$ which is the transmission from VNA port 2 to the output of Rx antenna

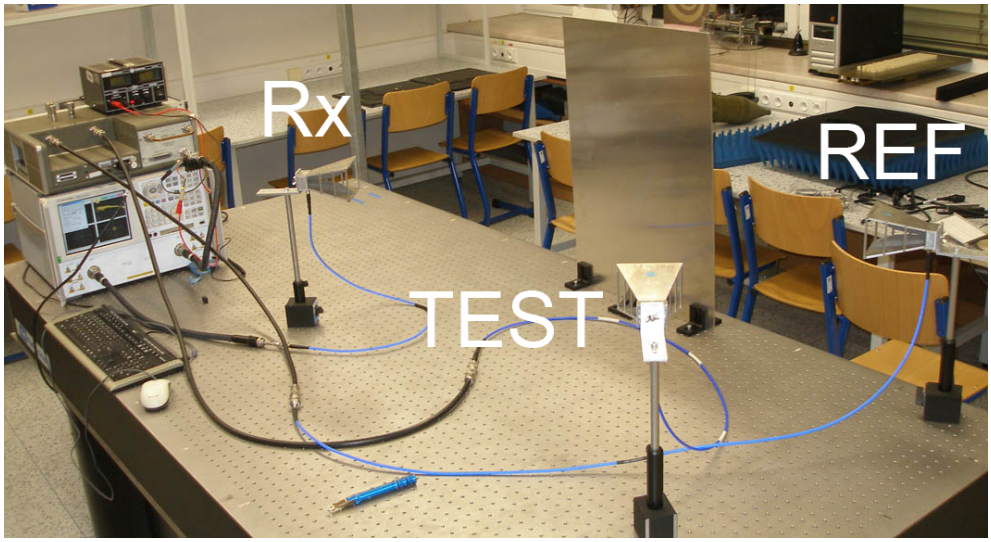

Figure 5.2: Measurement setup. The radiation absorbent material was placed on the metal table during the measurement.

via the antenna REF. And finally let $A_{\mathrm{Rx}} = c/a = c/b$ which is the transmission from the output of the Rx antenna to VNA port 1.

The VNA was calibrated in the reference plane of high-performance test cables connectors with a 3.5 mm Agilent 85052B calibration kit. Measurements consisted of three types of transmission measurements.

5.1 Measurement Procedure

The first measurement was of $S_{12\mathrm{T}}$. The semi-rigid coaxial cable REFERENCE LINE (part of the RTTU) was replaced with two 50 Ω loads on the APC-7 connector and the SW switch was set to position R (Reflection). In this configuration only the TEST antenna was transmitting and $a = A_{\mathrm{T}}d$, $b = 0$, $c = A_{\mathrm{Rx}}(a + b) = A_{\mathrm{Rx}}A_{\mathrm{T}}d$. The measured transmission was

$$S_{12\mathrm{T}} = \frac{c}{d} = A_{\mathrm{Rx}}A_{\mathrm{T}}. \tag{5.1}$$

The second measurement was the measurement of $S_{12\mathrm{R}}$. The REFERENCE LINE was reconnected and the length of the LINE was set to 0 mm. The SW switch was set to position T (Transmission). In this configuration only the REF antenna was transmitting and $a = 0$, $b = A_{\mathrm{R}}d$, $c = A_{\mathrm{Rx}}(a + b) = A_{\mathrm{Rx}}A_{\mathrm{R}}d$. The measured transmission was

$$S_{12\mathrm{R}} = \frac{c}{d} = A_{\mathrm{Rx}}A_{\mathrm{R}}. \tag{5.2}$$

The third measurement was the measurement of $S^{(i)}_{12\mathrm{R+T}}$. The REFERENCE LINE was connected and the SW switch was set to position R. Both the REF and TEST antennas were transmitting simultaneously. The measurement was repeated

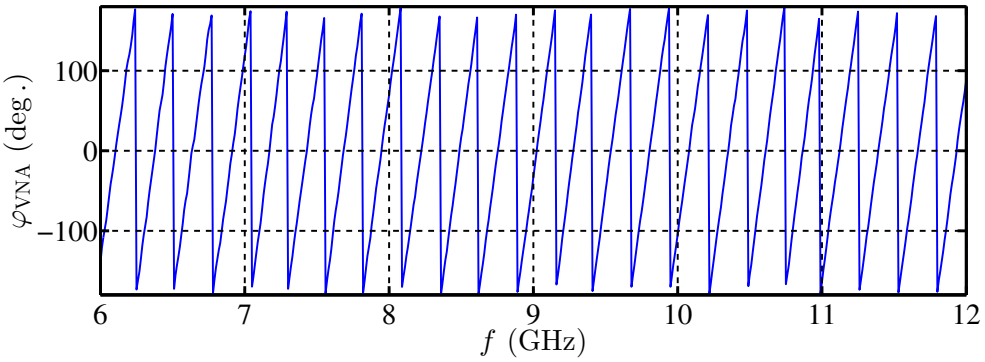

Figure 5.3: The reference phase difference φ_{VNA} identified directly from complex S-parameters measured with VNA.

for $n = 7$ lengths of the extending LINE inside the RTTU from $l_1 = 0\,\mathrm{mm}$ to $l_7 = 30\,\mathrm{mm}$ with 5 mm steps. These lengths represent phase shifts from $\alpha_1 = 0$ to $\alpha_7 \approx 360\,\mathrm{deg.}$ with step approximately 60 deg. at the frequency $f = 10\,\mathrm{GHz}$.

The transmission coefficient $A_{\mathrm{R}}^{(i)}$ of the reference path through the REF antenna depends on the length of the LINE in accordance with

$$A_{\mathrm{R}}^{(i)} = A_{\mathrm{R}} \mathrm{e}^{-\mathrm{j}\alpha_{\mathrm{i}}}. \tag{5.3}$$

for $i = \{1, 2, \ldots, n\}$. The dependence of additional LINE losses on its length was neglected. The waves can be expressed as $a = A_{\mathrm{T}} d$, $b_i = A_{\mathrm{R}}^{(i)} d$ and $c_i = A_{\mathrm{Rx}}(a + b_i) = A_{\mathrm{Rx}} d(A_{\mathrm{T}} + A_{\mathrm{R}}^{(i)})$. We measured n transmission coefficients

$$S_{12\mathrm{R+T}}^{(i)} = \frac{c_i}{d} = (A_{\mathrm{R}}^{(i)} + A_{\mathrm{T}}) A_{\mathrm{Rx}}. \tag{5.4}$$

VNA measurements of complex transmissions $S_{12\mathrm{R}}$ and $S_{12\mathrm{T}}$ allows us to calculate the phase difference φ_{VNA} directly as

$$\varphi_{\mathrm{VNA}} = \angle\left(\frac{A_{\mathrm{R}}}{A_{\mathrm{T}}}\right) = \angle\left(\frac{S_{12\mathrm{R}}}{S_{12\mathrm{T}}}\right) = \angle(S_{12\mathrm{R}}) - \angle(S_{12\mathrm{T}}). \tag{5.5}$$

This value was used as a reference phase difference to verify the results of the proposed method described below. Dependence of φ_{VNA} on frequency is shown in Figure 5.3.

To verify the new method amplitudes of measured S-parameters were used. We need to construct a geometrical representation of the measurement, i.e., calculate the radii R_0 and R_i of the circles, and it is possible with the knowledge of the ratios of received powers. The radii were thus expressed from the absolute values of S-parameters as

$$R_0 = \sqrt{\frac{P_{\mathrm{R}}}{P_{\mathrm{T}}}} = \sqrt{\frac{|A_{\mathrm{R}}|^2}{|A_{\mathrm{T}}|^2}} = \sqrt{\frac{|S_{12\mathrm{R}}|^2}{|S_{12\mathrm{T}}|^2}} = \frac{|S_{12\mathrm{R}}|}{|S_{12\mathrm{T}}|} \tag{5.6}$$

and

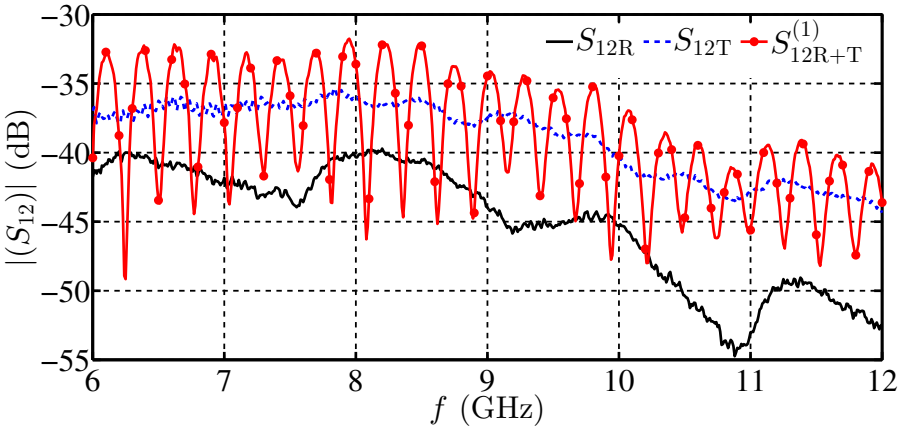

Figure 5.4: Magnitudes of measured transmission coefficients S_{12}. The values $\left|S^{(i)}_{12\mathrm{R+T}}\right|$ for other lengths l_i of the extending line are very similar to the graph of $\left|S^{(1)}_{12\mathrm{R+T}}\right|$, but the minima and maxima are shifted.

$$R_i = \sqrt{\frac{P^{(i)}_{\mathrm{R+T}}}{P_{\mathrm{T}}}} = \sqrt{\frac{\left|A^{(i)}_{\mathrm{R}} + A_{\mathrm{T}}\right|^2}{\left|A_{\mathrm{T}}\right|^2}} = \sqrt{\frac{\left|S^{(i)}_{12\mathrm{R+T}}\right|^2}{\left|S_{12\mathrm{T}}\right|^2}} = \frac{\left|S^{(i)}_{12\mathrm{R+T}}\right|}{\left|S_{12\mathrm{T}}\right|}. \tag{5.7}$$

5.2 Measurement Results

Some of the results of processing measured data at frequency $f = 10\,\mathrm{GHz}$ are stated in Table 5.1. Set phase shifts α_i via the electrical lengths l_i of the extending line are stated in the interval at $(-180, 180]$ deg. The amplitudes of measured S-parameters are $|S_{12\mathrm{R}}| = -45.35\,\mathrm{dB}$, $|S_{12\mathrm{T}}| = -40.55\,\mathrm{dB}$ and using (5.6) results in a radius of $R_0 = 0.575$. The measured magnitudes of transmission S_{12} parameters are depicted in Figure 5.4. It is possible to obtain only absolute values of arguments $\angle(\mathrm{I}_i) = \left|\varphi^{(i)} + \alpha_i\right|$ from the geometrical representation of measurement and another proper intersection point, I_j, is used to obtain the correct sign of phase differences $\varphi^{(i)}$. In Table 5.1 the indexes j of the proper intersection points computed by (4.1) are stated. The actual values $\varphi^{(i)}$ are then computed using (3.21) - (3.24). One of the outcomes of (3.21) or (3.23) is significantly closer to zero, i.e., the sign of individual realizations of $\varphi^{(i)}$ are clearly obtained. If computing uncertainty of measurement is not required, it is possible to compute an average value $\bar{\varphi}$ from all realizations of $\varphi^{(i)}$ and the measurement is complete. However, if it is intended to exploit the redundancy in measurement effectively, uncertainties must be considered.

In our procedure the uncertainties of individual realizations $u\left(\varphi^{(i)}\right)$ are based on a geometrical representation, but we cannot use (4.4) and (4.5) for this representation construction because we do not know the actual value of P_{T} and uncertainties $u(P)$ of the individual power detectors in the VNA. We have to utilize the uncertainty of the magnitude of transmission coefficient measurement of the VNA used which is depicted in Figure 5.5. We assume this type B uncertainty stated in the

i	l_i	α_i	$\lvert S^{(i)}_{12R+T}\rvert$	R_i	$\angle(\mathrm{I_i})$	j	$\Delta\alpha_{ij}$	$\varphi^{(i)}$	U	$\lvert S^{(i)}_{12R+T}\rvert$	$u(R_i)$	$u_g(\angle(\mathrm{I_i}))$	κ	$u(\varphi^{(i)})$
(-)	(mm)	(deg.)	(dB)	(-)	(deg.)	(-)	(deg.)	(deg.)		(dB)	(-)	(deg.)	(-)	(deg.)
1	0	0.0	-40.23	1.037	102.79	5	119.8	-102.79		0.189	0.0108	1.37	0.77	1.1
2	5	-60.0	-47.01	0.475	163.85	3	-60.0	-103.81		0.211	0.0086	2.35	0.86	2.1
3	10	-120.1	-43.57	0.707	136.30	5	-120.1	-103.61		0.200	0.0094	1.09	0.93	1.1
4	15	179.9	-38.64	1.245	78.95	5	-60.0	-100.93		0.185	0.0118	1.97	0.69	1.4
5	20	119.8	-36.67	1.563	14.89	7	-120.1	-104.95		0.181	0.0134	12.0	0.67	8.1
6	25	59.8	-37.29	1.454	47.00	5	60.0	-106.80		0.182	0.0128	3.62	0.65	2.4
7	30	-0.3	-40.38	1.020	104.64	3	-119.8	-104.39		0.189	0.0107	1.33	0.78	1.1

Table 5.1: Results for computation of mean value of phase difference $\bar{\varphi}$ at frequency $f = 10\,\mathrm{GHz}$.

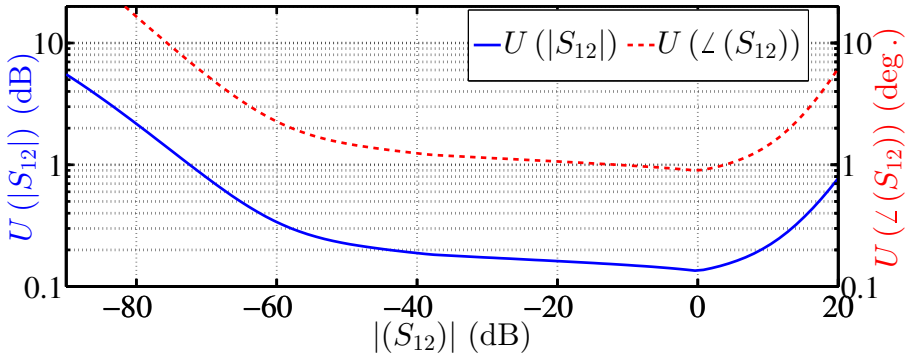

Figure 5.5: Expanded uncertainties ($k = 3$) of magnitude and argument of transmission coefficient measurement of the Agilent VNA E8364A. $BW = 500\,\text{Hz}$, $P_{\text{out}} = -10\,\text{dBm}$, unknown, open, short, match (UOSM) calibration [35] using 3.5 mm calibration kit 85052B, $f = 2 \div 20\,\text{GHz}$. Uncertainty data were obtained from the Vector Network Analyzer Uncertainty Calculator [36] from Agilent Technologies.

datasheet was obtained from measurements with high degrees of freedom [18]. This graph makes it possible to determine the standard uncertainty $u(|S_{12}|)$ belonging to every level of the measured transmission coefficient. The uncertainties of the radii of circles $u(R_0)$ and $u(R_i)$ are possible to obtain by applying the law of uncertainty propagation on (5.6) and (5.7) as

$$u(R_0) = \sqrt{\left(\frac{\partial R_0}{\partial |S_{12\text{R}}|} u(|S_{12\text{R}}|)\right)^2 + \left(\frac{\partial R_0}{\partial |S_{12\text{T}}|} u(|S_{12\text{T}}|)\right)^2}, \tag{5.8}$$

$$u(R_i) = \sqrt{\left(\frac{\partial R_i}{\partial |S_{12\text{T}}|} u(|S_{12\text{T}}|)\right)^2 + \left(\frac{\partial R_i}{\partial |S_{12\text{T+R}}|} u(|S_{12\text{T+R}}|)\right)^2} \tag{5.9}$$

where

$$\frac{\partial R_0}{\partial |S_{12\text{R}}|} = \frac{1}{|S_{12\text{T}}|}\,,\ \frac{\partial R_0}{\partial |S_{12\text{T}}|} = -\frac{|S_{12\text{R}}|}{|S_{12\text{T}}|^2},$$
$$\frac{\partial R_i}{\partial |S_{12\text{T}}|} = -\frac{|S_{12\text{R+T}}|}{|S_{12\text{T}}|^2} \text{ and } \frac{\partial R_i}{\partial |S_{12\text{R+T}}|} = \frac{1}{|S_{12\text{T}}|}.$$

Expanded uncertainties of transmission coefficients using the graph, see Figure 5.5, are $U(S_{12\text{R}}) = 0.205\,\text{dB}$ and $U(S_{12\text{T}}) = 0.190\,\text{dB}$. But for usages of (5.8) and (5.7), it is necessary to use standard uncertainties in linear scale. The transformation is possible using the equation

$$u(S)_{\text{lin}} = \left(10^{\frac{U(S)_{\text{dB}}}{20}} - 1\right) \frac{|S_{\text{lin}}|}{k}, \tag{5.10}$$

where $U(S)_{\text{dB}}$ is the expanded uncertainty of the S-parameter in decibels for coverage factor k, and, S_{lin} is the S-parameter in linear units. This equation is simplified and sufficiently holds if $|S|_{\text{dB}} \ll U(S)_{\text{dB}}$. In this case it is possible to consider the

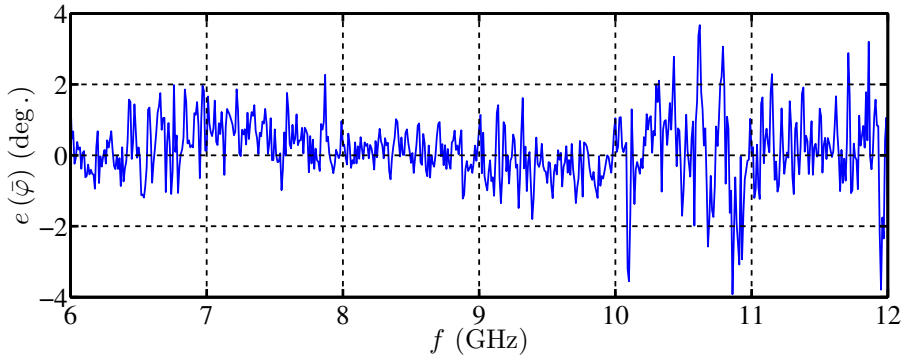

Figure 5.6: The difference between the reference phase difference φ_{VNA} and $\bar{\varphi}$ derived from the scalar measurement. RMS = 0.91 deg.

coverage interval symmetrical around S_{lin}. After obtaining uncertainties in linear scale, the standard uncertainty of radius R_0 using (5.8) is $u(R_0) = 0.0062$. The individual geometrical uncertainties $u_{\mathrm{g}}(\varphi^{(i)})$, with appropriate correction coefficient κ, are stated in Table 5.1. The standard uncertainty $u(\varphi^{(i)})$ of the individual realizations of $\varphi^{(i)}$ is also affected by the uncertainty of the settings of the length of the extending line $u(\alpha_i)$, as stated in (4.11). The uncertainty of the length of the extending line was estimated to be 0.05 mm with uniform distribution, i.e., the standard uncertainty $u(\alpha_i) = 0.35$ deg. at frequency $f = 10$ GHz.

The correction coefficient κ was used as in (4.10) and the actual values of κ were numerically obtained. The dependence of κ is, in this case, a function of the measured S-parameters and the uncertainty of the VNA used. The simulation was made for $|S_{12\mathrm{R}}| \in [-70, -10]$ dB and $|S_{12\mathrm{T}}| \in [-90, 10]$ dB. The mean value of κ for all combinations of measured S-parameters is $\bar{\kappa} = 0.64$ and has a 95% probability of being in interval [0.21, 0.99].

The outcome of computing average value (4.2) from all realizations of $\varphi^{(i)}$ is $\bar{\varphi} = -103.90$ deg. with standard uncertainty (4.12) $u(\bar{\varphi}) = 1.0$ deg. Such a high uncertainty was primarily caused by measurement number $i = 5$ where the resulting uncertainty is $u(\varphi^{(5)}) = 8.1$ deg. To enhance the uncertainty of the arithmetic mean we have to use (4.13) utilizing only realizations of $\varphi^{(i)}$ with sufficiently small uncertainty. The selection of proper realizations of $\varphi^{(i)}$) was done by calculating the standard uncertainty of all combinations of $\varphi^{(i)}$ without repetition. In our case, the best combination, in terms of minimizing the standard uncertainty of sample mean (4.13), were measurements $i \in M = \{1, 3, 4, 7\}$. The others were not used and are shaded in Table 5.1. The final obtained phase difference is $\bar{\varphi} = -102.93$ deg. with standard uncertainty $u(\bar{\varphi}) = 0.59$ deg.

The procedure described above was automated via MATLAB software and the phase difference $\bar{\varphi}$ was obtained for all 601 frequency points measured. The difference between the reference phase difference φ_{VNA}, identified directly from complex transmission coefficients (5.5), and computed phase difference $\bar{\varphi}$ is shown in Figure 5.6. The expanded uncertainty ($k = 3$) of computed phase difference $\bar{\varphi}$ is depicted in Figure 5.7.

The reference phase difference φ_{VNA} was obtained from measured data with

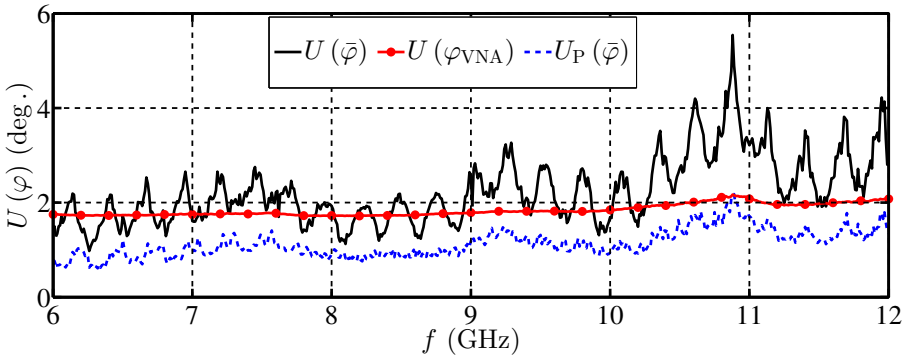

Figure 5.7: Expanded uncertainty ($k = 3$) of the computed phase difference $U(\bar{\varphi})$, expanded uncertainty of the reference phase difference $U(\varphi_{\mathrm{VNA}})$ measured directly by the VNA, and expanded uncertainty $U_{\mathrm{P}}(\bar{\varphi})$ of phase difference computed from simulated measurements with one power detector having uncertainty $U(P) = 0.1\,\mathrm{dB}$.

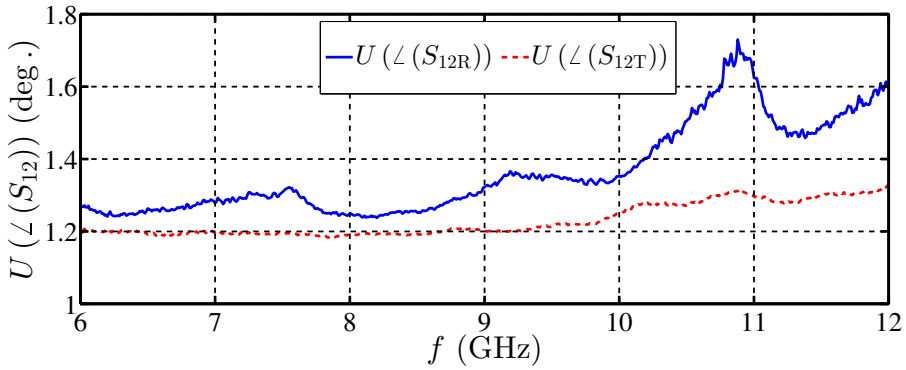

Figure 5.8: Expanded uncertainty ($k = 3$) of the argument of measured $S_{12\mathrm{R}}$ and $S_{12\mathrm{T}}$ by VNA.

some uncertainty. The expanded uncertainty of argument of transmission coefficient measurement $U(\angle(S_{12}))$ is depicted in Figure 5.5 and it is possible to exploit this data to compute the standard uncertainty of the reference phase difference $u(\varphi_{\mathrm{VNA}})$ which can be processed with the application of the law of uncertainty propagation on (5.5) as

$$\begin{aligned} u(\varphi_{\mathrm{VNA}}) &= \sqrt{\left(\frac{\partial\varphi_{\mathrm{VNA}}}{\partial\angle(S_{12\mathrm{R}})}u(\angle(S_{12\mathrm{R}}))\right)^2 + \left(\frac{\partial\varphi_{\mathrm{VNA}}}{\partial\angle(S_{12\mathrm{T}})}u(\angle(S_{12\mathrm{T}}))\right)^2} \\ &= \sqrt{u^2(\angle(S_{12\mathrm{R}})) + u^2(\angle(S_{12\mathrm{T}}))}. \end{aligned} \tag{5.11}$$

This equation is simplified because the argument of S-parameters, i.e., argument of the complex number, is a circular variable. To be precise, the random variable φ_{VNA} with the wrapped normal distribution, or von Mises circular distribution, should be assumed [30]. But when the standard uncertainty of argument S_{12} is much smaller than 180 deg., i.e., $u(\angle(S_{12})) \ll 180\,\mathrm{deg.}$, (5.11) sufficiently holds. The actual

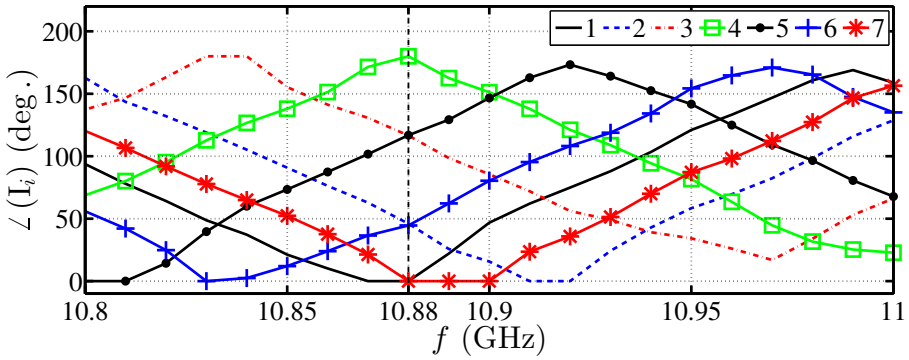

Figure 5.9: Arguments of intersection points $\angle(\mathrm{I_i})$ in frequency band $10.8 \div 11\,\mathrm{GHz}$.

uncertainties of measured arguments of $S_{12\mathrm{R}}$ and $S_{12\mathrm{T}}$ are depicted in Figure 5.8. The resulting expanded uncertainty $u(\varphi_{\mathrm{VNA}})$ is depicted in Figure 5.7.

Regardless the measurement was performed by the VNA the method is based on a measurement with a power detector. Let us derive the expanded uncertainty of the phase difference $U_{\mathrm{P}}(\bar{\varphi})$ computed from simulated measurements with a commercially available power detector with expanded uncertainty $U(P) = 0.1\,\mathrm{dB}$ $(k = 3)$ and constant reference power $P_{\mathrm{R}} = -20\,\mathrm{dBm}$ which is, in practice, easy to achieve. The radii of circles R_0 and R_i have already been obtained from (5.6) and (5.7) and it is possible to compute simulated received powers as $P_{\mathrm{T}} = P_{\mathrm{R}}/R_0^2$ and $P^{(i)}_{(\mathrm{R+T})} = R_i^2 P_{\mathrm{T}}$ from (3.8) and (3.9). These processed measured data, as described in section 3 and 4, provide the final expanded uncertainty of phase difference $U_{\mathrm{P}}(\bar{\varphi})$ depicted in Figure 5.7.

Generally, typical uncertainty dependences of most measurement systems are smooth curves. In our case the uncertainty $U(\bar{\varphi})$ in Figure 5.7 is rippled. It results from the computation procedure which is explained as follows: $n = 7$ measurements with different physical lengths l_i in the reference path were performed. At some frequencies it was possible to obtain the argument of intersection point precisely using most measurements simultaneously. However, the situation was completely different at certain frequencies where it was possible to use only one measurement. The curve $U(\bar{\varphi})$ in Figure 5.7, hence, holds only for our specific measurement with a specifically measured scenario, i.e., a radiated metal plate. With other measured test objects or frequency bands the uncertainty would be different. The same holds for curve $U_{\mathrm{P}}(\bar{\varphi})$.

The worst expanded uncertainty, $U(\bar{\varphi}) = 5.6\,\mathrm{deg.}$, occurs at frequency point $f = 10.88\,\mathrm{GHz}$. Considering the measured S-parameters in Figure 5.4, the $|S_{12\mathrm{R}}|$ has global minimum value of $|S_{12\mathrm{R}}| = -54.7\,\mathrm{dB}$, but this is not the reason for the poor uncertainty. The answer is depicted in Figure 5.9, where the arguments of intersection points $\angle(\mathrm{I_i})$ for all number i of measurements are presented. At the frequency $f = 10.88\,\mathrm{GHz}$, it became a random situation when the outcome of measurements number $i = 1$ and 7 resulted in $\angle(\mathrm{I_1}) = \angle(\mathrm{I_7}) = 0\,\mathrm{deg.}$, for the $i = 4$ $\angle(\mathrm{I_4}) = 180\,\mathrm{deg.}$, and, for $i = 2$ and 6, and $i = 3$ and 5, respectively, the arguments of intersections are the same. It yields in little redundancy in measurement and decreases the precision of measurement.

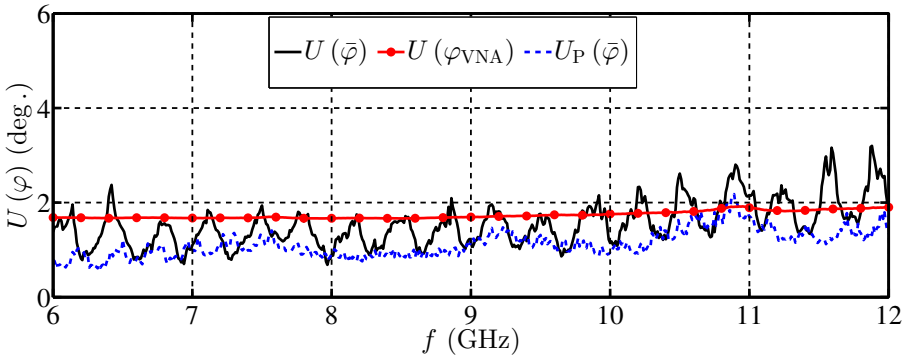

Figure 5.10: Expanded uncertainties ($k = 3$) from the measurement without the test object. $U(\bar{\varphi})$ is the uncertainty of the computed phase difference, $U(\varphi_{\mathrm{VNA}})$ is the uncertainty of the reference phase difference measured directly by the VNA and $U_{\mathrm{P}}(\bar{\varphi})$ is the uncertainty of phase difference computed from simulated measurements with one power detector having uncertainty $U(P) = 0.1\,\mathrm{dB}$.

One way to reduce the uncertainty $U(\bar{\varphi})$ is to use a higher amount of different phase shifts α_i in the reference path. Performing a higher number of measurements increases the probability of obtaining more realizations with precisely obtained intersection points at every frequency point. As can generally be seen from (4.12), a higher number of measurements n leads to smaller uncertainty of $\bar{\varphi}$. Another option how to reduce resulting uncertainty is to use a high-quality power detector with a small uncertainty. Powers measured with smaller uncertainty $u(P)$ provide smaller uncertainties of radii of circles $u(R_0)$ and $u(R_i)$ resulting in a smaller intersection area which in turn lead to a smaller uncertainty of realizations of $\varphi^{(i)}$. As demonstrated in Figure 5.7, using a power detector with expanded uncertainty $U(P) = 0.1\,\mathrm{dB}$ provides comparable, if not better uncertainty than a standard VNA measurement.

Outcomes from the measurements in this article with a configuration corresponding to the configuration in Figure 3.1 are presented. Second verification measurements with the TEST antenna directly irradiating the Rx antenna were also carried out. Such a configuration simulated a potential application of the new method for measuring of the TEST antenna. This measurement was performed with a better power balance and hence the overall measurement uncertainties were also slightly better. The expanded uncertainties of this measurement are depicted in Figure 5.10 and were obtained in the exactly same way as stated above. The random situation similar to that depicted in Figure 5.9 around frequency 10.88 GHz did not occur, because the propagation conditions were different and the measured S-parameters had different phases and modules. Hence, the actual arguments of intersection points were different and the dependence of $U(\bar{\varphi})$ does not exhibit such a significant maximum unlike Figure 5.7.

5.3 Multipath Propagation

It is also extremely important to note that the multipath propagation has no influence on the error signal depicted in Figure 5.6. However, it is clear that between the REF - Rx and TEST - Rx antennas some multi-path propagation, due to reflections from walls and subjects in a room, does occur, but it does not affect the correctness of the verification of the method. The vector transmission coefficient $S_{12\mathrm{T}}$ and $S_{12\mathrm{R}}$ were measured in configuration as depicted in Figure 5.2, but during the measurement of the absolute values of all $|S_{12}|$ parameters, the multipath propagation conditions were the same, thus these scalar transmission coefficients were affected in the same way as the reference vector data. When the microwave imaging is performed in a common places, e.g., security check-points in airports, nondestructive testing in industry etc. the multipath propagation always occurs. Due to this interference the measured S-parameters are obtained with some error and some artifacts appear in the reconstructed image. These artifacts can be considerably reduced by using, for example, the time gating technique [37] widely used in antenna measurements, or, by the modified back-projection method published in [38]. Both techniques require a sufficient difference between the direct and the multipath propagation delay as well as eligible bandwidth and the number of frequency points.

Chapter 6

Scalar Measurement

In the previous section a measurement was performed using VNA as a very precise possibility of how to practically verify basic principles of measurement method. But it is also necessary to practically verify the measurement method with its intended HW configuration, i.e., realize a scalar power measurement with a single detector. During the designing of necessary HW for this measurement we discovered that the design of a wide-band antenna array would be very difficult, so we decided to leave our original intention to provide a multistatic imaging system and rather implement an ISAR measurement technique, which necessarily needs just one receiving antenna instead of an antenna array [39].

6.1 HW Implementation

The specific HW solution was affected by several circumstances. First of all we wanted to use the proposed HW for microwave imaging, hence it was necessary that the HW function in a band as wide as possible due to the relevant spatial resolution, which is directly proportional to the bandwidth. On the other hand we wanted to use the already available HW components and devices at our department and spend just the appropriate amount of money for the fabrication of new components corresponding to the relevance of this work. Another important requirement was to design the whole system to be controllable via personal computer (PC) to provide automated measurement capability.

A proposed measurement arrangement is shown in Figure 6.1. It was necessary to design and fabricate the highlighted blocks to fulfil the appropriate parameters. All antennas were used the same as with the VNA measurement, i.e., DRH20 horn antennas [34]. Usage of these antennas practically resolved the frequency band of the measurement. These antennas work in the frequency band $1.7 \div 20\,\mathrm{GHz}$ and fortunately it suitably matched the necessary parameters of available equipment as cables, connectors, adapters, detector, generator, etc., required for measurement. A Rohde & Schwarz SMF100A [40] generator with operating frequency range $1 \div 43.5\,\mathrm{GHz}$ and output power up to 30 dBm was used.

We have already had several practical experiences with the design of microwave circuits using the RO4003C [41] microwave substrate from the Rogers Corporation and we decided to use it also for this project. Over time we determined that for

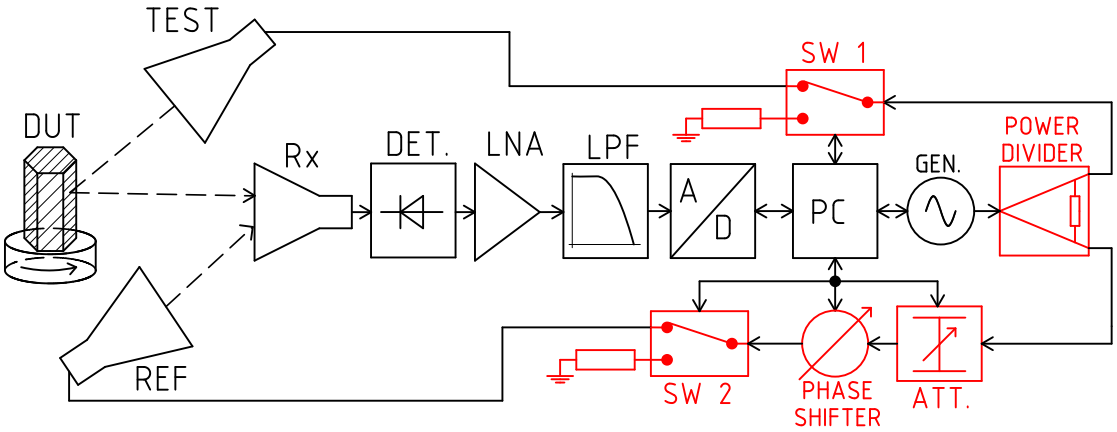

Figure 6.1: Measurement arrangement verifying imaging capabilities of the measurement method. Red blocks represent the microwave components which are to be designed and fabricated.

the precise design of microwave components, i.e., to make the measurement and simulation agree as well as possible, the characterization of substrate permittivity and dielectric losses was necessary. For this purpose we designed an extensive calibration kit containing several calibration standards to possibly use several calibration techniques to perform calibration directly on the grounded coplanar waveguide (CPWG) [42]. The calibration kit assembled with Rosenberger 32K243-40ML5 connectors [43] is depicted in Figure 6.2. For substrate characterization purposes we used the multi-line TRL calibration method [44, 45] using four Line standards with lengths of 3.1, 5.8, 8.1 and 10 mm. The characterization of substrate was performed by fitting measured and calibrated S-parameters of 200 mm long CPWG line with a CST model simulation using "Extract complex permittivity" macro [46, 47]. The obtained substrate parameters are show in Figure 6.3. According to datasheet [41] of this substrate the dielectric constant should be $\varepsilon_r' = 3.38$ at 10 GHz, i.e., approximately 9% lower than measured. Dielectric losses should be $\tan\delta_e = 2.7 \cdot 10^{-3}$ at 10 GHz, but when measured were approximately about 50% higher.

All components mentioned earlier were fabricated on the RO4003C substrate with thickness 0.0087" (≈0.221 mm) and enclosed into custom made metallic boxes equipped with Super SMA connectors model 212-502SF [48] from Southwest Microwave, Inc. In the following paragraphs we provide a detailed description of the individual components.

6.1.1 Power Divider

Due to wide bandwidth of DRH20 horn antennas (over one decade) to fully exploit its possibilities it was necessary to design similarly wideband power divider. According to the achievable bandwidth, losses and isolation of different types of power dividers we chose to design a Wilkinson power divider [49]. This kind of divider can provide bandwidth of up to one decade using a 7-stage design [50] with reasonable requirements for fabrication precision. The impedances of lines and resistors

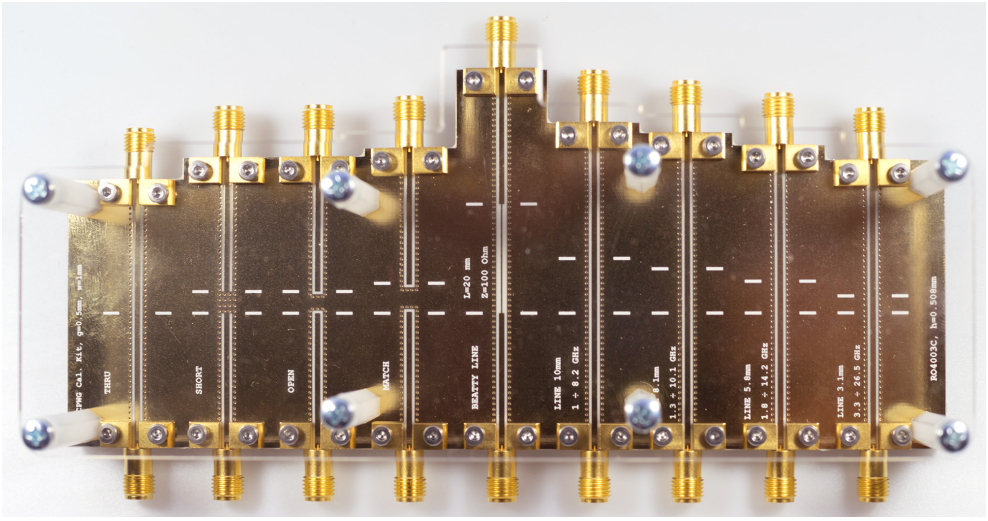

Figure 6.2: Calibration kit used for the characterization of the RO4003C substrate.

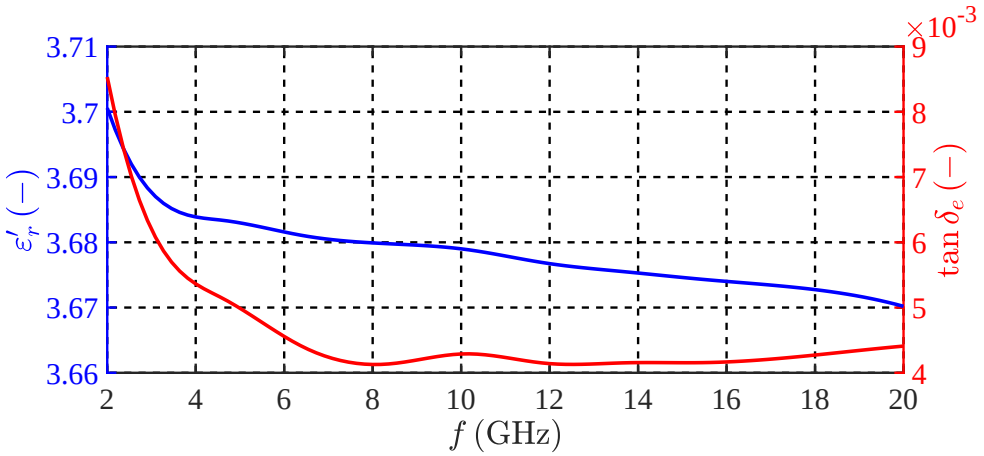

Figure 6.3: Measured relative permittivity and dielectric losses of the RO4003C substrate.

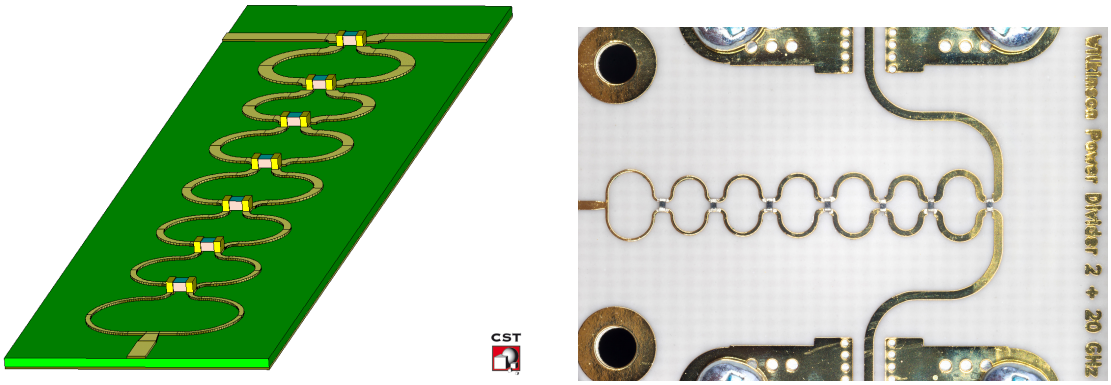

(a) (b)

Figure 6.4: Model of the 7-stage Wilkinson power divider in CST for verification of design and realized structure. The length of the part with branches is approximately 2 cm.

for equal-ripple (Chebyshev) approximation of characteristics with reflections and crosstalk lower than −20 dB are listed in [50]. We modelled, parametrized and optimized the whole Wilkinson structure in AWR Microwave Office while incorporating all microstrip junctions and 0201 surface-mount device (SMD) resistor models. The narrowest line with impedance 89 Ω was 0.12 mm wide, which is still reasonably manufacturable. The usage of SMD components in microwave circuit design is usually a source of discrepancies between simulation expectations and the real properties of the fabricated device. To rigorously characterize all seven resistors using planar calibration standards would be time consuming, hence we decided to simulate the SMD components in CST as 3D physical models including resistor body, soldering pads and resistive layer [51]. Extracted parameters of SMD resistors were then used in AWR simulations and, finally, the whole Wilkinson divider design was verified in CST (see Figure 6.4(a)). A photo of the fabricated divider with assembled 0201 SMD resistors is shown in Figure 6.4(b) and measured S-parameters with a reference plane on SubMiniature version A (SMA) connectors in Appendix A.1.

6.1.2 Absorptive Switches

The requirements for switches were to utilize commercially available switches in an SMD package, obtain reflections on connectors lower than −15 dB, have isolation better than 40 dB and insertion loss as low as possible. All of which having to hold up to 20 GHz. From available and reasonably priced switches we chose single pole, double throw (SPDT) MASW-008322 switches [52] in a 24-lead power quad flat no lead (PQFN) package. For construction of the single pole, single throw (SPST) switch, as required (SW 1 and SW 2 in Figure 6.1), we had to utilize two SPDT switches in the configuration depicted in Figure 6.5(a) and (b). To be possible to control the switches with digital signals with transitor-transistor logic (TTL) levels we utilized the MADRCC0005 driver [53]. Based on our practical experiences and literature [54] we used two 100 Ω 0201 SMD resistors in parallel instead of one 50 Ω

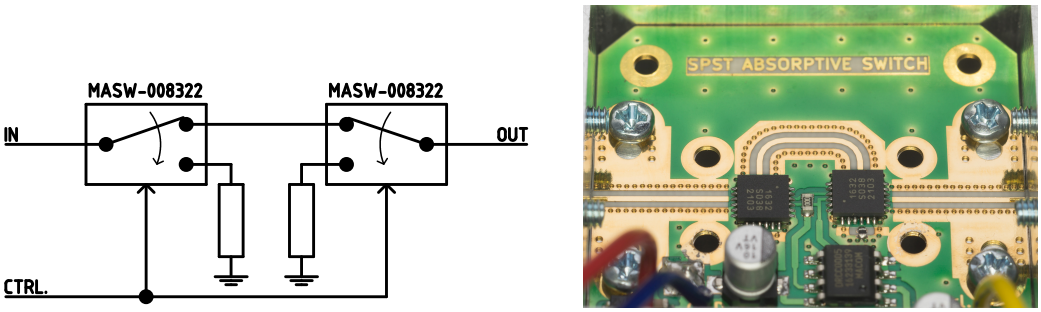

(a) (b)

Figure 6.5: (a) Proposed arrangement of two MASW-008322 switches to create one SPST absorptive switch. (b) Photo of the realized switch.

resistor as a load to achieve lower reflections up to 20 GHz. On the same printed circuit board (PCB) with switches was also the ICL7660S switched capacitor voltage converter [55] to create necessary negative voltage for switches to simplify the usage of the absorptive switch as one block with a single positive supply voltage. Measured S-parameters of the fabricated switch are depicted in Appendix A.2.

6.1.3 Phase Shifter

Most commercially available phase shifters work in a bandwidth of only a few octaves. On the other hand these shifters usually offer a flat phase response almost independent on frequency. Unfortunately, in our application a bandwidth of one decade is needed and hence we decided to develop a phase shifter as digitally controlled switched delays (lines). This style of phase shifter offers us a wide band of operation limited only by switches, but strong frequency dependence of phase shift on frequency and impossible instantaneous setting of shift is expected [56]. It makes this type of shifter inapplicable e.g., as a phase modulator in communications systems, but it is applicable for our purposes.

As already mentioned above in Section 3, in all cases the argument of intersection point lies in interval $\angle(\mathrm{I}_i) \in [0, 180]$ deg. and it is directly influenced by transmission between the TEST and REF antennas and setting of phase shifter. To obtain the correct sign of phase of transmission between the TEST and REF antennas we chose one (the most perpendicular) intersection point from the set of intersections making it beneficial to have another measurement with phase shift $\Delta\alpha_{ij} = \pm 90$ deg. to utilize (4.1). Hence it is necessary to allow set an approximately 90 deg. phase shift in the whole working frequency band.

From one side, it is necessary to have the longest possible electrical length in a vacuum for low frequency at least

$$L_{\mathrm{LF}} = \frac{\lambda_{\mathrm{LF}}}{4} = \frac{c_0}{4 f_{\mathrm{LF}}} \approx 37.5 \text{ mm}, \tag{6.1}$$

where $f_{\mathrm{LF}} = 2$ GHz, and the minimal electrical length for highest frequency maximally

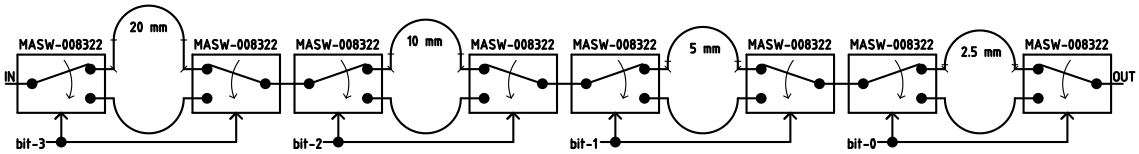

Figure 6.6: Diagram of proposed phase shifter implemented as switched delays. Lengths of lines represent electrical length in a vacuum.

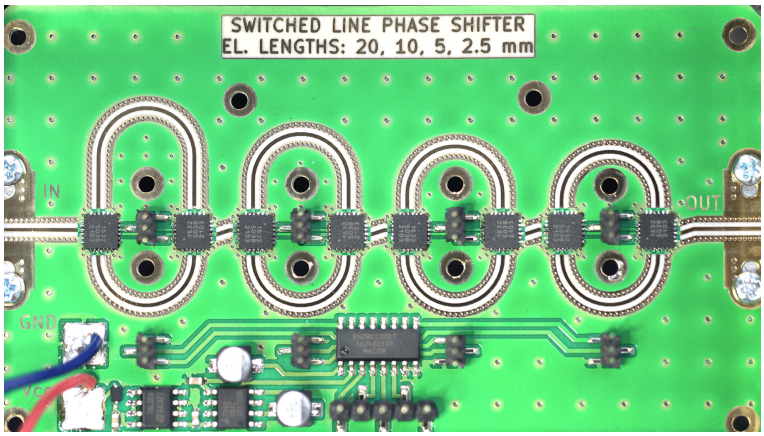

Figure 6.7: Realized 4-bit digitally controlled phase shifter implemented as switched delays.

$$L_{\mathrm{HF}} = \frac{\lambda_{\mathrm{HF}}}{4} = \frac{c_0}{4 f_{\mathrm{HF}}} \approx 3.75\ \mathrm{mm}, \tag{6.2}$$

where $f_{\mathrm{HF}} = 20\,\mathrm{GHz}$. To fulfil these requirements we chose the phase shifter to be 4-bit (16 states) with a 2.5 mm step in the range of $0 \div 37.5\,\mathrm{mm}$. It allow us to set a phase shift with a 6 deg. and 60 deg. step at frequencies 2 and 20 GHz, respectively. This is a compromise between the complexity of the whole phase shifter HW, achievable insertion loss and needed diversity in the measurement to achieve unambiguous results. Switches were used the same (MASW-008322 [52]) as in the absorptive switch design and the functional diagram is shown in Figure 6.6. To be possible to control the switches with digital signals with TTL levels we utilized the MADRCC0007 quad driver [57]. The PCB of switch also includes source of a negative voltage (ICL7660S) for switch's supply. A photo of fabricated shifter is shown in Figure 6.7 and measured S-parameters for all states of phase shifter in Section A.3.

6.1.4 Attenuator

An attenuator is needed to match the values of received powers P_{T} and P_{R} to ensure $P_{\mathrm{T}}/P_{\mathrm{R}} = 0\,\mathrm{dB}$ to achieve minimal uncertainty of $\angle(\mathrm{I}_i)$ as depicted in Figure 4.10. This attenuator should be mainly capable of equalizing the reflectivity of DUT, because free space loss (FSL) in the test and reference channel would be almost the same (difference 6 dB for double distance). The attenuation of the signal in the

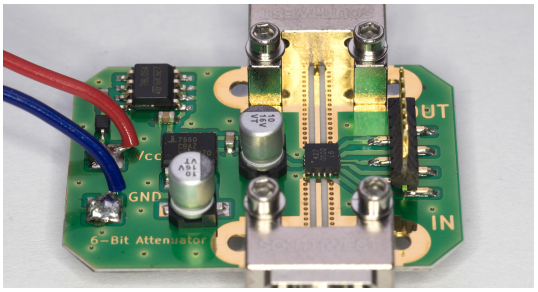

Figure 6.8: Realized 6-bit digitally controlled attenuator using MAAD-011021.

phase shifter ($\approx 5 \div 20\,\mathrm{dB}$) can be easily balanced with the gain of the REF antenna, which is directly heading the Rx antenna. Hence we decided to utilize the digitally controlled 6-bit attenuator MAAD-011021 [58] with a 0.5 dB step working from DC to 30 GHz. A photo of fabricated attenuator, including a negative voltage supply with ICL7660S, is shown in Figure 6.8 and measured S-parameters are shown in Appendix A.4.

6.1.5 Reference Path Setup

All components described above were connected together to create a core microwave multistate circuit of verifying measurement. A photo of the system is depicted in Figure 6.9. The system is generally a 3-port circuit offering 12-bit controlling (six for the attenuator, four for the phase shifter and $2\times$ 1 for two switches) with 4096 states in total. However, for the measurement procedure described in Section 3 the states where both switches are turned off are not practically important. Hence we can conclude that realized system offers $2^{10} = 1024$ unique combinations of attenuations and phase shifts in reference path, which is sufficient for getting unambiguous measurements with sufficient dynamics for imaging purposes.

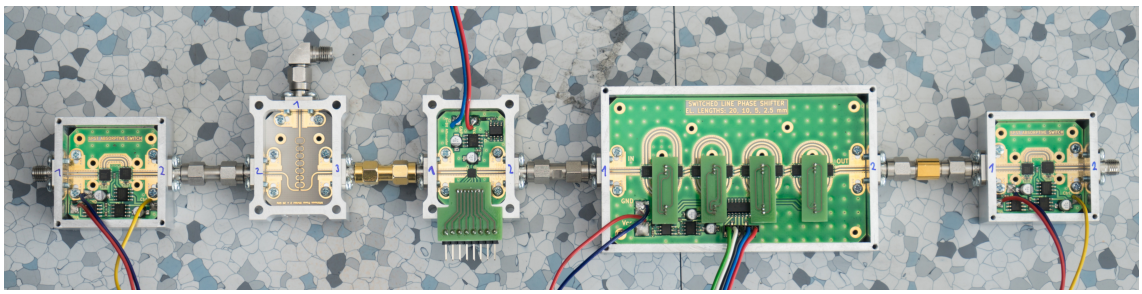

Figure 6.9: Realized microwave setup of the multistate system for the verifying measurement.

Because of the high phase sensitivity of the measurement method and the utilization of SMA and 3.5 mm junctions for connecting all components together, it was necessary to characterize the whole setup by additional vector measurements. Multiple reflections occur in the system which is not possible to predict without

precise knowledge of all junction parameters. Hence we made the full 3-port measurement of the assembled system for all 4096 states, but it is important to show just the 1024 achievable transmission states in reference path. The remaining results are not so important and it would need extensive space to present them in a feasible way. The relative transmission of the reference path of the system is depicted in Figure 6.10. The reference state was chosen as the state with the attenuator set to 0 dB and the phase shifter set to a 0 deg. shift. Measurement results are shown for just a few frequencies to present a preview of the behaviour of relative transmission in the reference path. It can be seen that at all frequencies the achievable attenuation is approximately from -32 to 0 dB and that the achievable phase shift is highly frequency dependent. At the lowest frequency 2 GHz the maximal achievable phase shift is maximally ≈ 90 deg. and with frequency increasing up to 7.5 GHz the coverage of the phase shift also increases. At frequency 7.5 GHz the coverage of the polar plot is the most dense. For further increasing frequencies the achievable states overlap because of the excessive length of the lines in the phase shifter and coverage of achievable transmissions is uneven. The sparsest coverage occurs at the highest frequency 20 GHz where the majority of achievable phase shifts is distributed around 60 deg. steps. It can be also seen that for some particular settings the achievable absolute value of relative transmission is $|\Delta S_{21}| > 0$ dB. This is caused by multiple reflections in the system. These reflections generally worsen the linearity of the settings of achievable transmissions but in our case it is not a problem because we measured complete 3-port parameters over a full operating frequency range for all digital states. Hence we know precisely the relative transmission between two arbitrary digital states which is necessary for the computation of transmission between the Rx and TEST antennas.

6.2 Measurement procedure

The measurement setup was arranged as shown in Figure 6.11. A metallic plate, with 40 cm long sides, was used as the DUT and several absorptive materials were used to suppress potential multi-path propagation. A Rohde & Schwarz SMF100A [40] was used as the signal generator with all antennas being DRH20 [34]. The Krytar 201B power detector [59], consisting of a zero bias Schottky diode working from 10 MHz to 20 GHz and connected directly to the Rx antenna, was used. An external audio sound card Sweex SC016 with line input incorporating integrated double 16-bit analog-to-digital converter (ADC) CM6206 [60] with maximal sampling frequency 48 kHz was used as the ADC.

The whole measurement setup was arranged in a standard laboratory instead of an anechoic chamber, because we wanted to make the measurement method also work in standard environment. First, we tried to utilize 1 kHz chopping (square wave amplitude modulation) to make it possible to use capacitively coupled amplifiers and to reduce 1/f noise [61]. During the practical measurement we discovered a serious problem with interference, mainly with the Wi-Fi signal and other wireless services, which significantly increased the uncertainty of measured received power. Hence it was necessary to come up with some diversity technique, which could enable us to share the frequency spectrum with other wireless services. We chose a direct-

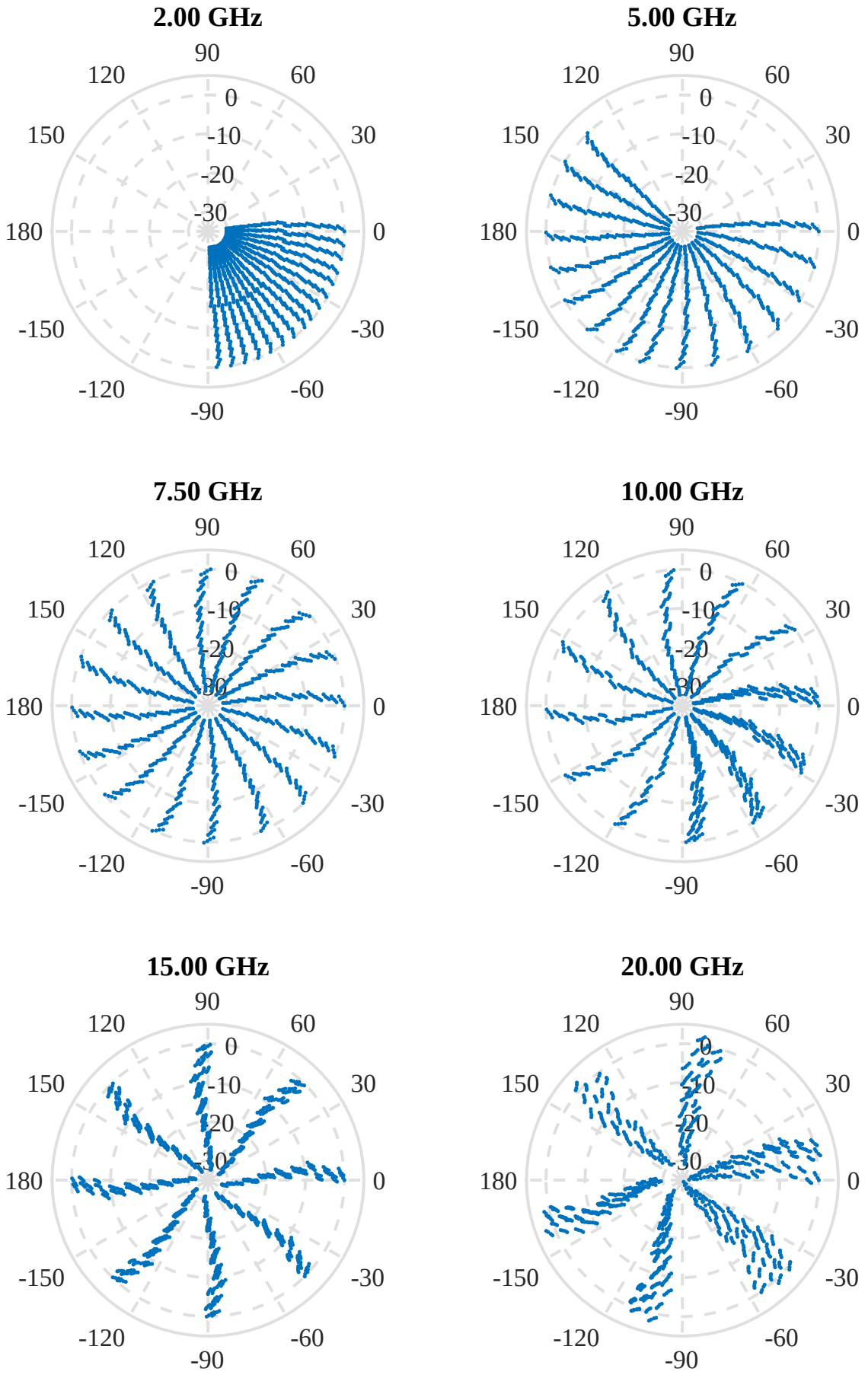

Figure 6.10: Achievable relative transmissions in reference path. It is possible to set 2^{10} (1024) independent states.

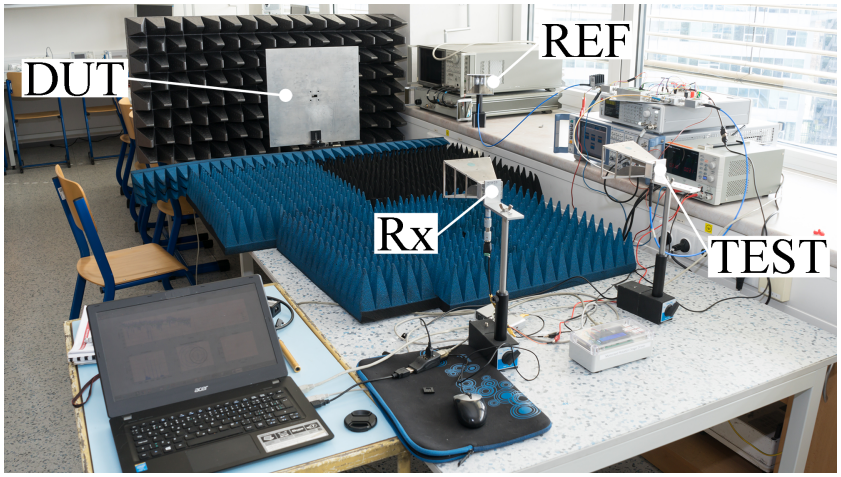

Figure 6.11: Arrangement of scalar measurement using three horn antennas and a metallic plate as the DUT.

[t]

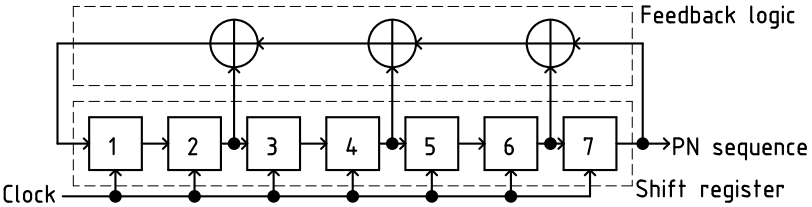

Figure 6.12: Shift register of length $m = 7$ generating MLS with length $m^2 - 1 = 127$ bits. The feedback circuit consists of modulo-2 adders and are summing bits from register positions 7, 6, 4 and 2.

sequence spread-spectrum modulation using a pseudo-noise (PN) binary sequence, which provides great interference immunity ([62]). We used a maximum-length sequence (MLS) binary code a length of 127 bits offering us an $\approx 40\,\mathrm{dB}$ processing gain, which was a compromise between interference cancellation, time consumption of measurement and the computational cost of demodulation. We implemented an MLS generator as shift register with logic feedback circuit according to Figure 6.12. The shift register has $m = 7$ flip-flops (two-state memory stage) and feedback consists of modulo-2 adders. The initial state of memory could be arbitrary except for all zeros and for every clock pulse the bits in the register are shifted to the right and a new feedback bit is computed in the feedback circuit. There exist several possibilities how to construct the feedback circuit for every length of register ([62]), but all sequences are equivalent for our purposes. Generally the period of the PN binary sequence generated by the shift register with proper feedback can be maximally $m^2 - 1$. We utilized feedback circuit summing bits from register positions 7, 6, 4 and 2 and the resulting MLS and its circular autocorrelation function is shown in Figure 6.13. The autocorelation properties of MLS are highly beneficial for detecting the actual PN sequence under low SNR conditions.

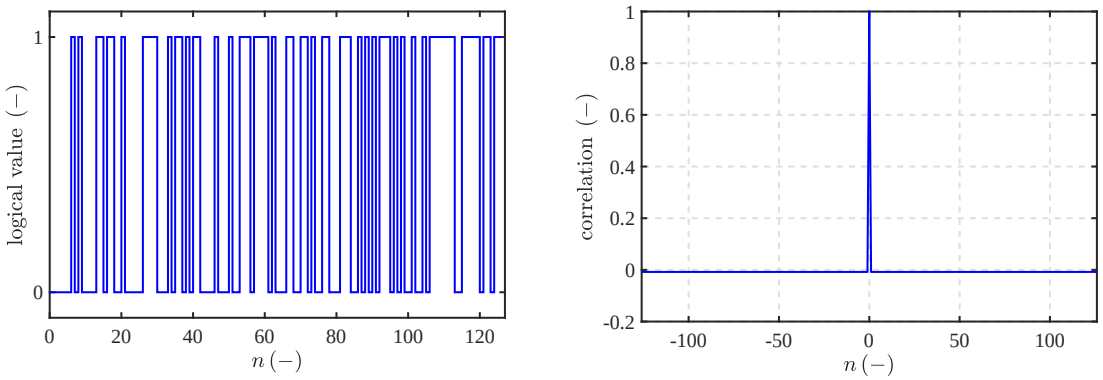

(a) (b)

Figure 6.13: Time dependence of utilized MLS and its cyclic autocorrelation function.

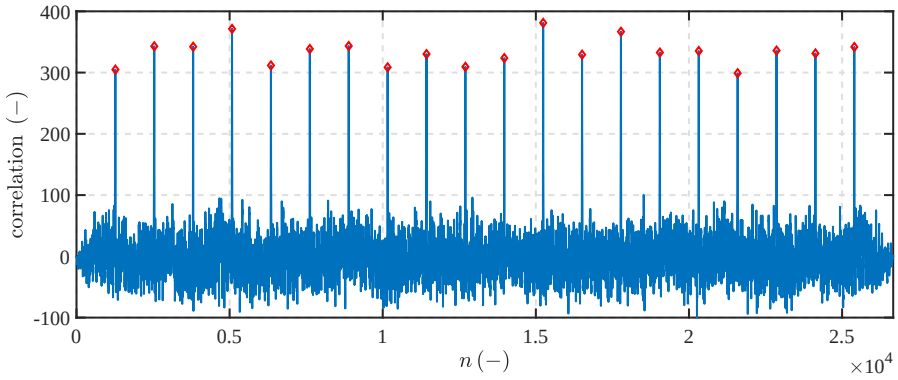

Figure 6.14: Correlation between a recorded signal containing 20 PN binary sequences from Figure 6.13 with 10 samples per bit and a copy of the sequence. Shown case is for SNR = −10 dB and correlation peaks can still be easily detected.

To measure received power on the Rx antenna precisely utilizing spread-spectrum modulation, we calibrated a power detector connected according to Figure 6.15. The signal from the microwave generator was chopped by an MLS binary sequence from an HMF2550 [63] arbitrary wave generator and detected by the detector. The detected signal was amplified by the amplifier and digitized by an ADC. For further processing we utilized MATLAB for the computation of correlation between a copy of the PN sequence and the recorded detection signal. Output of correlation consists of an easily detectable series of peaks whose height carries information about detected microwave power by the detector. It is possible to exploit the fact that the correlation of long-recorded signal consisting of n periods of an MLS contains the same number of peaks with previously known span (see Figure 6.14). We implemented the method for finding correct peaks also for low SNR utilizing the knowledge of the mutual peaks span. For reducing power measurement uncertainty we calibrated the detector using a signal containing a series of 20 binary sequences and calculated the average from the detected peaks. It enabled us to characterize the power detector in a power

range of $-55 \div 0\,\mathrm{dBm}$, where the lowest detected voltage had an amplitude in the order of $0.1\,\mu\mathrm{V}$. A calibration curve of the Krytar 201B power detector is shown in Figure 6.16 and shows minimal frequency dependence. The relative ripple of calibration data over the frequency is shown in Figure 6.17 and attains values in order of units of percentile points.

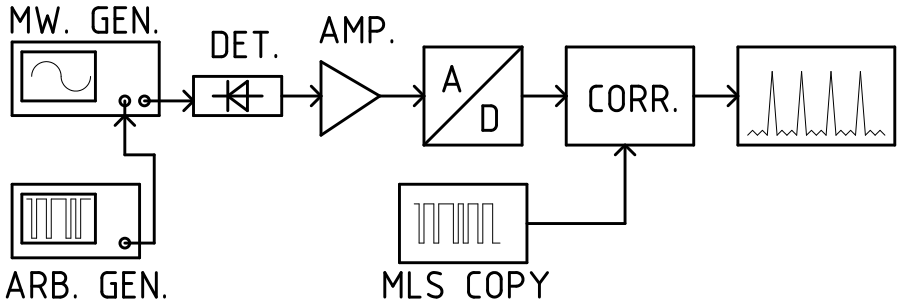

Figure 6.15: Scheme of detector calibration system.

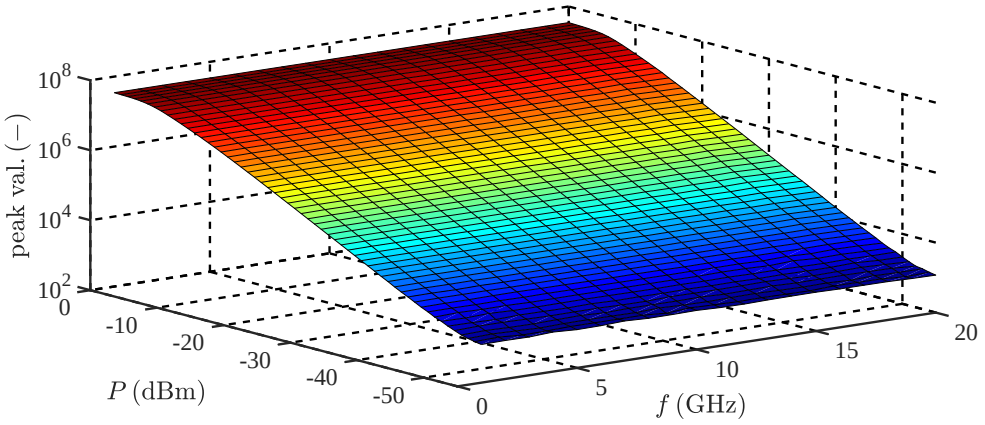

Figure 6.16: Calibration curve of the Krytar 201B detector.

We implemented extensive controlling software for autonomous measurements in MATLAB. The software enabled us to set measuring frequency points, set digital states of the multistate system in the reference path of the setup, measure received power on the Rx antenna utilizing a correlation with a copy of a PN sequence using an extrapolated calibration curve of the detector, adaptively control settings of the attenuator in the reference path to obtain similarly received powers P_R and P_T to reduce uncertainty of measurement, and, in accordance to received powers evaluate phase difference φ between waves in the reference and test path and set the angle of rotation of the DUT. The phase shift φ computation (Section 3) needs the actual settings of the reference path settings, hence extrapolated measured data shown in Figure 6.10 were utilized for that purpose.

Scalar measurement in the configuration from Figure 6.1 was performed in a frequency band $2 \div 20\,\mathrm{GHz}$ with $n_\mathrm{f} = 128$ frequency points and the DUT was rotated

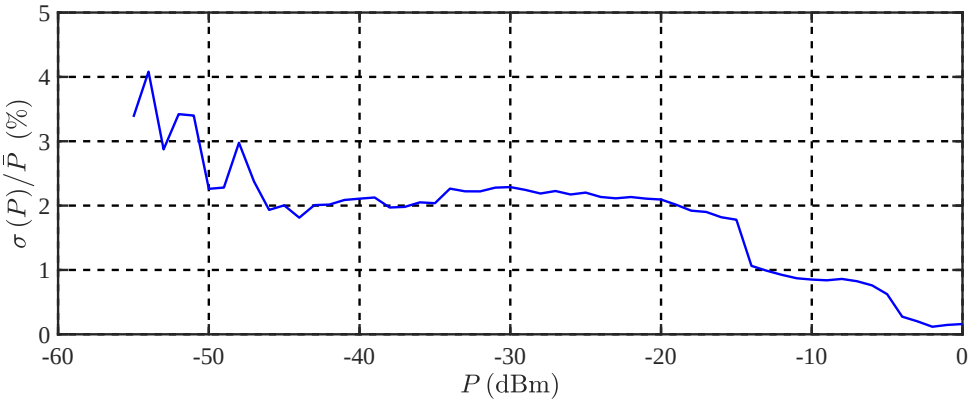

Figure 6.17: Relative standard deviation of detected power using the Krytar 201B detector over frequency range $2 \div 20$ GHz.

all the way round with step $\Delta\theta = 5$ deg., i.e., in 72 points. The distance between the Rx and TEST antennas was 40 cm and the distance from the antennas to the DUT was 1.7 m. The half-power beamwidth of the DRH20 antennas is minimally 20 deg., i.e., a circle with a diameter of at least 70 cm is sufficiently illuminated which is enough for a 40×40 cm plate. The bandwidth of the measurement was $BW = 18$ GHz and this designated the achievable resolution in a range according to (2.7) as ≈ 1 cm, which is sufficient for our purposes. With the described measurement procedure we measured the frequency dependence of transmission between the Rx and TEST antennas for every rotation angle θ. To represent transmission Γ_{DUT} in time domain, as usual in a time analysis in vector measurement technique [24], we utilized an inverse discrete Fourier transform (IDFT) implemented as an IFFT in MATLAB. The time step (time resolution) of the time signal is $\Delta t = 1/\mathrm{BW}$ and the maximal reachable time delay is $t_{\max} = M\Delta t$, where M is the length of the time signal. We used interpolation in frequency by factor 2, hence $M = 2n_{\mathrm{f}}$ and the maximal unambiguous range is $R_{\max} = t_{\max} c_0 = 2.13$ m. It is enough for the imaging of the DUT at 1.7 m distance, but other unwanted reflections behind the DUT position can degrade the reconstructed image. Fortunately, the presence of absorptive material around the DUT and additional free space losses to the closest wall in the room reduced the influence of unwanted reflections to an acceptable level.

6.3 Image Reconstruction

The set of measured transmissions between the TEST and Rx antennas (for all rotation angles θ) was processed by IFFT to compute the range profiles in a time domain. We assume that the wave propagating through the free space has speed of light c_0, hence the computation of the equivalent distance range from the time domain is $d = tc_0$. Computed range profiles for several rotation angles θ from range $[0, 90]$ deg. are shown in Figure 6.18. The range profiles represent the propagation path of a wave from the TEST antenna to the Rx antenna through a reflection from the DUT. It can be seen that maximal values around DUT distance 1.7 m are

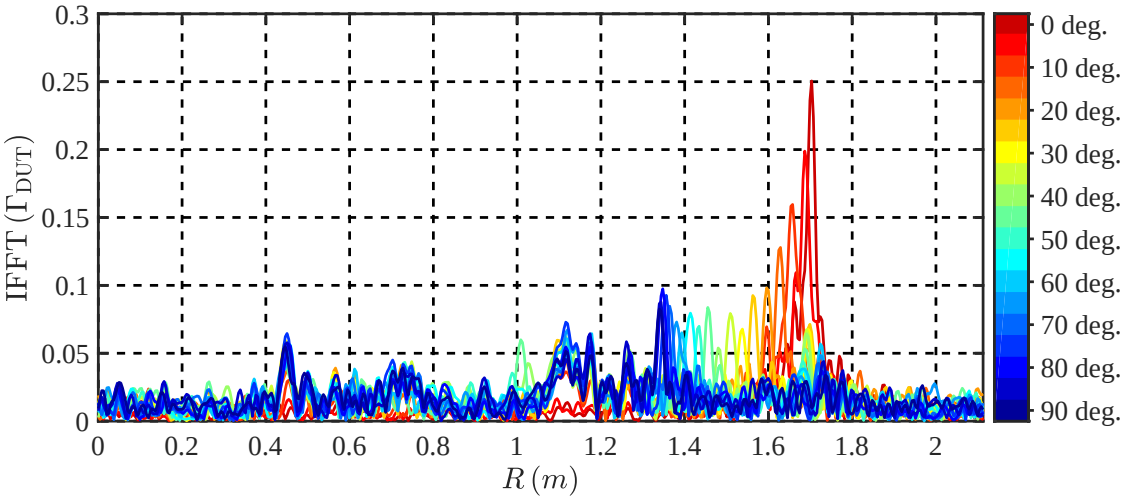

Figure 6.18: Measured range profiles of a metallic plate for several rotation angles θ. Range profiles were computed as the IFFT of Γ_{DUT}. According to rotation angle, a shift of maximal reflection and size of reflection can be clearly seen.

moving toward zero distance according to the actual rotation angle. It is caused by the effective movement of the main reflection part of the metallic plate during the rotation. The range profiles are measured in a reflection arrangement, hence the distance changes are doubled. It corresponds to the measured range profiles where the maximal peak shift is about two times that of half of the metallic plate size, i.e., 40 cm, because the plate is rotating around its vertical axis. The magnitude of the reflection is also dependent on the angle of irradiation and should roughly represent the dependence of the RCS of the metallic plate.

A collection of all range profiles for all rotation angles θ is shown in Figure 6.19 (a). It creates a so-called sinogram and clearly shows the distances of the main reflection points on the DUT depending on the angle of rotation. The sinogram is the main source of data for further processing, hence it is suitable to be free of any unwanted clutters. For that purpose we applied a background subtraction technique [64] which satisfyingly dealt with antenna crosstalk and static background reflections. Artificial targets created by the mirroring of surrounding objects via the flat highly reflective DUT cannot be reduced by this technique [65]. Measured sinograms before and after background subtraction application are shown in Figure 6.19. In both sinograms the artificial target can be seen for rotation angle $\theta \approx 140$ and 320 deg. This target was created by a reflection from the measurement equipment and window which was located on the right side of the DUT, because reflected wave from the DUT was reflecting back to the Rx antenna through this equipment and window. These targets have a physical basis, but their position is changed according to mirroring from the flat surface, and, moreover, they appear only for specific rotation angles.

To obtain a correctly reconstructed image it is necessary to focus the image. The focusing actually consists of a proper shifting of the sinogram, i.e., range profiles, in a range direction to match the center of the sinogram with the center of rotation of the real DUT. Processed sinogram with the main reflections in the center of the

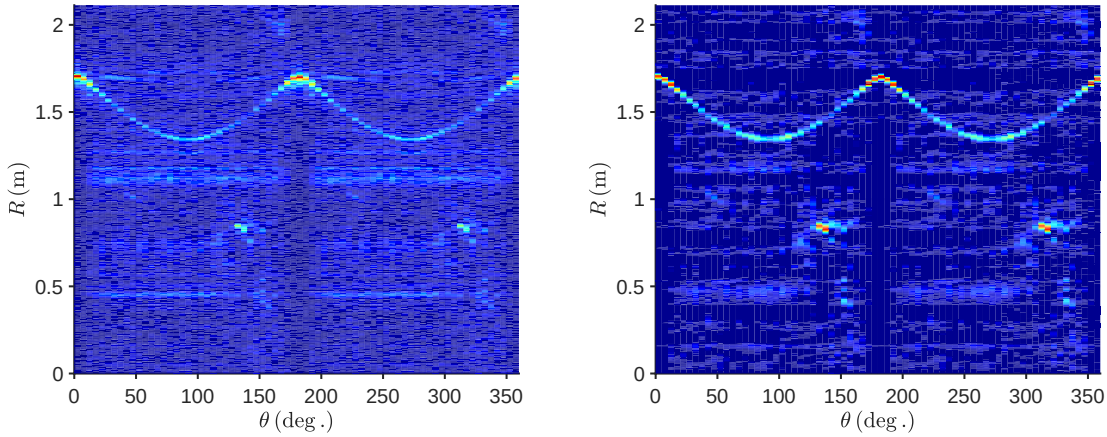

Figure 6.19: Measured sinogram of DUT (metallic plate). (a) Sinogram made with unprocessed range profiles. (b) Sinogram made with background subtracted range profiles.

maximal range is shown in Figure 6.20 (a). It can be equivalently made by multiplying all measured transmissions Γ_{DUT} with a complex exponential with a linearly increasing phase to simulate the DUT changing the distance from the illuminating antenna. Thanks to the translation (time shifting) property of the Fourier transform, the phase shift of the spectrum (transmission coefficient) in the frequency domain represents a time (distance) shift in the time domain [25].

Measured sinograms were processed in MATLAB using an inverse Radon transform [66] (example shown above in Figure 2.5). By default, the Ram-Lak (ramp) filter, which significantly sharper the resulting image (highlights edges), was utilized. The focussed image reconstructed from the shifted sinogram from a scalar measurement is shown in Figure 6.20(b). The data for image processing consists of range profiles in the horizontal plane and the DUT was rotating around the vertical axis, hence reconstructed image represents the horizontal cut across the DUT. The shape of the DUT can be clearly recognized and the dynamic range of the figure is approximately 14 dB (maximal value over a mean value of background).

Separately, we also performed a reference measurement with the VNA directly connected to the Rx and TEST antennas according to Figure 6.21 (a). We directly measured the transmission coefficient S_{21} between the antennas through the DUT reflection. This VNA measurement was processed in the same way as the scalar measurement and the resulting reconstructed image is shown in Figure 6.21 (b). It can be seen that the Radon transform produces a lot of parasitic clutter in the final reconstructed image, especially in the case when we have the rather sparse rotation angle θ coverage, hence between images from the scalar and VNA measurements there is not a significant difference. The dynamic range of the image reconstructed from VNA measurement is approximately 18 dB.

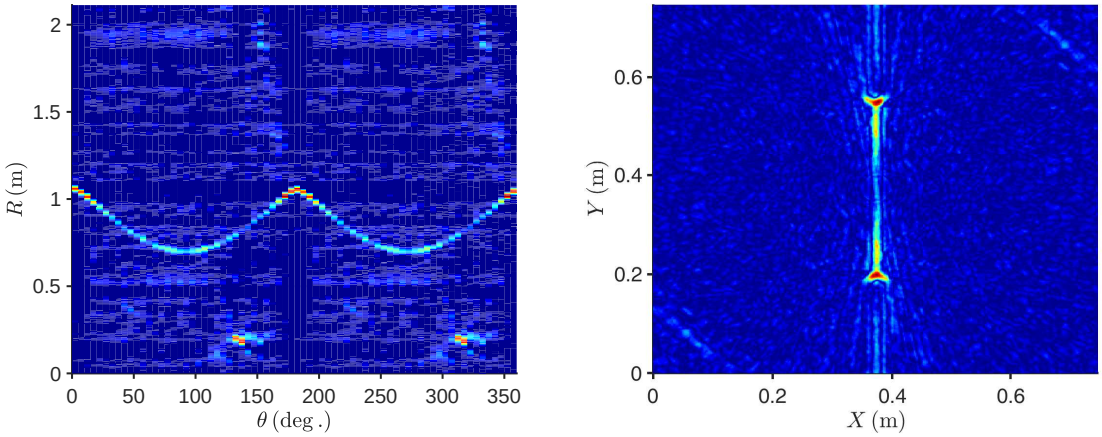

(a) (b)

Figure 6.20: (a) Preprocessing of a sinogram (range profiles) by circular shifting in time (spatial) domain. The main reflection for rotation angle $\theta = 0\,\text{deg.}$ is placed into the center of the maximal unambiguous range $\frac{R_{\max}}{2} \approx 1.07\,\text{m}$. (b) Reconstructed image of the DUT (metallic plate) by inverse Radon transform. The image represents the horizontal cut across the DUT.

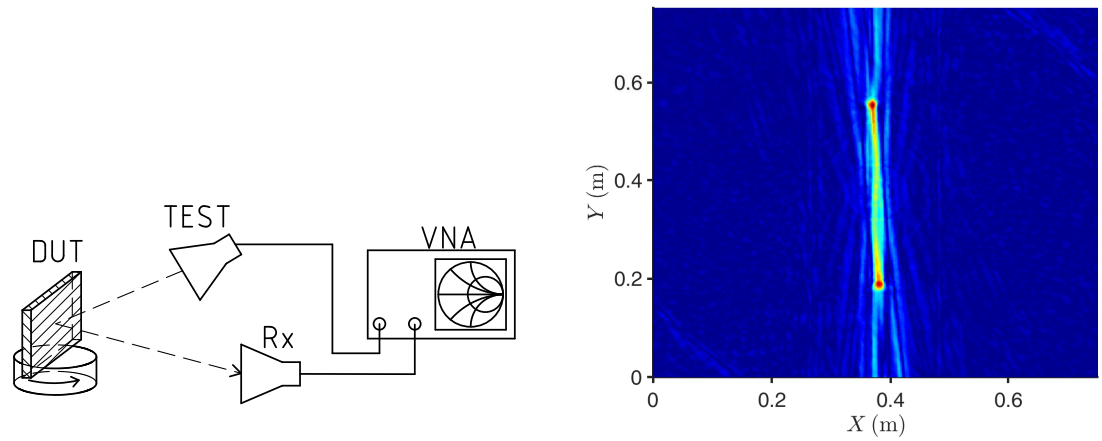

(a) (b)

Figure 6.21: (a) System arrangement for VNA measurement. (b) Image reconstructed from the VNA measurement.

Chapter 7

Conclusion

A new vector measurement method of transmission between two antennas in free space, based only on scalar measurement, was proposed and experimentally verified. The main benefit of the method is the possibility of constructing a microwave measurement system which does not need a delivering reference microwave signal by wire attached to the receiving part of the system. In our concept the reference signal could be led via free space directly to a receiving antenna(s) and, utilizing just the scalar power detection without any frequency conversion, it is possible to measure the complex transmission between two antennas in bistatic or multistatic arrangement, respectively. It makes this system significantly cheaper than using a standard measurement incorporating a VNA. Moreover, the method itself is not limited by the frequency band of the application. Applications in a higher frequency band are limited only by the features of the hardware components supposing an acceptable power balance in the measurement system.

The mathematical description of the method makes the geometrical interpretation of the measurement possible providing an illustrative estimation of measurement uncertainties. The geometrical approach provides a rather pessimistic estimation of uncertainty. Proper determination of uncertainty of measurement is hardly feasible in an analytical way because, in ordinary practical situations, the PDF of the transmission coefficient is significantly different from bivariate normal distribution. It occurs for specific cases when strong destructive interference occurs and the measured power is comparable to the uncertainty of measurement. To exploit even these very uncertain measurements then requires the knowledge of the standard deviation of a non-normal distribution. Fortunately, these uncertain measurements can not relevantly decrease the measurement uncertainty, hence eliminating those measurements is close to ideal solution. Therefore, a simple geometrical representation can, at least, point out highly uncertain measurements which are best eliminated from the whole set of measurements. We also provided a numerical solution of uncertainty determination, which is based on the MCM. This solution offers a determination of the calibration constant κ which corrects the geometrically obtained uncertainty to get a more precise estimation of measurement uncertainty. To correctly obtain the calibration constant κ it is necessary to know the uncertainty of the power detector, which can be determined on the basis of statistical processing like the uncertainty of Type A, or from a datasheet of the detector. A verification measurement in the

$6 \div 12\,\mathrm{GHz}$ frequency band was carried out. This measurement verified that the proposed method can offer a comparable or more precise phase measurement of the transmission coefficient, with respect to the properties of the applied power detector and amount of redundancy, than by using a standard VNA.

A simplified system utilizing one receiving antenna was designed and built and carried measurement provided data for image reconstruction using an ISAR method. We wanted to provide a functional system out of an anechoic chamber, hence it was necessary to deal with interference from wireless communication systems. We decided to utilize a direct-sequence spread-spectrum modulation of transmitted signals which provided satisfactory interference cancellation. Unfortunately, usage of this modulation method made the signal processing (demodulation) significantly demanding in comparison with widely used on-off keying (chopping). A measured set of transmission coefficients for every rotation angle θ was used for reconstructing the DUT (metallic plate). With the same arrangement we also carried out measurements with the VNA allowing us to compare results from both significantly different measurement principles. Generally, the results from the VNA are better mainly because of the higher dynamic range which is caused by the heterodyne principle which utilizes a narrow intermediate filter. On the other hand, our scalar measurement uses direct detection in the whole working band which significantly increases the noise floor of the measurement.

Due to the fundamental principle of the method, which needs several scalar measurements to obtain vector data, measurement time will take a correspondingly longer time compared to a VNA vector measurement. However, the implementation of our method needs, in principle, simple, common hardware components unlike the VNA and represents a viable method for microwave imaging or antenna measurements. However, even if the components needed for the measurement system are rather simple (power divider, switches, attenuator, phase shifter), to our knowledge it is very hard to find commercially available parts on the market capable of providing all proper parameters for utilization in the proposed system. Hence, the need of an extensive design of microwave components is necessary, while the VNAs are more and more popular and more widely available, thanks to the increased effort to produce them as simply as possible with no screen or buttons, widely utilizing custom MMIC and fully controllable remotely. And moreover for most imaging applications in monostatic or multistatic arrangement, it is necessary to provide only the unidirectional measurements of reflection S_{11} or transmission S_{21}.

Bibliography

[1] S.S. Ahmed, A Schiessl, F. Gumbmann, M. Tiebout, S. Methfessel, and L. Schmidt. Advanced microwave imaging. *Microwave Magazine, IEEE*, 13(6):26–43, Sept 2012.

[2] M. Soumekh. Bistatic synthetic aperture radar inversion with application in dynamic object imaging. *Signal Processing, IEEE Transactions on*, 39(9):2044–2055, Sep 1991.

[3] S.S. Ahmed, A Schiessl, and L. Schmidt. A novel fully electronic active real-time imager based on a planar multistatic sparse array. *Microwave Theory and Techniques, IEEE Transactions on*, 59(12):3567–3576, Dec 2011.

[4] D.M. Sheen, D.L. McMakin, and T.E. Hall. Three-dimensional millimeter-wave imaging for concealed weapon detection. *Microwave Theory and Techniques, IEEE Transactions on*, 49(9):1581–1592, Sep 2001.

[5] K.B. Cooper, R.J. Dengler, N. Llombart, B. Thomas, G. Chattopadhyay, and P.H. Siegel. Thz imaging radar for standoff personnel screening. *Terahertz Science and Technology, IEEE Transactions on*, 1(1):169–182, Sept 2011.

[6] F. Friederich, W. Von Spiegel, M. Bauer, Fanzhen Meng, M.D. Thomson, S. Boppel, A Lisauskas, B. Hils, V. Krozer, A Keil, T. Loffler, R. Henneberger, AK. Huhn, G. Spickermann, P.H. Bolivar, and H.G. Roskos. Thz active imaging systems with real-time capabilities. *Terahertz Science and Technology, IEEE Transactions on*, 1(1):183–200, Sept 2011.

[7] O. Yurduseven, V. R. Gowda, J. N. Gollub, and D. R. Smith. Multistatic microwave imaging with arrays of planar cavities. *IET Microwaves, Antennas & Propagation*, 10(11):1174–1181, Aug 2016.

[8] S.S. Ahmed, A Schiess, and L. Schmidt. Near field mm-wave imaging with multistatic sparse 2d-arrays. In *Radar Conference, 2009. EuRAD 2009. European*, pages 180–183, Sept 2009.

[9] Glenn F. Engen. The six-port reflectometer: An alternative network analyzer. *Microwave Theory and Techniques, IEEE Transactions on*, 25(12):1075–1080, Dec 1977.

[10] L.C. Oldfield, J.P. Ide, and E.J. Griffin. A multistate reflectometer. *Instrumentation and Measurement, IEEE Transactions on*, IM-34(2):198–201, June 1985.

[11] G. F. Engen. An improved circuit for implementing the six-port technique of microwave measurements. *IEEE Transactions on Microwave Theory and Techniques*, 25(12):1080–1083, Dec 1977.

[12] Cletus A Hoer. A network analyzer incorporating two six-port reflectometers. *Microwave Theory and Techniques, IEEE Transactions on*, 25(12):1070–1074, Dec 1977.

[13] F.M. Ghannouchi and A. Mohammadi. *The Six-Port Technique with Microwave and Wireless Applications*. Artech House, Norwood, MA, USA, 2009.

[14] D. Woods. Analysis and calibration theory of the general 6-port reflectometor employing four amplitude detectors. *Electrical Engineers, Proceedings of the Institution of*, 126(2):221–228, February 1979.

[15] Shihe Li and R. G. Bosisio. Calibration of multiport reflectometers by means of four open/short circuits. *IEEE Transactions on Microwave Theory and Techniques*, 30(7):1085–1090, Jul 1982.

[16] G. P. Riblet and E. R. B. Hansson. Aspects of the calibration of a single six-port using a load and offset reflection standards. *IEEE Transactions on Microwave Theory and Techniques*, 30(12):2120–2125, Dec 1982.

[17] Glenn F. Engen and Cletus A Hoer. Thru-reflect-line: An improved technique for calibrating the dual six-port automatic network analyzer. *Microwave Theory and Techniques, IEEE Transactions on*, 27(12):987–993, Dec 1979.

[18] Bureau International des Poids et Mesures. Jcgm 100:2008 gum 1995 with minor corrections, evaluation of measurement data – guide to the expression of uncertainty in measurement, 2008. [Online; accessed 16-April-2018], Available at `http://www.bipm.org/en/publications/guides/gum.html`.

[19] M. I. Skolnik. *Radar Handbook, 2nd edition*. McGraw-Hill Education, Columbus, OH, USA, 1990.

[20] M. Z. Baharuddin, K. Suto, J. T. S. Sumantyo, H. Kuze, L. T. Sze, J. Y. K. Shen, W. G. Cheaw, and K. V. Chet. Development of a semi-automated sar test-bed. In *2014 IEEE 2nd International Symposium on Telecommunication Technologies (ISTT)*, pages 236–240, Nov 2014.

[21] Y. Izumi, S. Demirci, M. Z. Baharuddin, and J. T. S. Sumantyo. Inverse sar imaging of circularly and linearly polarized synthetic aperture radar. In *2016 International Symposium on Antennas and Propagation (ISAP)*, pages 864–865, Oct 2016.

[22] J. Vancl, P. Cerny, Z. Skvor, and M. Mazanek. Evaluation and correction of cable phase stability in high frequency near-field measurement. In *2008 14th Conference on Microwave Techniques*, pages 1–4, April 2008.

[23] T. Sheret, B. Allen, and C. G. Parini. Phase stable multi-channel antenna measurements on a moving positioner. In *2016 10th European Conference on Antennas and Propagation (EuCAP)*, pages 1–5, April 2016.

[24] M. Hiebel. *Fundamentals Of Vector Network Analysis*. Rohde & Schwarz GmbH & Co. KG, Mühldorfstr. 15, 81671 München, Germany, 2011.

[25] S. Haykin. *Fourier Methods in Imaging*. John Wiley & Sons, Inc., New York, USA, 2010.

[26] J. Hsieh. *Computed Tomography Principles, Design, Artifacts, and Recent Advances, 2nd Edition*. John Wiley & Sons, Inc., New York, USA, 2009.

[27] V. Adler and K. Hoffmann. Spatial vector measurement based on six-port concept. In *Microwave Measurement Conference (ARFTG), 2013 81st ARFTG*, pages 1–3, June 2013.

[28] V. Adler and K. Hoffmann. Six-port spatial electromagnetic wave measurement. *IEEE Transactions on Microwave Theory and Techniques*, 62(12):3161–3171, Dec 2014.

[29] L. Kirkup and R.B. Frekel. *An Introduction to Uncertainty in Measurement*. Cambridge University Press, Cambridge, UK, 2006.

[30] K.V. Mardia and P.E. Jupp. *Directional Statistics*. John Wiley & Sons, Inc., New York, USA, 2000.

[31] Agilent Technologies, Inc., Santa Clara, California, USA. *User's and Service Guide*, 2013. [Online; accessed 7-May-2018], Available at `https://doc.xdevs.com/doc/HP_Agilent_Keysight/85025A%20B%20D%20E%20Detectors%20User%27s%20and%20Service%20Guide%2085025-90063%20%5B14%5D.pdf`.

[32] B.D. Hall. *Notes on Complex Measurement Uncertainty - part 2*. Measurement Standards Laboratory of New Zealand, Lower Hutt, New Zealand, 2012. [Online; accessed 16-April-2018], Available at `http://rf.irl.cri.nz/sites/default/files/files/Notesoncomplexmeasurementuncertainty-part2.pdf`.

[33] Bureau International des Poids et Mesures. Supplement 1 to the "guide to the expression of uncertainty in measurement" — propagation of distributions using a monte carlo method, 2008. [Online; accessed 16-April-2018], Available at `http://www.bipm.org/en/publications/guides/gum.html`.

[34] RFspin s.r.o. *Model DRH20 – Double Ridged Waveguide Horn*. RFspin s.r.o., Prague, Czech Republic, November 2010. [Online; accessed 16-April-2018], Available at `http://www.rfspin.cz/en/antennas/measurement-antennas/drh20`.

[35] A. Ferrero and U. Pisani. Two-port network analyzer calibration using an unknown 'thru'. *IEEE Microwave and Guided Wave Letters*, 2(12):505–507, Dec 1992.

[36] Agilent Technologies. Vector network analyzer uncertainty calculator, September 2017. [Online; accessed 16-May-2018], Available at `http://www.keysight.com/main/software.jspx?cc=US&lc=eng&ckey=1000000418:epsg:sud&nid=-11143.0.00&id=1000000418:epsg:sud`.

[37] S. Loredo, M.R. Pino, F. Las-Heras, and T.K. Sarkar. Echo identification and cancellation techniques for antenna measurement in non-anechoic test sites. *Antennas and Propagation Magazine, IEEE*, 46(1):100–107, Feb 2004.

[38] D.A Garren. Sar image formation uncorrupted by multiple-bounce artifacts. In *Radar Conference, 2002. Proceedings of the IEEE*, pages 338–343, 2002.

[39] M. Cheney. *Fundamentals of Radar Imaging*. Dept. of Mathematical Sciences, Rensselaer Polytechnic Institute, New York, USA, 2008.

[40] Rohde & Schwarz GmbH & Co. KG. *R&S® SMF100A Microwave Signal Generator - Operating Manual*. Rohde & Schwarz GmbH & Co. KG, Mühldorfstr. 15, 81671 München, Germany, 2016. [Online; accessed 16-April-2018], Available at `https://cdn.rohde-schwarz.com/pws/dl_downloads/dl_common_library/dl_manuals/gb_1/s/smf/SMF100A_OperatingManual_en_12.pdf`.

[41] Rogers Corporation. *RO4000® Series High Frequency Circuit Materials*. Rogers Corporation, 100 S. Roosevelt Avenue, Chandler, AZ 85226, 2017. [Online; accessed 16-April-2018], Available at `http://www.rogerscorp.com/documents/726/acs/RO4000-LaminatesData-Sheet.pdf`.

[42] R. N. Simons. *Coplanar Waveguide Circuits, Components, and Systems*. John Wiley & Sons, Inc., New York, USA, 2001.

[43] Rosenberger Hochfrequenztechnik GmbH & Co. KG, D-84526 Tittmoning Germany. *Technical data sheet - SMA Right Angle Jack PCB*, 2016. [Online; accessed 18-April-2018], Available at `http://rosenberger.de/ok/images/documents/db/32K243-40ML5.pdf`.

[44] R. B. Marks. A multiline method of network analyzer calibration. *IEEE Transactions on Microwave Theory and Techniques*, 39(7):1205–1215, Jul 1991.

[45] D. C. DeGroot, J. A. Jargon, and R. B. Marks. Multiline trl revealed. In *60th ARFTG Conference Digest, Fall 2002.*, pages 131–155, Dec 2002.

[46] V. Sokol. *Material properties modeling based on measured data*. CST - Computer Simulation Technology AG, Bad Nauheimer Str. 19,64289 Darmstadt, Germany, 2015. [Online; accessed 16-April-2018], Available at `https://www.cst.com/Content/Events/Downloads/euc2015/7-3-3-Vratislav-Sokol.pdf`.

[47] V. Sokol. *Modeling Material Properties based on Measured Data (webminar)*. CST - Computer Simulation Technology AG, Bad Nauheimer Str. 19,64289 Darmstadt, Germany. [Online; accessed 17-April-2018], Available at `https://www.cst.com/solutions/article/modeling-material-properties-based-on-measured-data`.

[48] Inc. Southwest Microwave. *Super SMA Connector Series*. Southwest Microwave, Inc., 9055 South McKemy Street, Tempe, Arizona, USA, 2012. [Online; accessed 17-April-2018], Available at `http://mpd.southwestmicrowave.com/showImage.php?image=819&name=SuperSMA.pdf`.

[49] D. M. Pozar. *Microwave Engineering, 4th edition*. John Wiley & Sons, Inc., New York, USA, 2011.

[50] S. B. Cohn. A class of broadband three-port tem-mode hybrids. *IEEE Transactions on Microwave Theory and Techniques*, 16(2):110–116, February 1968.

[51] V. Sokol. *Precise High Frequency Modelling of SMD Components (webminar)*. CST - Computer Simulation Technology AG, Bad Nauheimer Str. 19,64289 Darmstadt, Germany. [Online; accessed 17-April-2018], Available at `https://www.cst.com/solutions/article/precise-high-frequency-modelling-of-smd-components`.

[52] M/A-COM Technology Solutions, Inc. (MACOM), 100 Chelmsford Street, Lowell, MA, USA. *MASW-008322 - GaAs SPDT Switch*, 2015. [Online; accessed 18-April-2018], Available at `https://cdn.macom.com/datasheets/MASW-008322.pdf`.

[53] M/A-COM Technology Solutions, Inc. (MACOM), 100 Chelmsford Street, Lowell, MA, USA. *MADRCC0005 - Single Driver for GaAs FET Switches and Attenuators*, 2015. [Online; accessed 24-April-2018], Available at `http://cdn.macom.com/datasheets/madrcc0005.pdf`.

[54] J.P. Dunsmore. *Handbook of microwave component measurements*. John Wiley & Sons, Inc., New York, USA, 2012.

[55] Renesas Electronics Corporation, Tokyo, Japan. *ICL7660S, ICL7660A - Super Voltage Converters*, 2013. [Online; accessed 5-May-2018], Available at `https://www.intersil.com/content/dam/intersil/documents/icl7/icl7660s-a.pdf`.

[56] G. Bianchi R. Sorrentino. *Microwave and RF Engineering*. John Wiley & Sons, Inc., New York, USA, 2010.

[57] M/A-COM Technology Solutions, Inc. (MACOM), 100 Chelmsford Street, Lowell, MA, USA. *MADRCC0007 - Quad Driver for GaAs FET Switches and Attenuators*, 2015. [Online; accessed 24-April-2018], Available at `http://cdn.macom.com/datasheets/madrcc0007.pdf`.

[58] M/A-COM Technology Solutions, Inc. (MACOM), 100 Chelmsford Street, Lowell, MA, USA. *MAAD-011021 - Digital Attenuator*, 2015. [Online; accessed 25-April-2018], Available at `http://cdn.macom.com/datasheets/maad-011021.pdf`.

[59] Krytar Inc. *ZERO BIAS SCHOTTKY DETECTORS*. Krytar Inc., 1288 Anvilwood Avenue, Sunnyvale, CA 94089 USA, 2010. [Online; accessed 16-April-2018], Available at `https://krytar.com/pdf/200zbs.pdf`.

[60] Cmedia Electronics Inc. *CM6206 High Integrated USB Audio I/O Controller*. Cmedia Electronics Inc., 6F., 100, Sec. 4, Civil Boulevard, Taipei, Taiwan 106 R.O.C., 2013. [Online; accessed 16-April-2018], Available at `https://www.cmedia.com.tw/products/USB20_FULL_SPEED/CM6206`.

[61] J. Huijsing Q. Fan, K. Makinwa. *Capacitively-Coupled Chopper Amplifiers*. Springer International Publishing AG, Cham, Switzerland, 2017.

[62] S. Haykin. *Communication Systems, 4th edition*. John Wiley & Sons, Inc., New York, USA, 2001.

[63] Rohde & Schwarz GmbH & Co. KG. *R&S®HMF2550 - Arbitrary Function Generator*. Rohde & Schwarz GmbH & Co. KG, Mühldorfstr. 15, 81671 München, Germany, 2016. [Online; accessed 3-May-2018], Available at `https://cdn.rohde-schwarz.com/pws/dl_downloads/dl_common_library/dl_manuals/gb_1/h/hmf25xx/HMF25xx_UserManual_de_en_04.pdf`.

[64] K. Them, M. G. Kaul, C. Jung, M. Hofmann, T. Mummert, F. Werner, and T. Knopp. Sensitivity enhancement in magnetic particle imaging by background subtraction. *IEEE Transactions on Medical Imaging*, 35(3):893–900, March 2016.

[65] S. S. Ahmed. Electronic microwave imaging with planar multistatic arrays. Doctoral thesis, Faculty of Engineering, Friedrich-Alexander-Universität, Nürnberg, 2013.

[66] The MathWorks, Inc., Natick, Massachusetts, USA. *Inverse Radon transform - iradon - MATLAB 2018a Documentation*, 2018. [Online; accessed 7-May-2018], Available at `https://www.mathworks.com/help/images/ref/iradon.html`.

[67] Rohde & Schwarz GmbH & Co. KG. *R&S®ZVA / R&S®ZVB / R&S®ZVT Vector Network Analyzers - Operating Manual*. Rohde & Schwarz GmbH & Co. KG, Mühldorfstr. 15, 81671 München, Germany, 2016. [Online; accessed 17-April-2018], Available at `https://cdn.rohde-schwarz.com/pws/dl_downloads/dl_common_library/dl_manuals/gb_1/z/zva_2/ZVA_ZVB_ZVT_OperatingManual_en_30.pdf`.

[68] Rohde & Schwarz GmbH & Co. KG. *Calibration Units - Technical Information*. Rohde & Schwarz GmbH & Co. KG, Mühldorfstr. 15, 81671 München, Germany, 2014. [Online; accessed 17-April-2018], Available at `https://cdn.rohde-schwarz.com/pws/dl_downloads/dl_common_library/dl_manuals/gb_1/z/zvx_1/ZV-Z52_Z55_TechnicalInformation_en_12.pdf`.

Appendices

Appendix A

Measurement of Individual Components

All vector measurements were performed with a ZVA67 4-port VNA [67] calibrated by a ZV-Z52 calibration unit [68]. The reference plane was placed on reference plane of Super SMA 212-502SF connectors [48].

A.1 Measurement of Wilkinson Power Divider

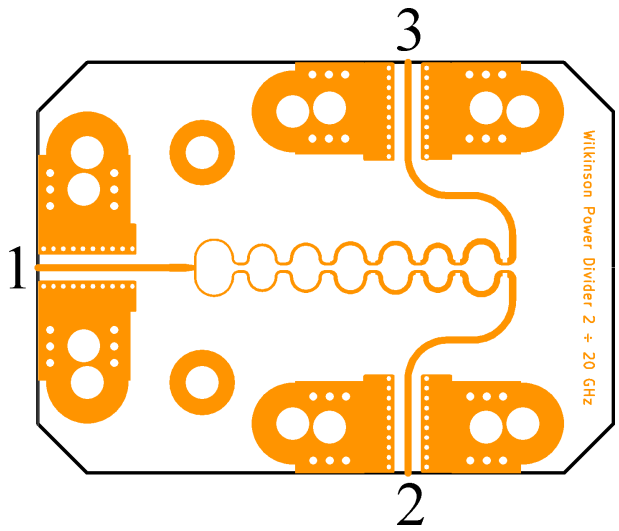

Figure A.1: Layout of the designed Wilkinson divider with numbering of ports. Size of PCB is $35 \times 25\,\mathrm{mm}$.

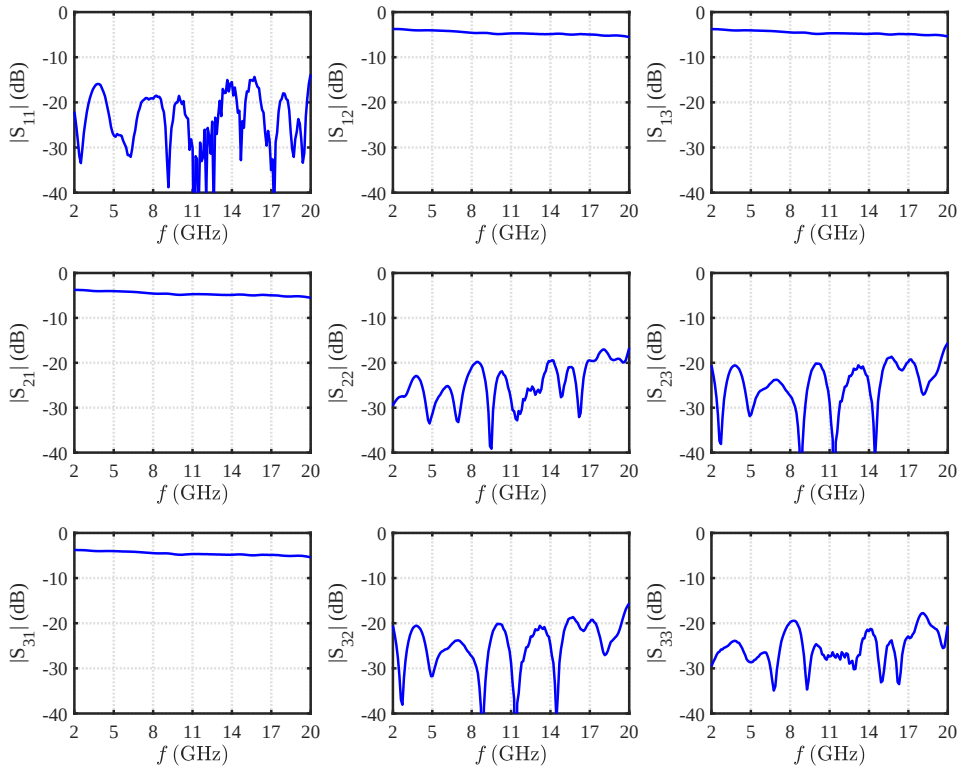

Figure A.2: Measured S-parameters of the Wilkinson power divider. The reference plane of the measurement was on the reference plane of the SMA connectors. Design goals were to have reflections and isolation lower than $-20\,\mathrm{dB}$.

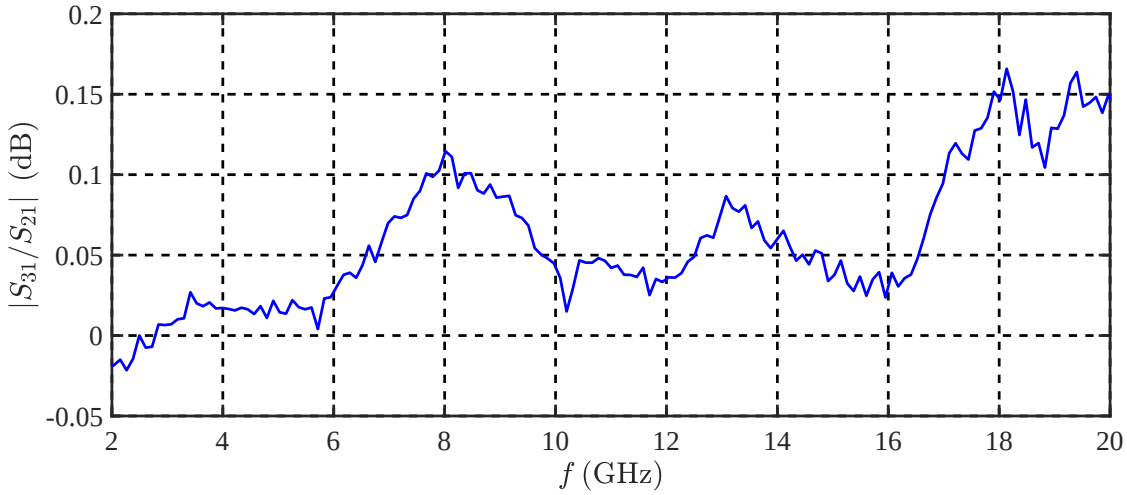

Figure A.3: Measured amplitude unbalance.

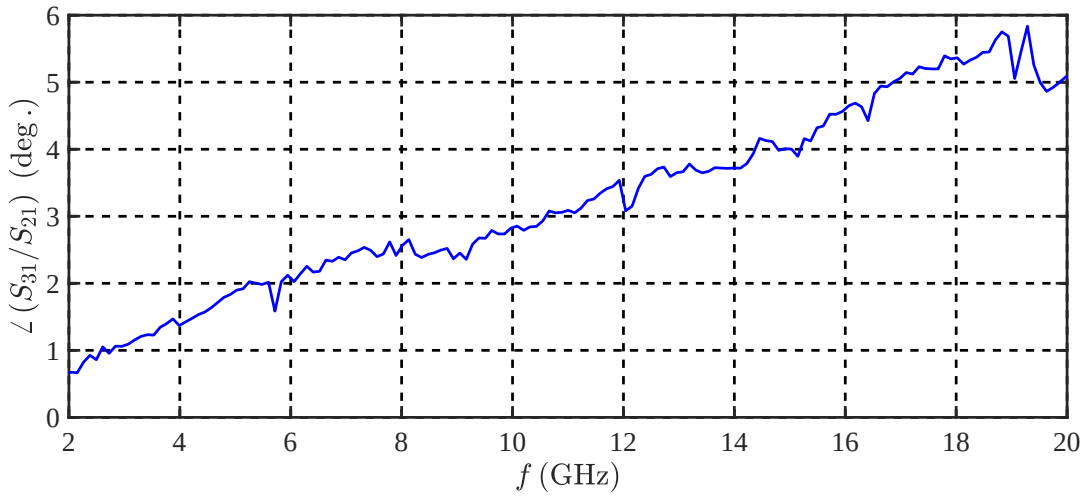

Figure A.4: Measured phase unbalance.

A.2 Measurement of Absorptive Switch

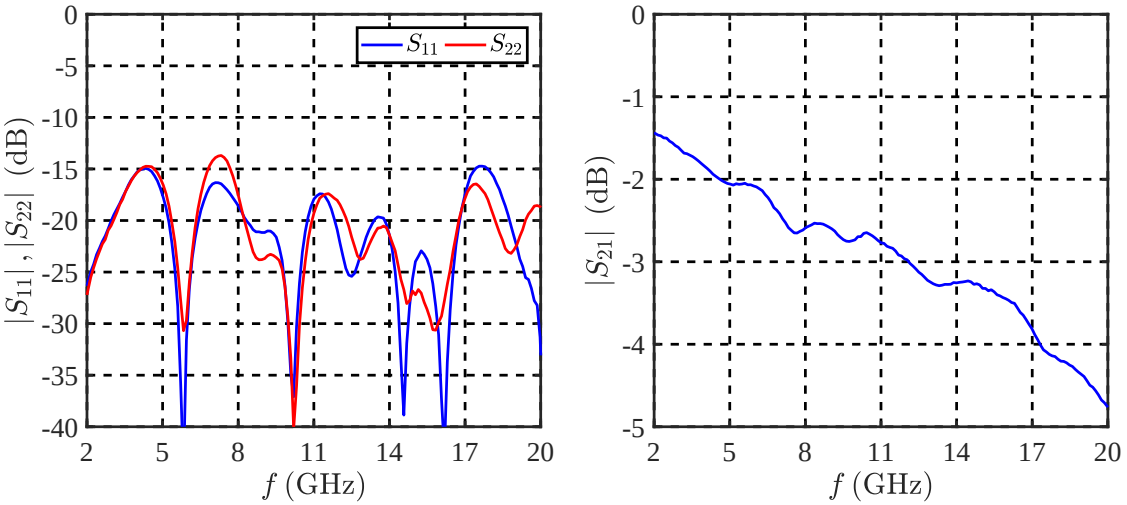

Figure A.5: Measured S-parameters of absorptive switch in ON state.

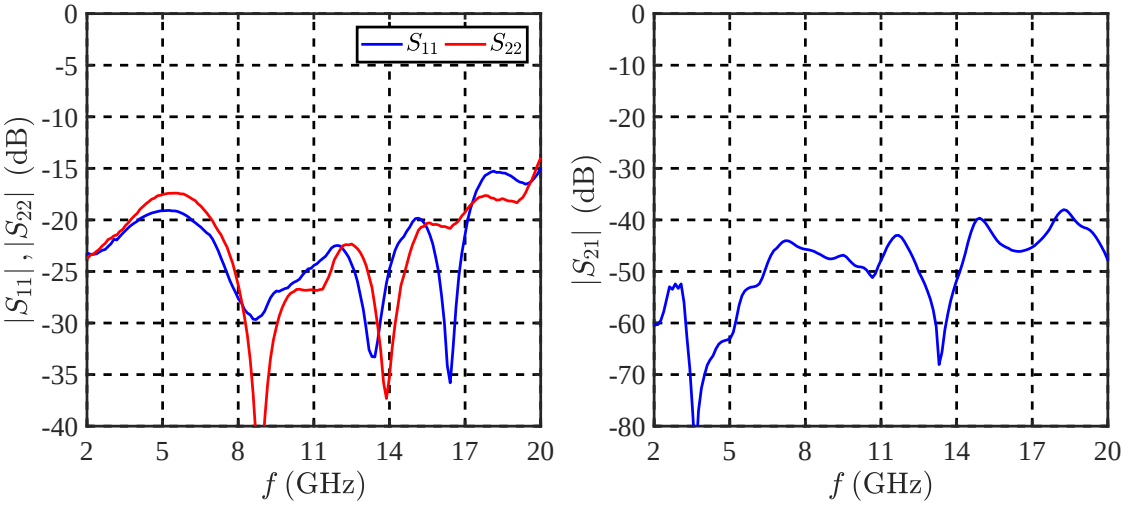

Figure A.6: Measured S-parameters of absorptive switch in OFF state. The magnitude of reflection coefficients is highly affected by load made by parallel combination of two 100 Ω resistors in 0201 SMD package.

A.3 Measurement of Phase Shifter

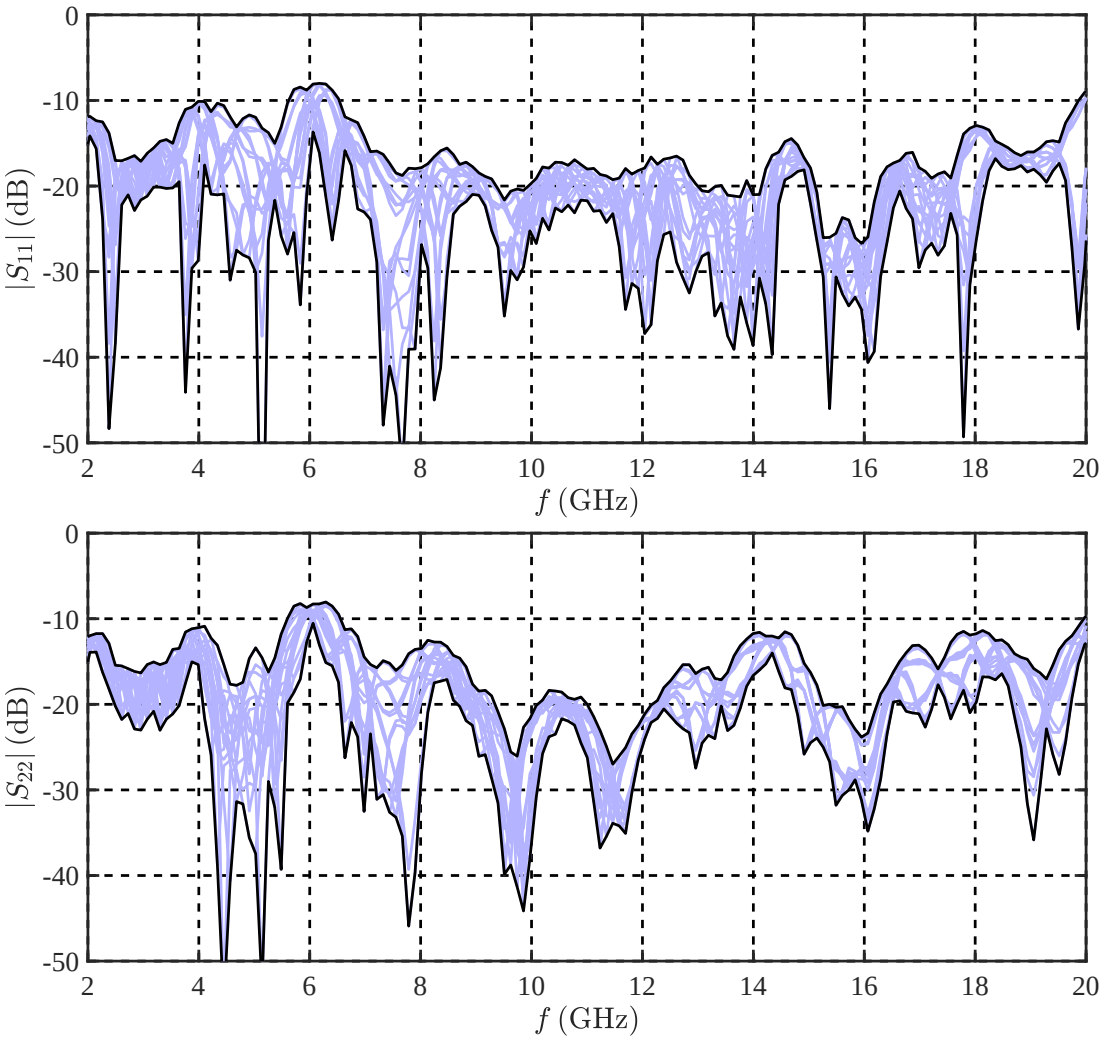

Figure A.7: Range of measured reflection coefficients of digitally controlled 4-bit phase shifter for all 16 states.

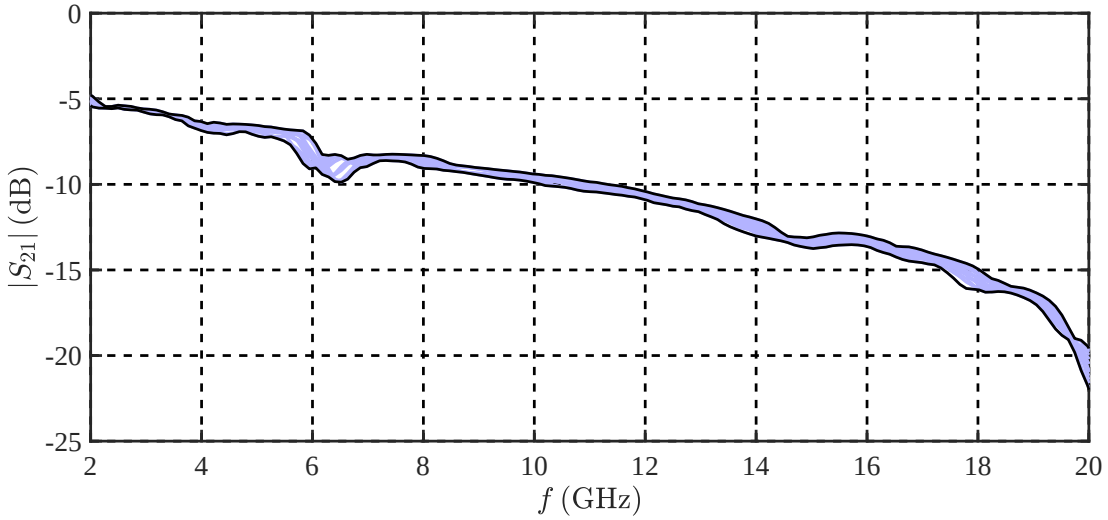

Figure A.8: Range of measured transmission coefficients of digitally controlled 4-bit phase shifter for all 16 states.

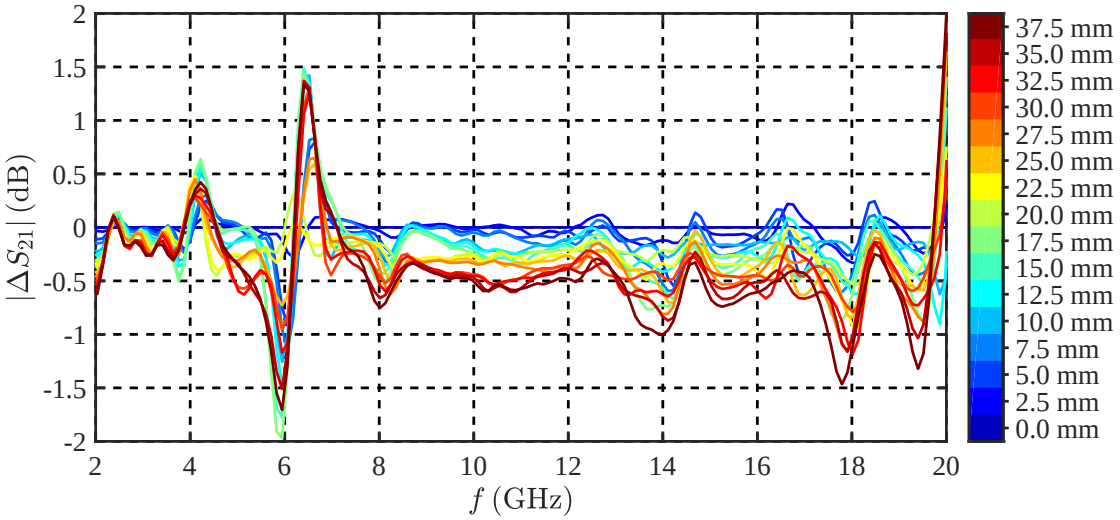

Figure A.9: Relative differences of the transmission coefficients from Figure A.8. The reference transmission is for a relative line of length 0 mm. Generally, the higher the phase shift set, the greater deviation seen.

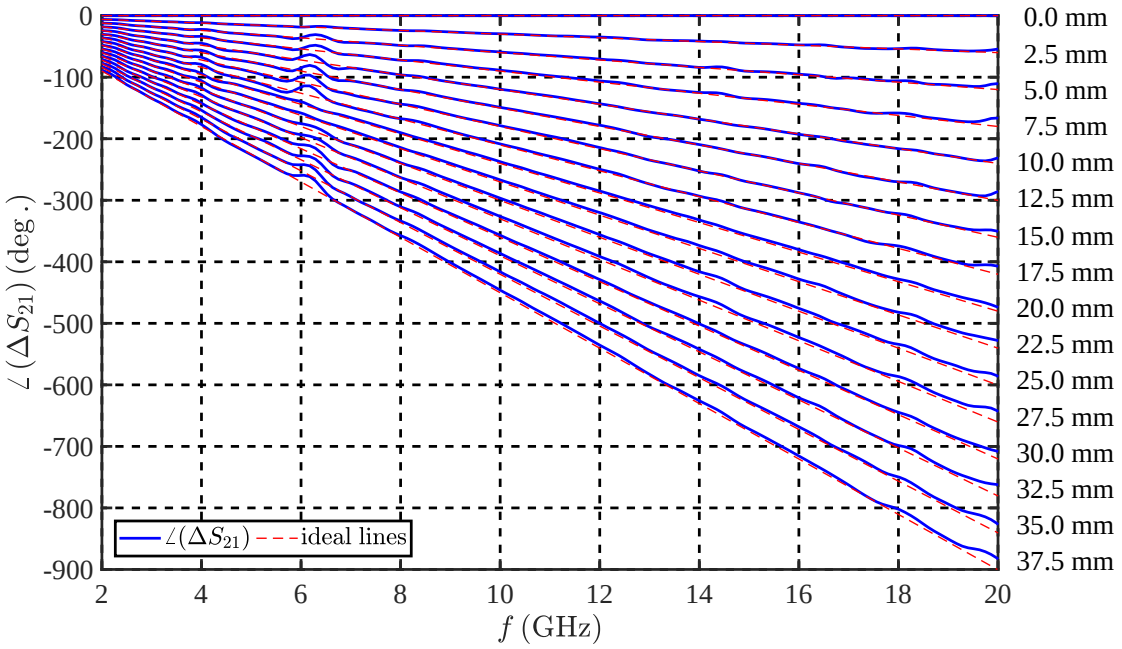

Figure A.10: Relative phase of the measured transmission coefficient and electrical lengths of ideal air lines.

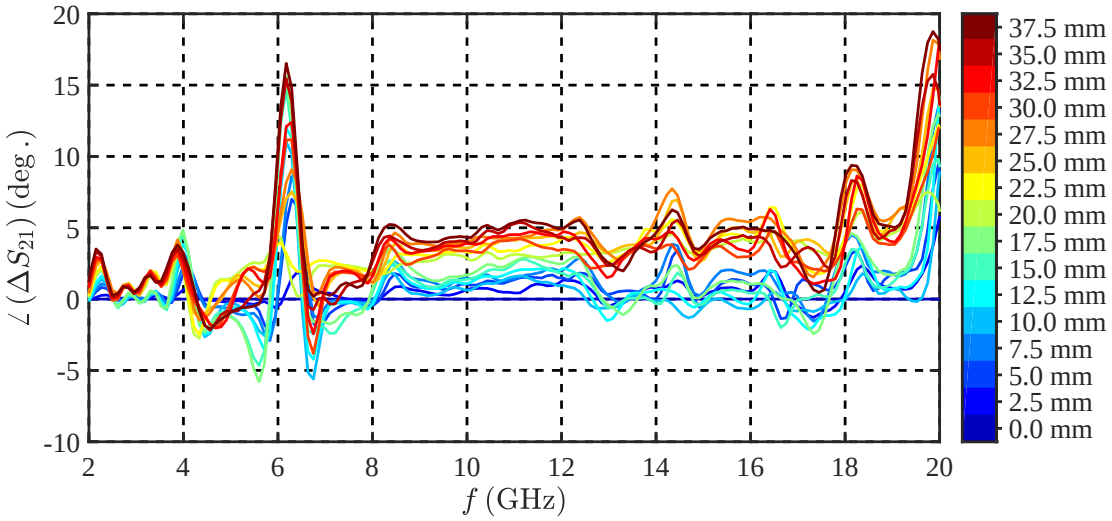

Figure A.11: Deviation of the phase of the transmission coefficient of the phase shifter from electrical lengths of ideal air lines from Figure A.10. In most cases, the larger the phase shift, the larger the deviation.

A.4 Measurement of Attenuator

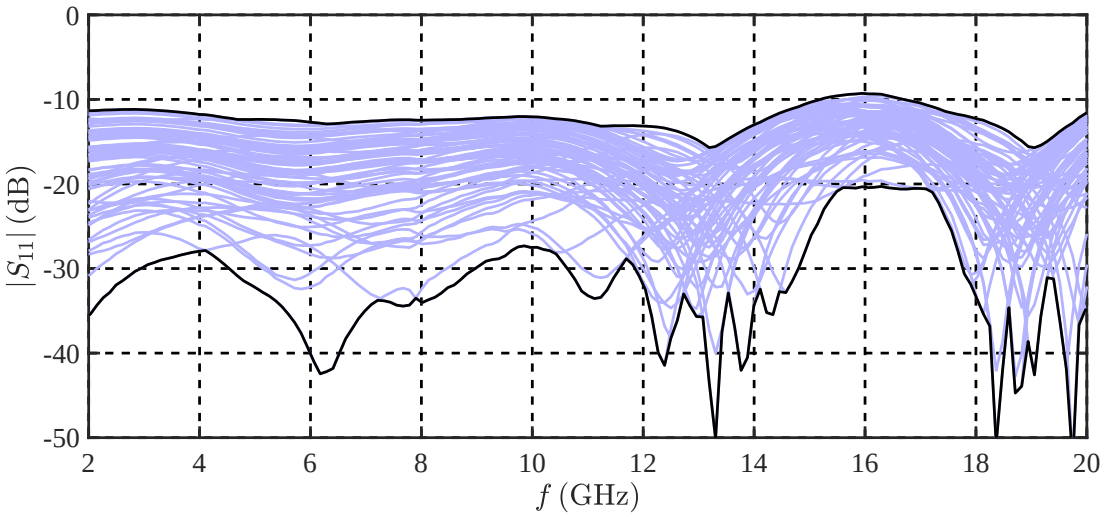

Figure A.12: Range of the measured reflection coefficients for all states of the attenuator.

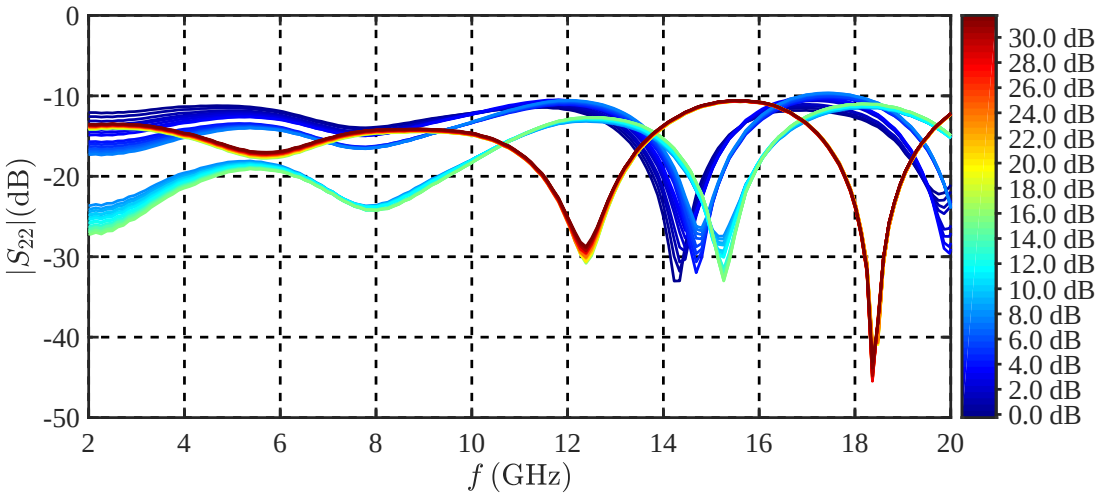

Figure A.13: Reflection coefficients of the attenuator for all states. The dependence of the reflections on the individual connected attenuator stages is obvious.

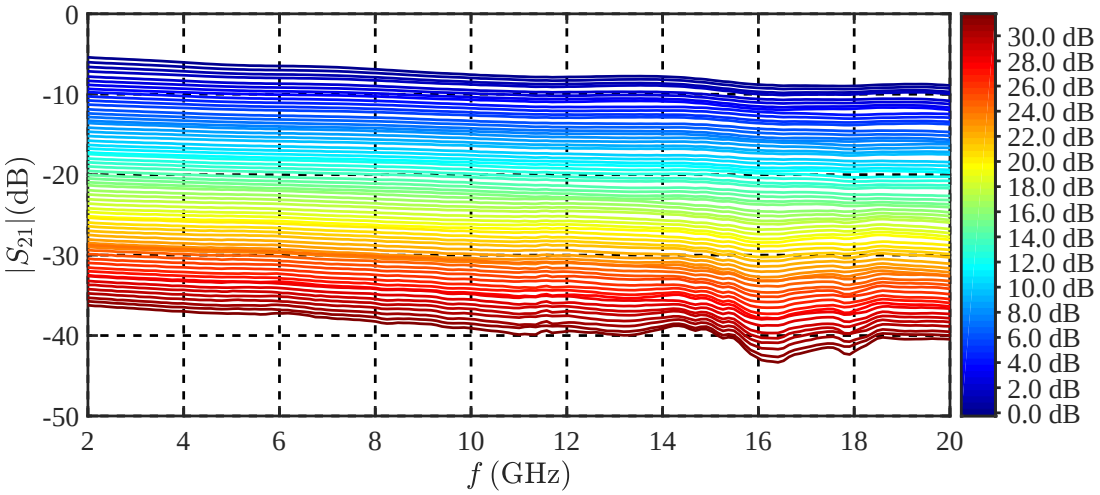

Figure A.14: Measured transmission coefficients of the digitally controlled 6-bit attenuator for all states.

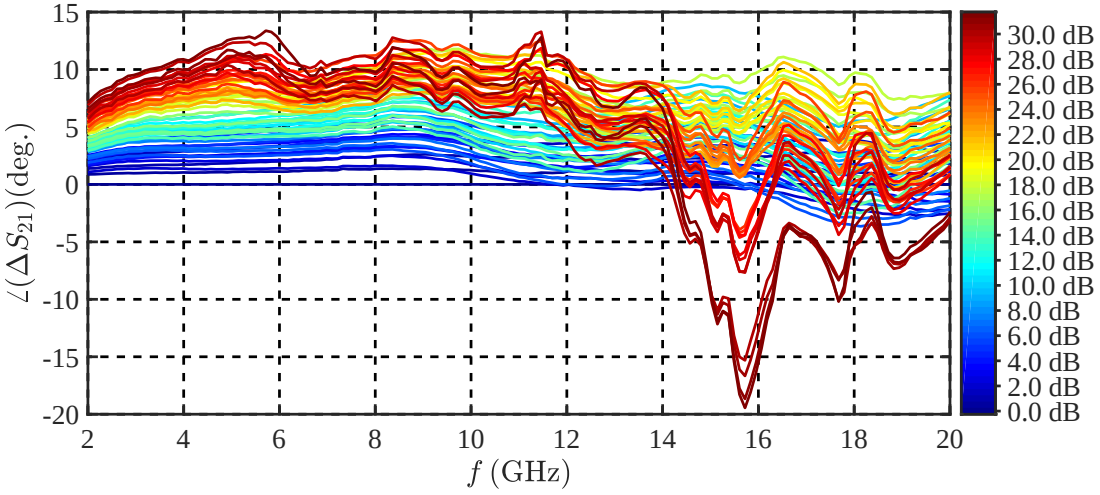

Figure A.15: Phase of attenuator transmission relative to settings with 0 dB attenuation.

Appendix B

List of Candidate's Publications

Stated authors participate equally in listed publications, unless otherwise stated.

B.1 Publications Related to This Thesis

Publications in impacted journals

Adler, V.; Hoffmann, K., Six-Port Spatial Electromagnetic Wave Measurement, IEEE Transactions on Microwave Theory and Techniques, 2014, 62(12), 3161-3171. ISSN 0018-9480.

Cited in:

- Zhang, W.; Hasan, A.; Ghannouchi, F.M.; Helaoui, M.; Wu, Y.; Liu, Y., Concurrent Dual-Band Receiver Based on Novel Six-Port Correlator for Wireless Applications, Access IEEE, vol. 5, pp. 25826 - 25834, 2017, ISSN 2169-3536.
- Staszek, K; Gruszczynski, S; Wincza, K, Six-Port Reflectometer Providing Enhanced Power Distribution, IEEE Transactions on Microwave Theory and Techniques, vol. 64, no. 3, pp. 939 - 951, 2016, ISSN 0018-9480.

Peer-reviewed publications

Adler, V.; Hoffmann, K., Spatial Vector Measurement Based on Six-Port Concept, 81st ARFTG Microwave Measurement Conference Proceedings, New Jersey: IEEE, 2013. pp. 114-116. ISBN 978-1-4673-4982-6.

B.2 Other Publications

Peer-reviewed publications

Adler, V.; Moll, J.; Kuhnt, M.; Hils, B.; Krozer, V.; Hoffmann, K., High Resolution Range Imaging Via Model-based Compressed Sensing, Proceedings of PIERS 2015 in Prague. Cambridge, Electromagnetics Academy, 2015. pp. 248-252, ISSN 1559-9450, ISBN 978-1-934142-30-1.

Cited in:

- Moll, J.; Krozer, V., Radar-based mechanical vibration sensing for structural health monitoring applications: A comparison of radar transceiver measurements at 24 GHz and 100 GHz, Proceedings of 8th European Workshop on Structural Health Monitoring, EWSHM 2016, Bilbao, Spain, Volume 3, Pages 2128-2133, e-ISBN: 978-151082793-6.

Ourednik, P.; Hudec, P.; **Adler, V.**, TRL-based measurement of active antennas and other more complex microwave structures, Proceedings of 89th ARFTG Microwave Measurement Conference, Piscataway (New Jersey): IEEE, 2017, pp. 83-86, ISBN 978-1-5386-2747-1.

Capek, M.; Hazdra, P.; **Adler, V.**; Kadlec, P.; Sedenka, V.; Marek, M.; Masek, M.; Losenicky, V.; Strambach, M.; Mazanek, M.; Rymus, J., AToM: A Versatile MATLAB Tool for Antenna Synthesis, Proceedings of 12th European Conference on Antenna and Propagation (EuCAP), London, UK, April 2018, to be published.

Functional Samples

Hazdra, P.; Capek, M.; **Adler, V.** (25%), Planar circularly polarized antenna, 2017.

List of Figures

List of Tables